Spring 2018

Distributed Sensing and System Identification of Cantilever Beams and Plates in the Presence of Weak Nonlinearities

Patrick Sean Heaney
Old Dominion University, patrick.s.heaney@gmail.com

DISTRIBUTED SENSING AND SYSTEM IDENTIFICATION OF CANTILEVER BEAMS AND PLATES IN THE PRESENCE OF WEAK NONLINEARITIES

by

Patrick Sean Heaney
B.A. May 2009, Yale University
M.S. May 2014, University of Pennsylvania

A Thesis Submitted to the Faculty of
Old Dominion University in Partial Fulfillment of the
Requirements for the Degree of

MASTER OF SCIENCE

MECHANICAL ENGINEERING

OLD DOMINION UNIVERSITY
May 2018

Approved by:

Sebastian Bawab (Director)

Onur Bilgen (Member)

Thomas Alberts (Member)

ABSTRACT

DISTRIBUTED SENSING AND SYSTEM IDENTIFICATION OF CANTILEVER BEAMS AND PLATES IN THE PRESENCE OF WEAK NONLINEARITIES

Patrick Sean Heaney
Old Dominion University, 2018
Director: Dr. Sebastian Bawab

While the mathematical foundation for modal analysis of continuous systems has long been established, flexible structures have become increasingly widespread and developing tools for understanding their mechanics has become increasingly important. Cantilever beams and plates, in particular, have been extensively studied due to their practical importance as approximations of more complex structures. The focus of this thesis is on understanding the dynamics of vibrating cantilever beams and plates through analytical and experimental investigation. Various models for the mechanics of these structures, of varying physical fidelity, are described and compared. A fiber optic sensing system is utilized to experimentally acquire distributed strain measurements, which are used to estimate the mode shapes and natural frequencies for the cantilever structures. These experimental estimates are compared with analytical and numerical solutions corresponding to the models previously introduced. Next, a detailed case study is described which demonstrates the nonlinear response in a cantilever beam's first mode and implements an empirical procedure for estimating a variable parameter model which accounts for its varying system parameters. By implementing the described identification methods, parameter variations due to a system's nonlinear response are included in a modified linear model and significantly reduce the errors in predicted response. Based on this research, methods to experimentally estimate and validate the mode shapes and system parameters can be implemented for other beam- and plate-like structures.

To Kristen, Sammy, and Lucas – your love and support have made this work possible.

ACKNOWLEDGMENTS

First, I would like to thank Dr. Onur Bilgen for his constant support and guidance throughout my graduate study. Over the course of innumerable hours in the office and laboratory, he has been instrumental in my development as a student and researcher.

I would like to thank my wife, Kristen, who has been essential to the completion of this work. Even with two small boys at home and teaching high school mathematics (where she is responsible for even more children), she has been a constant source of support during my graduate study and continues to be an inspiration for all that I do.

Thanks to the Department of Mechanical and Aerospace Engineering at Old Dominion University, especially Dr. Sebastian Bawab. The system identification tests presented in Chapter 4 were conducted in the Smart Systems Laboratory at Old Dominion University, and the financial support of the Department was critical in developing those results. Finally, I would like to thank the National Aeronautics and Space Administration (NASA), which has provided funding and laboratory space at Langley Research Center to support the fiber optic sensing tests described in Chapter 3. The material in that chapter is based upon work supported under Grant Number NNX16AT14H issued through the NASA Education Aeronautics Scholarship and Advanced STEM Training and Research (AS&ASTAR) Fellowship.

NOMENCLATURE

FBG	Fiber Bragg Grating
FE	Finite Element
FFT	Fast Fourier Transform
FOSS	Fiber Optic Strain Sensing
FRF	Frequency Response Function
MDOF	Multiple Degrees of Freedom
OFDR	Optical Frequency Domain Reflectometry
SDOF	Single Degree of Freedom
WDM	Wavelength Division Multiplexing
A	Cross-sectional area
b	Width
c	Damping constant
D	Flexural rigidity of a plate
E	Elastic modulus
F	Point force
f	Distributed force
F_r	Modal force
G	Shear modulus
g	Electromechanical coupling factor
H	Frequency response function
h	Thickness
I_i	Second moment of area of the cross section with respect to the $i \in \{y,\ z\}$ axis
I_x	Second polar moment of area about the x-axis
J	Torsional constant
j	Imaginary unit

k	Stiffness
L	Lagrangian function
l	Length
M	Moment
m	Mass
p_e	Photoelastic constant
Q	Generalized force
R	Radius of curvature
r	Frequency ratio
T	Kinetic energy
$\mathcal{T}$	Torque
t	Time
U	Strain energy
V	Potential energy of applied load
$\mathcal{V}$	Shear force
u, v, w	Deformations in x-, y-, and z-directions
x, y, z	Dimensional coordinates
$\hat{x}, \hat{y}, \hat{z}$	Non-dimensional coordinates
α	Twist rate
β	Weighted frequency for free-free beam
γ	Coupling correction
δ	Variation operator
δ_{ij}	Kronecker delta
ε_{ij}	Strain tensor
ζ	Damping ratio
η	Modal coordinate
θ	Angular twist

κ	Curvature
$\varkappa$	Torsion warping function
λ	Frequency parameters
λ_B	Bragg wavelength
ν	Poisson's ratio
ν_i	Direction cosine of the outward pointing normal in the i-direction
ξ	Weighted frequency for clamped-free beam
ρ	Mass per volume or per unit length
τ_{ij}	Stress tensor
ϕ	Mode shape for clamped-free beam
φ	Prandtl stress function
χ	Mode shape for free-free beam
ψ	Angle of rotation
Ω	Domain of the beam or plate
ω	Angular frequency
$\mathcal{L}$	Linear operator
∇^4	Biharmonic operator
∂_i	Partial differentiation with respect to i

TABLE OF CONTENTS

Page

Page

LIST OF TABLES

LIST OF FIGURES

Figure Page

Figure Page

Figure Page

CHAPTER 1
INTRODUCTION AND BACKGROUND

1.1 Introduction

Continuous systems, such as beams and plates, have been extensively analyzed due to their practical importance as models for more complex real-world structures. Two such examples include an aircraft's wing or a single wing panel. Understanding beam and plate mechanics yields important insight into the behavior of these more complex real-world structures. Due to the relative ease of manufacture, for example, wind tunnel models of complex wings are often created using an equivalent beam that represents the same bending and torsional stiffness of the wing to be studied. The outer mold line of the wing is then attached to the beam to provide the proper aerodynamic shape, while the structural behavior is governed by the internal beam or plate structure.

Based on the importance of understanding these structures, numerous models have been developed which approximate their physics to various degrees of accuracy. Higher fidelity models are more challenging to analyze and often do not yield results which are immediately useful for design or interpretation. Thus, lower fidelity models are often useful as approximations to the actual physics and yield results which provide insight into the structural behavior. An understanding of how closely the approximate models represent the actual system is important – if the simple approximation is relatively accurate, it is often preferred to the more complex model. The analysis, identification, and evaluation of several approximate models forms the foundation of this thesis. Two particular issues are investigated: (1) Experimental estimation and validation of mode shapes and (2) Experimental system identification of parameters for the assumed models. The tools of modal analysis are applied to these problems in order to compare experimental results with various analytical and numerical models.

The next section provides a background and literature review of work related to the topics investigated in this thesis. The motivation, objectives, and outline of the thesis are then presented.

1.2 Background and Literature Review

1.2.1 Fiber Optic Strain Sensors

One method for experimentally estimating the deformation of a structure employs distributed fiber optic strain sensors (FOSS). In this method, which is described in Chapter 3, the strains can be measured at hundreds of points and orientations in a structure and then used to estimate its deformation. Depending on the type of sensing system employed, in general these measurements either have high spatial resolution (many sensors per unit length) or high time resolution (many measurements per unit time). In this thesis, the second type is utilized since the goal is to estimate the dynamic behavior of the structure at relatively high frequencies.

The use of FOSS for shape sensing applications has been investigated for years, and several methods have been employed to transform distributed strain measurements into estimated deflection shapes. The most common method relies on using distributed strain measurements to estimate curvatures, and then integrating the curvatures twice to yield the structural deflections. This is the method utilized in this thesis and is described in detail in Chapter 3. Ko [1] described the implementation of this method and presented results, based on simulated strain measurements from finite element (FE) analysis, which validated the accuracy of the shape reconstruction for beams and for plates with multiple span-wise fibers.

Simulation and experimental results for an approximate method, known as modal superposition, were presented by Li et al. [2] in an analysis of the static and dynamic shapes of a plate. In this method, a finite number of structural modes are used to reconstruct the deflection based on relatively few strain measurements, but prior knowledge of the struc-

ture's mode shapes is required. The results presented in that paper indicate relatively good agreement for the single reference point used.

Another method is known as the inverse FE method. In this method, an FE model is used to extend the estimated deflection shape along the fiber to points not instrumented with FOSS in order to construct the three-dimensional deformation field. Vazquez et al. [3] applied this method for shape reconstruction based on experimental strain measurements and reported accurate results for the estimated cantilever beam deflection. Simulation results were reported by Gherlone et al. [4] for a method implementing this inverse FE method for several different structures. Their results were relatively robust even in the presence of simulated noise. Extending the previous shape reconstruction algorithm detailed by Ko [1], Pak [5] described a two-step method which included an FE model to interpolate the deformation for the entire structure based on strain measurements from parallel, span-wise, fibers. For various load cases, his method was quite accurate in reconstructing the deformation field in comparison to photogrammetry data.

A number of additional experimental studies have been conducted validating the use of FOSS for shape reconstruction. Using an array of FOSS sensors, Jones et al. [6] fit a surface to the measured strain prior to calculating the static deflection of a plate. In comparison to displacement measurements from a linear variable differential transformer, this method was shown to be relatively accurate despite the low number of strain measurements. Glaser et al. [7] incorporated an interpolating spline to the beam shape reconstruction algorithm in order to increase the number of strain measurements and showed that errors between the algorithm and photogrammetry data for various load cases were small. In another comparison with photogrammetry results, Bakalyar and Jutte [8] used FOSS to estimate the static deflection shape of several thin plate-like structures. The results indicated that processing FOSS data for deflection data is less accurate, but comparable, with photogrammetry data. Using the swept plate specimen from Bakalyar and Jutte [8], Derkevorkian et al. [9] used a Displacement Transfer Function (DTF) method to estimate the deflection shape of a

swept plate using FOSS sensors. Comparing their data with photogrammetry results showed excellent agreement.

Several studies have also considered the use of FOSS for large-scale structures. One early study by Childers et al. [10] used 3,000 FOSS sensors applied to a semi-span wing and showed good agreement with foil strain gages also instrumenting the structure. Jutte et al. [11] also used FOSS to instrument a full-scale wing and found that in comparison to photogrammetry, the calculated deformation based on the shape sensing method was accurate for wing bending but sensitive to error for estimating wing twist. The results reported by Nicolas et al. [12] for a semi-span full scale composite wing confirm that algorithms for shape reconstruction based on measured strain are effective for wing bending in comparison to reference measurements.

Although the focus of the research described above has been on static shape sensing, other researchers have studied the use of FOSS for dynamic measurements. Cusano et al. [13] used the frequency response functions calculated based on excitation impacts at different locations along the span of a cantilever beam to estimate the mode shapes of the beam. The frequency response functions developed using a tip accelerometer and those using a mid-span FOSS sensor were calculated and resulted in comparable estimated mode shapes. Jiang et al. [14] described a method to calculate the real-time mode shapes of a cantilever beam using FOSS. Results reported in this study indicated close agreement with analytical predictions and were demonstrated to be effective in updating the mode shape estimate after a step-change in mass.

Various studies have also been conducted using FOSS as sensors for active control. Using a single FOSS sensor as feedback, Chau et al. [15] implemented and demonstrated the effectiveness of various control laws. Two control architectures for vibration supression of a composite cantilever beam were investigated by Braghin et al. [16], demonstrating that improved suppression performance can be achieved by integrating control laws utilizing the distributed strain measurements from multiple FOSS sensors. Cazzulani et al. [17] described

a sensor-averaging technique to reduce feedback signal noise from FOSS sensors and implemented the method in a "quasi-modal" controller. Results from this study showed the same vibration suppression improvements through the use of many FOSS sensors. In an extension of these results, Cazzulani et al. [18] found similar vibration suppression performance when employing a modal control method.

1.2.2 System Identification

The complex task of mathematically modeling the structural dynamics of continuous systems such as beams has led to numerous models that, under certain conditions and assumptions, closely approximate physical observations. In the Euler-Bernoulli beam model, for example, the beam's governing equation for transverse motion is a partial differential equation second order in time and fourth order in the spatial dimension. The solutions for this governing equation under various boundary conditions are well known, and yield infinite natural frequencies and mode shapes of the beam. Since the identification of such a model requires an infinite number of measurements, in practice the distributed model is truncated to yield a tractable discrete parameter model, while still including enough terms to yield sufficient accuracy within a frequency range of interest. Analysis of this truncated, reduced order, model can then proceed through system identification of a single degree of freedom (SDOF) lumped parameter model for each included mode.

In SDOF analysis, individual modes of the truncated system are considered one at a time and the dynamics in the frequency region around that mode are approximated by a lumped parameter model, with well-defined parameters such as mass, damping, and stiffness [19]. For many applications, to include control system design and system identification for an FE model, the lumped parameter approach can be used to accurately model the system behavior in a finite frequency domain. When the natural frequencies of the modes of interest are relatively far apart, so that the modal interactions are negligible, and the frequency domain of interest is limited, the lumped parameter approach is effective and yields

a simple analytical model that captures the dynamic behavior of the system.

An issue arises in experimentally estimating the parameters of the SDOF model when nonlinearities exist in the system's physical response to an excitation. In the presence of nonlinearities, the identified parameters of the SDOF model (i.e. mass, damping, and stiffness) may be dependent on the amplitude of excitation. As flexible structures have become more widespread and the need for higher fidelity structural models has increased, understanding these nonlinearities and developing appropriate analysis and system identification methods have received significant attention [20, 21, 22].

While nonlinear behavior is characteristic of many systems for responses of relatively high amplitude, an additional electromechanical nonlinearity may be introduced for devices excited by a piezoelectric actuator. This method, through which the system is actuated by distributed strain-induced excitation, is frequently used in the field of smart materials. Classical models of beams in bending have been extended by various researchers to incorporate electromechanical coupling in a piezocomposite structure, although most analyses assume linear constitutive equations for preliminary design and optimization.

Modeling of and experimentation with piezocomposite actuators, operating under the converse piezoelectric effect, has been a focus of research since the 1980s. Crawley and DeLuis [23] investigated the electromechanical coupling in piezocomposite structures and applied their model to the static and dynamic responses of a piezocomposite beam. This work was extended by Im and Atluri [24], who included axial and transverse shear forces in the mechanically coupled bending model. Using a state space model of the coupled electromechanical dynamics of a piezocomposite structure, Hagood et al. [25] compared their model to empirical data for a piezocomposite cantilever beam. Crawley and Anderson [26], in developing several strain-induced actuation models, identified empirical departures from the linear piezoceramic constitutive equations. With the objective of increasing structural damping, Hagood and von Flotow [27] modeled and experimentally validated a passive piezoelectric circuit on a piezocomposite beam. Kim and Jones [28] investigated optimal choices

for piezoelectric actuator thicknesses in a piezocomposite beam structure for both static and dynamic excitation.

SDOF systems are frequently used to model piezocomposite structures for static and dynamic analyses. Park and Chopra [29] developed an SDOF coupled model of extension, bending, and torsion of a piezocomposite beam. Brennan and McGowan [30] developed and experimentally tested an SDOF model of the power consumption of a piezoelectric actuator. An SDOF model of a piezocomposite beam for energy harvesting was considered by Erturk and Inman [31] and its predictions were compared with a corresponding distributed parameter model. The result of this comparison was a correction factor for the SDOF transverse vibration model to improve its accuracy in comparison to the distributed parameter model.

Although these SDOF models are often used for preliminary analysis and design, higher fidelity distributed parameter models of piezocomposite structures have also received attention. Erturk and Inman [32] derived a coupled distributed parameter model for an energy harvesting piezocomposite beam. A distributed parameter model for actuation of a piezocomposite beam was presented by Bilgen et al. [33], who compared its analytical predictions with experimental dynamic responses. The reported experimental data demonstrated nonlinear mechanical responses during piezoelectric actuation. In a comparison of the performance of several piezoelectric actuators, Bilgen et al. [34] experimentally demonstrated constitutive nonlinearities in the frequency response of the piezocomposite beams.

1.3 Objectives

The goal of this thesis is to apply the techniques of modal analysis to the experimental system identification of cantilever beam and plate structures. Specific objectives are:

1. To analyze and compare several models describing the mechanics of cantilever beams and plates.

2. To estimate the mode shapes for a cantilever beam and plate through distributed strain

measurements acquired with fiber optic strain sensors.

3. To develop a model and experimental procedures for accurately estimating the system parameters of a weakly nonlinear system, which can be used to represent the dynamics of a single mode of a cantilever beam or plate.

1.4 Outline

The remaining chapters in this thesis address the following topics. The focus of Chapter 2 is on the mechanics of cantilever beam and plate structures. Analytical solutions to the equations of motion and various approximations are introduced, analyzed, and compared.

These results are then applied to the problem of shape sensing in Chapter 3. After a brief description of the operation of FOSS systems, the mechanical results previously derived are utilized in the development of a shape sensing algorithm. Simulated and experimental results are discussed in depth for the cantilever beam, and comparisons are given for the several analytical model estimates described in Chapter 2. Two methods for estimating the twist in a cantilever plate are described in detail, and then FE and experimental results are compared.

Chapter 4 describes a procedure for estimating the variability of parameters of a weakly nonlinear system, and an in-depth case study is presented applying the method to identification of the first bending mode of a cantilever beam. A modified second-order model with variable parameters is proposed and experimental tests conducted to empirically estimate the models describing those parameters. Comparisons are made between the identified variable parameter models and a reference constant parameter model.

A summary of the results from this thesis is given in Chapter 5. A list of publications related to this work is also provided and topics for future research discussed.

CHAPTER 2
VIBRATION OF CANTILEVER BEAMS AND PLATES

2.1 Introduction

In this chapter, the mechanics of cantilever beams and plates are considered. Beams and plates are naturally modeled as distributed parameter systems, where the number of degrees of freedom are infinite. Using equilibrium and energy considerations, these distributed parameter equations of motion are derived for each system and solution techniques for the resulting partial differential equations reviewed. Of particular interest are the bending and twisting of a cantilever beam and approximate solution techniques for the general vibration modes of a cantilever plate. Each system is also analyzed using an associated discrete parameter system, which is a system that can be modeled with a countable number of degrees of freedom. These include single degree of freedom (SDOF) as well as multiple degrees of freedom (MDOF) systems.

The results outlined in this chapter form the analytical/numerical foundation for the experimental procedures and results which are described later. Various results related to SDOF and MDOF vibration, which are reviewed in Appendices A and B, will be used in the analysis of this chapter.

2.2 Transverse Vibration of a Cantilever Beam

After deriving the equation of motion for the transverse vibration of a cantilever beam, static and dynamic solutions will be shown in this section. The deflection and curvature shapes associated with these responses will be used extensively in Chapter 3 in comparison to their experimentally determined counterparts resulting from the use of distributed sensors. SDOF and MDOF models are then discussed and their natural frequency predictions compared with those of the distributed parameter model.

2.2.1 Distributed Parameter Model

Consider the cantilever beam shown in Fig. 2.1. The model to be analyzed is prismatic with dimensions b, h, and l for its width, thickness, and length. The transverse vibration of this system refers to the motion of the beam's centerline in a single bending direction, here denoted as w.

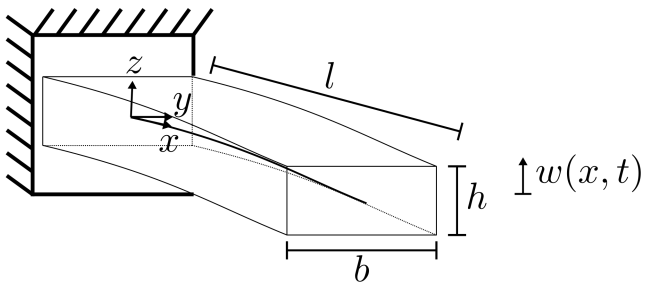

Figure 2.1: Schematic of a cantilever beam in bending.

In this analysis of transverse vibration, the beam's motion is assumed to be a function only of the x-coordinate and time, so the three-dimensional model can be reduced to the two-dimensional schematic shown in Fig. 2.2.

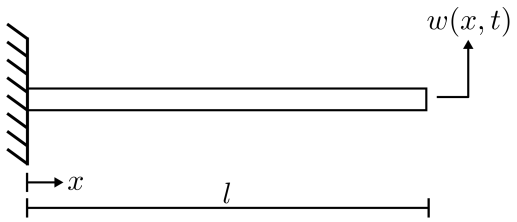

Figure 2.2: Two-dimensional schematic of a cantilever beam in bending.

Additional assumptions include: (1) the beam's width and thickness are much smaller than its length, (2) the beam's deflection is small, (3) the beam's centerline does not stretch, (4) cross sections of the beam are rigid and remain normal to the beam's centerline, and (5) rotational inertia and transverse shear are negligible. The analysis and results associated with these assumptions are collectively known as Euler-Bernoulli, or Classical, beam theory.

Newton/Euler Method

In order to develop the equations of motion for this system, several results related to the geometric and constitutive relationships are first established. Consider the curve shown in Fig. 2.3, where s is the curvilinear length along the curve and dx and dw correspond to the differentials shown.

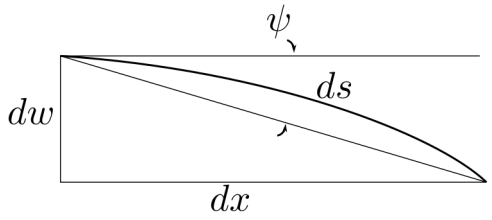

Figure 2.3: Bending curvature for a beam segment.

This curve represents a segment of the beam centerline in bending. The curvature κ and radius of curvature R are defined as:

$$\kappa = \frac{1}{R} \equiv \frac{d\psi}{ds} = \frac{d\psi}{dx} \cdot \frac{dx}{ds} \,. \tag{2.1}$$

Taking $'$ to indicate differentiation with respect to x, from Fig. 2.3 the slope of the

diagonal line can be written $w' = \tan\psi$. Differentiating this expression:

$$\begin{aligned} w'' &= \sec^2\psi \cdot \frac{d\psi}{dx} \\ &= \left(1 + \tan^2\psi\right) \cdot \frac{d\psi}{dx} \\ &= \left(1 + (w')^2\right) \cdot \frac{d\psi}{dx}\,, \end{aligned} \tag{2.2}$$

and then rearranging results in the following relationship:

$$\frac{d\psi}{dx} = \frac{w''}{1 + (w')^2}\,. \tag{2.3}$$

In addition, as $dx \to 0$ the curve in Fig. 2.3 is approximated by the diagonal connecting its endpoints. Based on the triangle which is formed, $ds^2 = dx^2 + dw^2$. Dividing this Pythagorean expression by dx^2, this relationship can be rearranged as:

$$\begin{aligned} \frac{ds}{dx} &= \sqrt{1 + (w')^2} \\ \Rightarrow \frac{dx}{ds} &= \frac{1}{\sqrt{1 + (w')^2}}\,. \end{aligned} \tag{2.4}$$

Substituting the results of Eqn. 2.3 and Eqn. 2.4 into Eqn. 2.1 yields an expression for the curvature:

$$\kappa = \frac{w''}{1 + (w')^2} \cdot \frac{1}{\sqrt{1 + (w')^2}} = \frac{w''}{\left(1 + (w')^2\right)^{3/2}}\,. \tag{2.5}$$

From this result, if the slope of the curve is small, i.e. $w' \approx 0$, then κ can be approximated as:

$$\kappa = w''(x)\,. \tag{2.6}$$

Now consider a representative beam segment under bending, shown in Fig. 2.4.

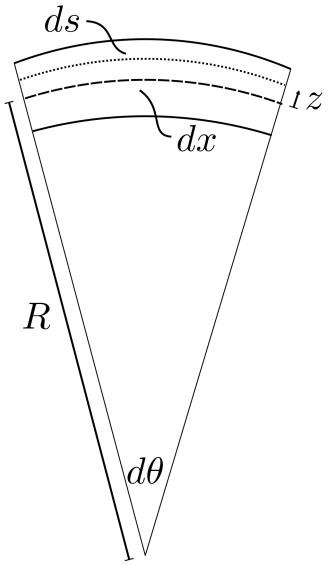

Figure 2.4: Bending strain for a beam segment.

The strain ε_{xx} in a layer at distance z from the neutral axis, denoted with a dotted line in the figure, is given by:

$$\varepsilon_{xx} = \frac{ds - dx}{dx} = \frac{(-R + z)\, d\theta + R d\theta}{-R d\theta} = -\frac{z}{R} = -z\kappa = -z w''(x)\,, \tag{2.7}$$

where the result of Eqn. 2.6 has been substituted and $R < 0$ if directed below the beam in order to yield the correct sign for the corresponding moment.

Assuming a linear elastic material, the normal stress τ_{xx} in the segment can be expressed using Hooke's Law as:

$$\tau_{xx} = E\varepsilon_{xx} = -Ezw''(x)\,, \tag{2.8}$$

where E is the elastic modulus.

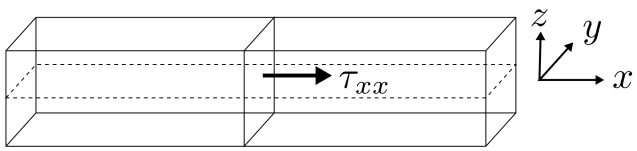

Figure 2.5: Normal stress for a beam segment.

Given a plane intersecting the beam at position x, as shown in Fig. 2.5, the moment M at that section can be determined by integrating the stress contribution of each layer multiplied by its distance from the neutral axis:

$$\begin{aligned} M(x) &= -\iint_A \tau_{xx} \cdot z \; dA \\ &= Ew''(x) \iint_A z^2 \; dA \\ &= EI_y w''(x) \,, \end{aligned} \tag{2.9}$$

where I_y is the second moment of area of the cross section with respect to the y-axis and A is the cross-sectional area. For a rectangular cross section:

$$I_y \equiv \iint_A z^2 \; dA = b \int_{-\frac{h}{2}}^{\frac{h}{2}} z^2 \; dz = \frac{bh^3}{12} \,. \tag{2.10}$$

Noting the potential time dependence of the moment and curvature, the moment equation is written:

$$M(x,t) = EI_y \frac{\partial^2 w(x,t)}{\partial x^2} \,. \tag{2.11}$$

Turning now to the equilibrium of a representative beam segment as shown in Fig. 2.6, there are shear forces $\mathcal{V}$ and moments M acting at each end of the segment, as well as a distributed force intensity f acting throughout the length dx. In addition, the body inertial

force $\mathcal{B}_F$ and moment $\mathcal{B}_M$ are indicated in the figure.

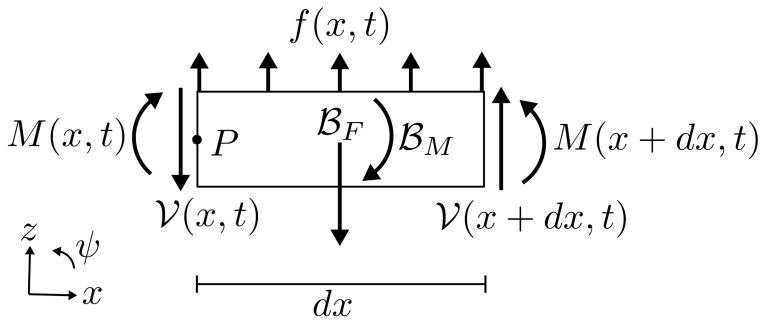

Figure 2.6: Equilibrium of a beam segment in bending.

The segment has a total mass of $\rho A\ dx$ where ρ is the volume density, so the body inertial force, which opposes motion in the positive z-direction, is $\mathcal{B}_F = \rho A \frac{\partial^2 w(x,t)}{\partial t^2} dx$. Force balance on the segment yields:

$$\begin{aligned} \mathcal{V}(x+dx,t) - \mathcal{V}(x,t) + f(x,t)\,dx - \rho A \frac{\partial^2 w(x,t)}{\partial t^2}\ dx = 0 \\ \frac{\partial \mathcal{V}(x,t)}{\partial x} = \rho A \frac{\partial^2 w(x,t)}{\partial t^2} - f(x,t)\ , \end{aligned} \tag{2.12}$$

where the second line is the result of dividing through by dx and taking the limit as $dx \to 0$. The body inertial moment, which opposes rotation in the positive ψ-direction, is written $\mathcal{B}_M = \rho I_y \frac{\partial^2 \psi(x,t)}{\partial t^2} dx$, so moment balance about point P on the segment results in:

$$M(x+dx,t) - M(x,t) + \mathcal{V}(x+dx,t)\,dx + f(x,t)\,\frac{dx^2}{2} - \rho I_y \frac{\partial^2 \psi(x,t)}{\partial t^2} dx = 0\,. \tag{2.13}$$

Rewriting the shear contribution term as $\left(\mathcal{V}(x,t) + \frac{\partial \mathcal{V}(x,t)}{\partial x} dx\right) dx$, the moment balance equa-

tion can be written as:

$$\begin{aligned} M\left(x+dx,t\right)-M\left(x,t\right)+\mathcal{V}\left(x,t\right)dx+\left(\frac{\partial\mathcal{V}\left(x,t\right)}{\partial x}+\frac{f\left(x,t\right)}{2}\right)dx^{2}&=\rho I_{y}\frac{\partial^{2}\psi\left(x,t\right)}{\partial t^{2}}dx \\ \mathcal{V}\left(x,t\right)+\frac{\partial M\left(x,t\right)}{\partial x}&=\rho I_{y}\frac{\partial^{2}\psi\left(x,t\right)}{\partial t^{2}}\,, \end{aligned} \tag{2.14}$$

where the second line is the result of dividing through by dx and taking the limit as $dx \to 0$. If the rotary inertia is assumed to be negligible, which is the case in Euler-Bernoulli beam theory, the right hand side of Eqn. 2.14 is zero. Taking the spatial derivative of that form and then substituting the result of Eqn. 2.12:

$$\begin{aligned} \frac{\partial\mathcal{V}\left(x,t\right)}{\partial x}+\frac{\partial^{2}M\left(x,t\right)}{\partial x^{2}}&=0 \\ \rho A\frac{\partial^{2}w\left(x,t\right)}{\partial t^{2}}-f\left(x,t\right)+\frac{\partial^{2}M\left(x,t\right)}{\partial x^{2}}&=0\,. \end{aligned} \tag{2.15}$$

Now taking two spatial derivatives of the moment equation, Eqn. 2.11, and substituting into Eqn. 2.15 yields the beam equation of motion:

$$\rho A\frac{\partial^{2}w\left(x,t\right)}{\partial t^{2}}+EI_{y}\frac{\partial^{4}w\left(x,t\right)}{\partial x^{4}}=f\left(x,t\right)\,. \tag{2.16}$$

A velocity proportional (viscous) damping term, with damping constant c, can also be included in the equation of motion:

$$\rho A\frac{\partial^{2}w\left(x,t\right)}{\partial t^{2}}+c\frac{\partial w\left(x,t\right)}{\partial t}+EI_{y}\frac{\partial^{4}w\left(x,t\right)}{\partial x^{4}}=f\left(x,t\right)\,. \tag{2.17}$$

Returning briefly to the axial strain equation, Eqn. 2.7, it can be seen that the absolute axial strain in the beam segment due to bending increases as the distance z from the neutral axis increases. Its maximum absolute value then occurs farthest from the beam's neutral

axis, i.e. at the top and bottom of the cross section:

$$\varepsilon_{xx,\max/\min}(x,t) = -\frac{h}{2} \cdot \frac{\partial^2 w(x,t)}{\partial x^2}. \tag{2.18}$$

In many sections of this thesis, the spatial dimension will be normalized with respect to the beam length, $\hat{x} = \frac{x}{l}$. The differential operator is then given by $\frac{d}{dx}(\cdot) = \frac{1}{l}\frac{d}{d\hat{x}}(\cdot)$. The beam equation of motion for this non-dimensional coordinate is thus:

$$\rho A \frac{\partial^2 w(\hat{x},t)}{\partial t^2} + c\frac{\partial w(\hat{x},t)}{\partial t} + \frac{EI_y}{l^4}\frac{\partial^4 w(\hat{x},t)}{\partial \hat{x}^4} = f(\hat{x},t), \tag{2.19}$$

and the maximum axial strain due to bending is given by:

$$\left|\varepsilon_{\hat{x}\hat{x},\max}(\hat{x},t)\right| = \frac{h}{2l^2} \cdot \frac{\partial^2 w(\hat{x},t)}{\partial \hat{x}^2}. \tag{2.20}$$

For all equations in which $\hat{x}$ appears, the usual volumetric density ρ should be interpreted as the density per unit length.

Energy Method

An alternative method to derive the beam equation of motion is through variational calculus and the energy method [35]. Following a similar procedure to determine the Lagrangian function as that used for discrete parameter systems, discussed in Appendices A and B, the kinetic energy T for the beam in bending (shown in Fig. 2.1) is:

$$T = \frac{1}{2}\int_0^l \iint_A \rho \left(\frac{\partial w}{\partial t}\right)^2 dA\, dx = \int_0^l \frac{\rho A}{2}\left(\frac{\partial w}{\partial t}\right)^2 dx, \tag{2.21}$$

where the contribution due to beam element rotation has been neglected. The strain energy stored in the beam, U, is:

$$U = \frac{1}{2}\iiint_V \tau_{ij}\varepsilon_{ij}\ dv = \frac{b}{2}\int_0^l \int_{-\frac{h}{2}}^{\frac{h}{2}} \tau_{xx}\varepsilon_{xx}\ dz\ dx\,, \tag{2.22}$$

where the stress τ_{ij} and strain ε_{ij} are assumed constant along the beam's width. Upon substituting Hooke's Law for a linear elastic material ($\tau_{xx} = E\varepsilon_{xx}$) and the result of Eqn. 2.7, Eqn. 2.22 can be rewritten:

$$U = \int_0^l \int_{-\frac{h}{2}}^{\frac{h}{2}} \frac{Eb}{2}\varepsilon_{xx}^2\ dz\ dx = \int_0^l \int_{-\frac{h}{2}}^{\frac{h}{2}} \frac{Eb}{2}\left[-z\cdot\frac{\partial^2 w}{\partial x^2}\right]^2 dz\ dx = \int_0^l \frac{EI_y}{2}\left(\frac{\partial^2 w}{\partial x^2}\right)^2 dx\,. \tag{2.23}$$

Finally, the work done by the applied load is:

$$V = -\int_0^l f(x,t)w(x,t)\ dx\,. \tag{2.24}$$

The Lagrangian function for this case is defined as:

$$L = T - U - V\,. \tag{2.25}$$

By the Hamilton principle [36], $\delta\int_{t_0}^{t_1} L\ dt = 0$, so:

$$\begin{aligned} 0 = \delta\int_{t_0}^{t_1} L\ dt &= \delta\int_{t_0}^{t_1}\int_0^l \left\{\frac{\rho A}{2}\left(\frac{\partial w}{\partial t}\right)^2 - \frac{EI_y}{2}\left(\frac{\partial^2 w}{\partial x^2}\right)^2 + fw\right\}\ dx\ dt \\ &= \int_{t_0}^{t_1}\int_0^l \left\{\rho A\dot{w}\ \delta\left(\frac{\partial w}{\partial t}\right) - EI_y\frac{\partial^2 w}{\partial x^2}\ \delta\left(\frac{\partial^2 w}{\partial x^2}\right) + f\ \delta w\right\}\ dx\ dt\,, \end{aligned} \tag{2.26}$$

where $(\dot{\ })$ indicates differentiation with respect to time. Integrating the first term by parts with respect to time:

$$\int_{t_0}^{t_1}\int_0^l \rho A\dot{w}\ \delta\left(\frac{\partial w}{\partial t}\right)\ dx\ dt = \int_0^l \left[\rho A\dot{w}\ \delta w\right]_{t_0}^{t_1}\ dx - \int_{t_0}^{t_1}\int_0^l \rho A\ddot{w}\ \delta w\ dx\ dt\,. \tag{2.27}$$

Since $\delta w = 0$ at t_0 and t_1, the first term on the right hand side is zero. The second term in Eqn. 2.26 can be integrated by parts with respect to x twice:

$$\begin{aligned}\int_{t_0}^{t_1}\int_0^l EI_y\frac{\partial^2 w}{\partial x^2}\;\delta\left(\frac{\partial^2 w}{\partial x^2}\right)\;dx\;dt &= \int_0^l -EI_y\frac{\partial^3 w}{\partial x^3}\;\delta\left(\frac{\partial w}{\partial x}\right)\;dx + \left[EI_y\frac{\partial^2 w}{\partial x^2}\;\delta\left(\frac{\partial w}{\partial x}\right)\right]_0^l \\ &= \int_0^l EI_y\frac{\partial^4 w}{\partial x^4}\;\delta w\;dx \\ &\quad + \left[EI_y\frac{\partial^2 w}{\partial x^2}\;\delta\left(\frac{\partial w}{\partial x}\right)\right]_0^l - \left[EI_y\frac{\partial^3 w}{\partial x^3}\;\delta w\right]_0^l .\end{aligned} \tag{2.28}$$

Now substituting Eqns. 2.27 and 2.28 into Eqn. 2.26:

$$\begin{aligned}0 = \delta\int_{t_0}^{t_1} L\;dt = \int_{t_0}^{t_1}\int_0^l &\left\{-\rho A\ddot{w} - EI_y\frac{\partial^4 w}{\partial x^4} + f\right\}\delta w\;dx\;dt \\ &+ \left[EI_y\frac{\partial^3 w}{\partial x^3}\;\delta w\right]_0^l - \left[EI_y\frac{\partial^2 w}{\partial x^2}\;\delta\left(\frac{\partial w}{\partial x}\right)\right]_0^l .\end{aligned} \tag{2.29}$$

This equation results in the same governing equation as for the Newton/Euler Method as well as the boundary conditions:

$$\begin{aligned}\rho A\frac{\partial^2 w\,(x,t)}{\partial t^2} + EI_y\frac{\partial^4 w\,(x,t)}{\partial x^4} &= f\,(x,t) \\ \left[EI_y\frac{\partial^3 w\,(x,t)}{\partial x^3}\;\delta w\,(x,t)\right]_0^l &= 0 \\ \left[EI_y\frac{\partial^2 w\,(x,t)}{\partial x^2}\;\delta\left(\frac{\partial w\,(x,t)}{\partial x}\right)\right]_0^l &= 0\,.\end{aligned} \tag{2.30}$$

As before, an ideal (viscous) damping term can also be added to this model. One key advantage of this method, in comparison to the Newton/Euler Method, is that the possible boundary conditions are determined during the solution process. As shown here, the boundary conditions at $x = 0$ and $x = l$ require that: (1) either the shear is zero or the deflection is prescribed and (2) either the moment is zero or the slope is prescribed.

2.2.2 Static Solution

For a static beam, the time derivative terms $\rho A\frac{\partial^2 w(\hat{x},t)}{\partial t^2}$ and $c\frac{\partial w(\hat{x},t)}{\partial t}$ in Eqn. 2.19 are zero, and the transverse centerline deflection is only a function of the longitudinal domain. The solution can then be determined by direct integration:

$$w\left(\hat{x}\right) = \frac{l^4}{EI_y}\left(\frac{C_1}{6}\hat{x}^3 + \frac{C_2}{2}\hat{x}^2 + C_3\hat{x} + C_4\right) , \tag{2.31}$$

where the constants C_1, C_2, C_3, and C_4 are determined based on the boundary conditions. For a cantilever beam with a tip load F, these boundary conditions are:

$$\begin{aligned} w\left(0\right) &= 0 & \left.\frac{d^2w(\hat{x})}{d^2\hat{x}}\right|_{\hat{x}=1} &= 0 \\ \left.\frac{dw(\hat{x})}{d\hat{x}}\right|_{\hat{x}=0} &= 0 & \frac{EI_y}{l^3}\left.\frac{d^3w(\hat{x})}{d^3\hat{x}}\right|_{\hat{x}=1} &= -F\,. \end{aligned} \tag{2.32}$$

Solving for the constants of integration results in the following static transverse deflection equation:

$$w\left(\hat{x}\right) = \frac{Fl^3}{6EI_y}\hat{x}^2\left(3-\hat{x}\right) . \tag{2.33}$$

Differentiating twice with respect to x yields the curvature:

$$\frac{d^2w(\hat{x})}{dx^2} = \frac{1}{l^2}\frac{d^2w(\hat{x})}{d\hat{x}^2} = \frac{Fl}{EI_y}\left(1-\hat{x}\right) . \tag{2.34}$$

The static deflection and curvature for a tip load, normalized to have a maximum value of 1, are shown in Fig. 2.7. By Eqn. 2.7, the curvature is proportional to the normal strain in the beam and will thus be important in Chapter 3 for comparison with the experimental static strain distribution.

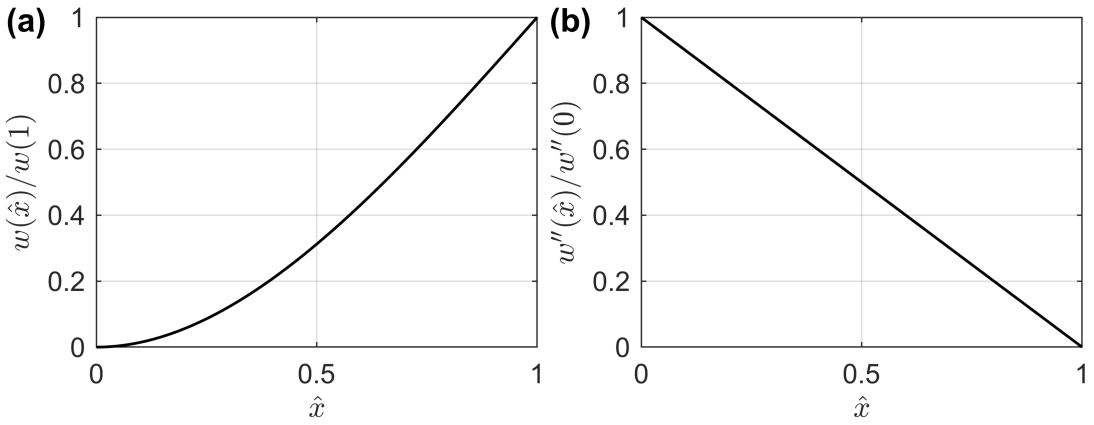

Figure 2.7: Normalized static (a) deflection and (b) curvature shapes of a cantilever beam for a point tip load.

2.2.3 Dynamic Solution

The unforced and undamped form of Eqn. 2.19 can be written:

$$\frac{\partial^2 w\left(\hat{x},t\right)}{\partial t^2} + \frac{EI_y}{\rho A l^4}\frac{\partial^4 w\left(\hat{x},t\right)}{\partial \hat{x}^4} = 0\,. \tag{2.35}$$

The boundary conditions corresponding to a cantilever beam are given below, where the beam is clamped at $\hat{x} = 0$ and free at $\hat{x} = 1$:

$$\begin{aligned} w\left(0,t\right) &= 0 \qquad \left.\frac{\partial^2 w(\hat{x},t)}{\partial \hat{x}^2}\right|_{\hat{x}=1} = 0 \\ \left.\frac{\partial w(\hat{x},t)}{\partial \hat{x}}\right|_{\hat{x}=0} &= 0 \qquad \left.\frac{\partial^3 w(\hat{x},t)}{\partial \hat{x}^3}\right|_{\hat{x}=1} = 0\,. \end{aligned} \tag{2.36}$$

These boundary conditions correspond to zero deflection and slope at the root, and zero moment and shear at the tip.

Following the separation of variables method, an assumed solution of the form $w\left(\hat{x},t\right) =$

$\phi(\hat{x})\,\eta(t)$ is substituted into the governing equation and then rearranged:

$$\begin{aligned} \phi\ddot{\eta} + \frac{EI_y}{\rho A l^4}\phi''''\eta &= 0 \\ \Rightarrow \frac{EI_y}{\rho A l^4}\frac{\phi''''}{\phi} &= -\frac{\ddot{\eta}}{\eta} = \omega^2\,, \end{aligned} \tag{2.37}$$

where differentiation is with respect to $\hat{x}$ for ϕ and t for η. Since both sides of the second equation are equal, yet functions of different variables, they must be equal to a constant, here called ω^2. The boundary conditions given in Eqn. 2.36 can also be rewritten in terms of $\phi(\hat{x})$:

$$\begin{array}{lllllll} w(0,t) & = \phi(0)\,\eta(t) & = 0 & \Rightarrow & \phi(0) & = 0 \\ \left.\frac{\partial w(\hat{x},t)}{\partial \hat{x}}\right|_{\hat{x}=0} & = \left.\frac{\partial \phi(\hat{x})}{\partial \hat{x}}\right|_{\hat{x}=0}\eta(t) & = 0 & \Rightarrow & \left.\frac{\partial \phi(\hat{x})}{\partial \hat{x}}\right|_{\hat{x}=0} & = 0 \\ \left.\frac{\partial^2 w(\hat{x},t)}{\partial \hat{x}^2}\right|_{\hat{x}=1} & = \left.\frac{\partial^2 \phi(\hat{x})}{\partial \hat{x}^2}\right|_{\hat{x}=1}\eta(t) & = 0 & \Rightarrow & \left.\frac{\partial^2 \phi(\hat{x})}{\partial \hat{x}^2}\right|_{\hat{x}=1} & = 0 \\ \left.\frac{\partial^3 w(\hat{x},t)}{\partial \hat{x}^3}\right|_{\hat{x}=1} & = \left.\frac{\partial^3 \phi(\hat{x},t)}{\partial \hat{x}^3}\right|_{\hat{x}=1}\eta(t) & = 0 & \Rightarrow & \left.\frac{\partial^3 \phi(\hat{x},t)}{\partial \hat{x}^3}\right|_{\hat{x}=1} & = 0\,, \end{array} \tag{2.38}$$

since for all of these cases, $\eta(t)$ cannot equal zero for all t. Two equations can be written using Eqn. 2.37:

$$\begin{aligned} \ddot{\eta} + \omega^2\eta &= 0 \\ \phi'''' - \left(\frac{\rho A l^4 \omega^2}{EI_y}\right)\phi &= 0\,. \end{aligned} \tag{2.39}$$

In this solution process, it is convenient to define a term known as the weighted frequency:

$$\xi = \sqrt[4]{\frac{\rho A l^4 \omega^2}{EI_y}}\,. \tag{2.40}$$

Spatial Solution

The second differential equation given in Eqn. 2.39 can be written:

$$\begin{aligned} \phi'''' - \xi^4 \phi &= 0 \\ \left(\mathcal{L} - \xi^4\right) \phi &= 0\,, \end{aligned} \tag{2.41}$$

where $\mathcal{L}$ is the linear operator defined as $\mathcal{L} = \frac{d^4}{d\hat{x}^4}$. The form given in the second line demonstrates the correspondence between the matrix eigenproblem solved for MDOF systems (described in Appendix B) and that formulated here for continuous functions. Where the solution in the matrix case requires determining the eigenvector which when multiplied by a linear transformation only scales that eigenvector, the solution here requires determining the function ϕ which is only scaled after applying the linear transformation $\mathcal{L}$. In the form shown in Eqn. 2.41, ξ^4 is the eigenvalue. The distributed parameter vibration problem can thereby be interpreted as an eigenproblem.

The characteristic polynomial of the differential equation in Eqn. 2.41 is $r^4 - \xi^4 = 0$, whose solutions are $r = \{\pm\xi,\ \pm j\xi\}$ where j is the imaginary unit. Thus, the solution to this differential equation, and eigenfunction of Eqn. 2.41, is [37]:

$$\phi\left(\hat{x}\right) = C_1 \sin \xi\hat{x} + C_2 \cos \xi\hat{x} + C_3 \sinh \xi\hat{x} + C_4 \cosh \xi\hat{x}\,, \tag{2.42}$$

where C_1, C_2, C_3, and C_4 are constants to be determined from the boundary conditions.

Evaluating each of the boundary conditions given in Eqn. 2.38:

1. $\phi\left(0\right) = 0$

$$C_2 + C_4 = 0 \Rightarrow C_4 = -C_2 \tag{2.43}$$

2. $\left.\frac{\partial\phi(\hat{x})}{\partial\hat{x}}\right|_{\hat{x}=0} = 0$

$$C_1 + C_3 = 0 \Rightarrow C_3 = -C_1 \tag{2.44}$$

Collecting the previous two results, Eqn. 2.42 can be written:

$$\phi(\hat{x}) = C_1(\sin\xi\hat{x} - \sinh\xi\hat{x}) + C_2(\cos\xi\hat{x} - \cosh\xi\hat{x}) \ . \tag{2.45}$$

3. $\left.\frac{\partial^2\phi(\hat{x})}{\partial\hat{x}^2}\right|_{\hat{x}=1} = 0$

$$\begin{aligned} C_1(\sin\xi + \sinh\xi) + C_2(\cos\xi + \cosh\xi) &= 0 \\ \Rightarrow C_1 &= -C_2\left(\frac{\cos\xi + \cosh\xi}{\sin\xi + \sinh\xi}\right) \end{aligned} \tag{2.46}$$

Substituting this result into Eqn. 2.45:

$$\phi(\hat{x}) = C_2\left(\cos\xi\hat{x} - \cosh\xi\hat{x} - \left(\frac{\cos\xi + \cosh\xi}{\sin\xi + \sinh\xi}\right)(\sin\xi\hat{x} - \sinh\xi\hat{x})\right) \ . \tag{2.47}$$

The constant C_2 is an arbitrary scaling factor, which can be chosen to normalize the mode shape as desired. Choosing here $C_2 = 1$ yields the mode shape:

$$\phi(\hat{x}) = \cos\xi\hat{x} - \cosh\xi\hat{x} - \left(\frac{\cos\xi + \cosh\xi}{\sin\xi + \sinh\xi}\right)(\sin\xi\hat{x} - \sinh\xi\hat{x}) \ . \tag{2.48}$$

where ξ will be determined next based on the final boundary condition.

4. $\left.\frac{\partial^3\phi(\hat{x},t)}{\partial\hat{x}^3}\right|_{\hat{x}=1} = 0$

$$C_2\left(\sin\xi - \sinh\xi + \left(\frac{\cos\xi + \cosh\xi}{\sin\xi + \sinh\xi}\right)(\cos\xi + \cosh\xi)\right) = 0 \tag{2.49}$$

Since $C_2 = 0$ would lead to a trivial solution:

$$\begin{aligned}
\sin\xi - \sinh\xi + \left(\frac{\cos\xi + \cosh\xi}{\sin\xi + \sinh\xi}\right)(\cos\xi + \cosh\xi) &= 0 \\
(\cos\xi + \cosh\xi)^2 &= \sinh^2\xi - \sin^2\xi \\
\cos^2\xi + \sin^2\xi + 2\cos\xi\cosh\xi &= \sinh^2\xi - \cosh^2\xi \\
1 + 2\cos\xi\cosh\xi &= -1 \\
2(1 + \cos\xi\cosh\xi) &= 0 \\
1 + \cos\xi\cosh\xi &= 0\,.
\end{aligned} \tag{2.50}$$

The last line of Eqn. 2.50 is known as the characteristic equation, which is transcendental and has infinitely many solutions. The first several solutions are:

$$\xi = \{1.87510407, 4.69409113, 7.85475744, 10.99554073, 14.13716839, \ldots\}\ . \tag{2.51}$$

To summarize the above results for the spatial solution, the clamped-free characteristic equation is given by:

$$1 + \cos\xi_r\cosh\xi_r = 0\,, \tag{2.52}$$

which has an infinite number of solutions ξ_r. The corresponding mode shapes are given by:

$$\phi_r(\hat{x}) = \cos\xi_r\hat{x} - \cosh\xi_r\hat{x} - \left(\frac{\cos\xi_r + \cosh\xi_r}{\sin\xi_r + \sinh\xi_r}\right)(\sin\xi_r\hat{x} - \sinh\xi_r\hat{x})\ . \tag{2.53}$$

The first four normalized mode shapes are plotted in Fig. 2.8 along with their corresponding curvature shapes (given by the second derivative of the mode shapes). As will be shown in Chapter 3, these curvature shapes are directly related to the strain distributions and can be measured with distributed strain sensors.

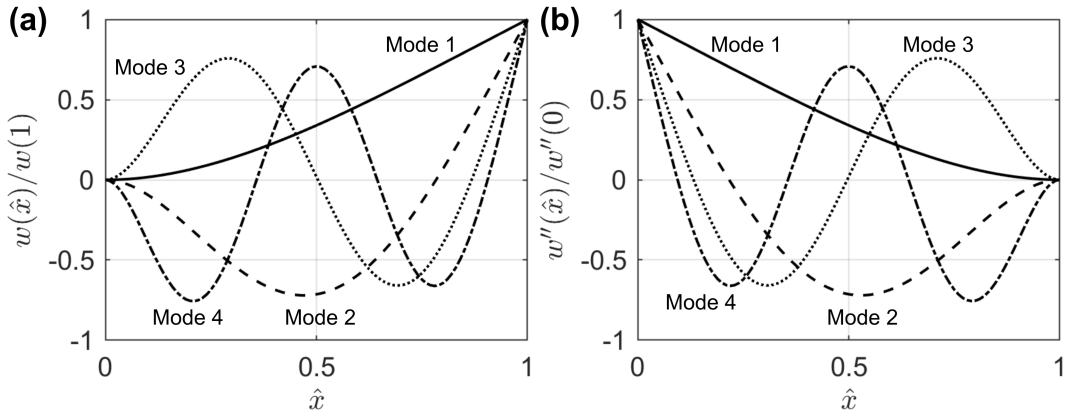

Figure 2.8: Normalized dynamic (a) mode and (b) curvature shapes of a cantilever beam.

Finally, from Eqn. 2.40, the corresponding natural frequencies are:

$$\omega_r = \left(\sqrt{\frac{EI_y}{\rho A l^4}}\right) \xi_r^2 \,. \tag{2.54}$$

Time Solution

The first differential equation given in Eqn. 2.39 can be written:

$$\ddot{\eta}_r + \omega_r^2 \eta_r = 0 \,, \tag{2.55}$$

where η_r is known as the r-th modal coordinate, based on its interpretation as the contribution of the r-th mode to the total response. The characteristic polynomial of this differential equation is $r^2 + \omega_r^2 = 0$, whose solutions are $r = \pm j\omega_r$. Thus, the solution to this differential equation is [37]:

$$\eta_r(t) = a_r \sin \omega_r t + b_r \cos \omega_r t \,, \tag{2.56}$$

where a_r and b_r are constants for each mode determined from the initial conditions.

Total Free Solution

From the above results given in Eqn. 2.53 and Eqn. 2.56, the total solution can be formed as the infinite sum:

$$w\left(\hat{x},t\right)=\sum_{r=1}^{\infty}\eta_r\left(t\right)\phi_r\left(\hat{x}\right)\,. \tag{2.57}$$

The total response is thus the sum of each modal coordinate η_r multiplied by its mode shape ϕ_r.

Forced Solution

Extending the free solution developed above to the case of forced vibration leads to a forced version of the differential equations for the modal coordinates. Substituting the total solution given in Eqn. 2.57 into the undamped form of Eqn. 2.19 results in:

$$\begin{aligned}\sum_{r=1}^{\infty}\left[\rho A\ddot{\eta}_r\phi_r\left(\hat{x}\right)+\frac{EI_y}{l^4}\eta_r\phi_r''''(\hat{x})\right]&=f\left(\hat{x},t\right)\\ \rho A\sum_{r=1}^{\infty}\left(\ddot{\eta}_r+\omega_r^2\eta_r\right)\phi_r\left(\hat{x}\right)&=f\left(\hat{x},t\right)\,,\end{aligned} \tag{2.58}$$

where by Eqn. 2.41:

$$\phi''''=\xi^4\phi=\frac{\rho Al^4\omega^2}{EI_y}\phi\,. \tag{2.59}$$

Multiplying by an arbitrary mode ϕ_s, integrating over the beam's domain Ω, and dividing through by ρA results in:

$$\ddot{\eta}_r+\omega_r^2\eta_r=\frac{1}{\rho A}\int_0^1 f\left(\hat{x},t\right)\phi_r\left(\hat{x}\right)\;d\hat{x}\,, \tag{2.60}$$

where the infinite sum is eliminated by the orthogonality of the mode shapes:

$$\int_\Omega\phi_s\phi_r\;d\hat{x}=\begin{cases}1, & s=r\\ 0, & s\neq r\,.\end{cases} \tag{2.61}$$

This second order ordinary differential equation describes the response of the r-th modal coordinate to the forcing function f. The modal forcing function can thus be defined as:

$$F_r(t) \equiv \int_0^1 f(\hat{x}, t)\, \phi_r(\hat{x})\ d\hat{x}\,, \tag{2.62}$$

yielding the following differential equation for the r-th modal coordinate:

$$\ddot{\eta}_r + \omega_r^2 \eta_r = \frac{1}{\rho A} F_r(t)\ . \tag{2.63}$$

If the forcing function strictly acts at a point $\hat{x}_f$, then it can be written $f(\hat{x}, t) = \delta(\hat{x} - \hat{x}_f)F(t)$ and the modal forcing function is:

$$F_r(t) = F(t) \int_0^1 \delta(\hat{x} - \hat{x}_f)\phi_r(\hat{x})\ d\hat{x} = F(t)\phi_r(\hat{x}_f)\,. \tag{2.64}$$

Thus if the amplitude of the r-th mode at $\hat{x}_f$ is zero ($\phi_r(\hat{x}_f) = 0$), the applied point force F can not excite that mode. In other words, if the force is applied at a mode's nodal point, that mode will not be excited.

2.2.4 Single Degree of Freedom Model

The transverse motion of the tip of a cantilever beam can be represented by an SDOF model, and analyzed using the techniques reviewed in Appendix A. The SDOF model, which is represented in Fig. A.1, is governed by the equation of motion:

$$m_{\text{eff}}\ddot{w} + c\dot{w} + k_{\text{eff}} w = F(t)\ , \tag{2.65}$$

where the effective mass m_{eff}, damping constant c, and effective stiffness k_{eff} of the system must be determined to produce a dynamically equivalent response to the behavior of the beam tip in the distributed parameter model. As discussed in Appendix A, models of damping are generally inaccurate in estimating the empirical system damping, and matching

this system parameter is most accurately accomplished empirically.

The effective tip stiffness, defined as the ratio of the force acting at the tip to the corresponding deflection, is determined by considering the static deflection equation given in Eqn. 2.33:

$$k_{\text{eff}} = \frac{F}{w\,(1)} = F \cdot \frac{3EI_y}{Fl^3} = \frac{3EI_y}{l^3}\,. \tag{2.66}$$

Determining the effective mass of the system is slightly more involved. It is assumed here that the deflection w of the first bending mode can be approximated by the static deflection curve of Eqn. 2.33. The kinetic energy is then given by $T = \frac{1}{2}\int_\Omega \dot{w}^2\ dm$. The static deflection equation can be rewritten in terms of the deflection at the tip of the beam, $w\,(1)$, and then differentiated to write an expression for the velocity:

$$\begin{aligned} w\,(\hat{x}) &= \frac{Fl^3}{6EI_y}\hat{x}^2\,(3-\hat{x}) = \frac{w(1)}{2}\hat{x}^2\,(3-\hat{x}) \\ \Rightarrow \dot{w}\,(\hat{x}) &= \frac{\dot{w}(1)}{2}\hat{x}^2\,(3-\hat{x})\ . \end{aligned} \tag{2.67}$$

Substituting this expression into the equation for the kinetic energy results in:

$$\begin{aligned} T &= \frac{1}{2}\int_\Omega \dot{w}^2\ dm \\ &= \frac{\rho Al}{2}\int_0^1 \left(\frac{\dot{w}(1)}{2}\hat{x}^2\,(3-\hat{x})\right)^2\ d\hat{x} \\ &= \frac{\rho Al}{8}\left[\int_0^1 \hat{x}^4\,(3-\hat{x})^2\ d\hat{x}\right]\dot{w}(1)^2 \\ &= \frac{\rho Al}{8}\left[\int_0^1 \hat{x}^6 - 6\hat{x}^5 + 9\hat{x}^4\ d\hat{x}\right]\dot{w}(1)^2 \\ &= \frac{\rho Al}{8}\left[\frac{1}{7} - 1 + \frac{9}{5}\right]\dot{w}(1)^2 \\ &= \frac{1}{2}\left[\frac{33}{140}\rho Al\right]\dot{w}(1)^2\,, \end{aligned} \tag{2.68}$$

where $dm = \rho A\ dx = \rho Al\ d\hat{x}$. By analogy with the kinetic energy of an SDOF system,

$T = \frac{1}{2}mv^2$, the effective mass of the cantilever beam acting at the tip is:

$$m_{\text{eff}} = \frac{33}{140}\rho A l \,. \tag{2.69}$$

Based on these system parameters, the natural frequency of the SDOF system is:

$$\omega_n = \sqrt{\frac{k_{\text{eff}}}{m_{\text{eff}}}} = \left(\sqrt{\frac{EI_y}{\rho A l^4}}\right)\sqrt{\frac{420}{33}}\,, \tag{2.70}$$

and the non-dimensional form of the SDOF equation of motion given in Eqn. 2.65 can be written:

$$\ddot{w} + 2\zeta\omega_n\dot{w} + \omega_n^2 w = \frac{1}{m_{\text{eff}}}F(t)\ , \tag{2.71}$$

where ζ is the damping ratio.

2.2.5 Multiple Degrees of Freedom Model: Multiple Bending Modes

The total response given in Eqn. 2.57 can be split into an N-term truncated model w_N and associated residual w_R [38]:

$$\begin{array}{rcccc} w(\hat{x},t) & = & \sum_{r=1}^{N}\eta_r(t)\,\phi_r(\hat{x}) & + & \sum_{r=N+1}^{\infty}\eta_r(t)\,\phi_r(\hat{x}) \\ & = & w_N(\hat{x},t) & + & w_R(\hat{x},t)\ . \end{array} \tag{2.72}$$

Following the process outlined for determining the forced response, the truncated model can be substituted into the equation of motion and simplified to yield N equations of the form given by Eqn. 2.63, where the truncated total response is then expressed as the sum of the N modal coordinates η_r multiplied by their corresponding mode shapes. For a particular system it is almost always the case that only a certain frequency range is of interest, and modes with natural frequencies significantly higher than this range can be grouped in the residual term without significant impact on the truncated model. This result underpins the rationale (and accuracy) of reduced order, truncated, modeling procedures.

2.2.6 Orthogonality of Mode Shapes

The property of orthogonality, invoked above without proof for the beam mode shapes, permits the decoupling of the total response into a summation of contributions from individual modes. This property can be proved in two parts: (1) if $s \neq r$, then $\int_\Omega \phi_s \phi_s \, d\hat{x} = 0$ and (2) $\int_\Omega \phi_s^2 \, d\hat{x} = h$ for some constant h. The constant h is arbitrary, as the scaling of the mode shapes is arbitrary. Here, however, the scaling choice of $C_2 = 1$ will be used to arrive at the result of Eqn. 2.61.

1. $\int_\Omega \phi_s \phi_s \, d\hat{x} = 0$ for $s \neq r$

   Consider the spatial governing differential equation given in Eqn. 2.41, which states that all modes must satisfy $\phi_r'''' = \xi_r^4 \phi_r$ where the derivative is taken with respect to the non-dimensional length coordinate $\hat{x}$. The integral of $\xi_r^4 \int_\Omega \phi_s \phi_r \, d\hat{x}$ can then be written as:

   $$\xi_r^4 \int_\Omega \phi_s \phi_r \, d\hat{x} = \int_\Omega \phi_s \phi_r'''' \, d\hat{x} \,. \tag{2.73}$$

   Integrating by parts the right hand side of the above equation four times results in:

   $$\xi_r^4 \int_\Omega \phi_s \phi_r \, d\hat{x} = [\phi_s \phi_r''' - \phi_s' \phi_r'' + \phi_s'' \phi_r' - \phi_s''' \phi_r]_0^1 + \xi_s^4 \int_\Omega \phi_s \phi_r \, d\hat{x} \,, \tag{2.74}$$

   where $\phi_s'''' = \xi_s^4 \phi_s$ has been substituted. Each of the terms in the square brackets can be eliminated due to the boundary conditions of the cantilever beam, which state that $\phi_i = \phi_i' = 0$ at $\hat{x} = 0$ and that $\phi_i'' = \phi_i''' = 0$ at $\hat{x} = 1$. Upon rearrangement, Eqn. 2.74 can then be written:

   $$\left(\xi_r^4 - \xi_s^4\right) \int_\Omega \phi_s \phi_r \, d\hat{x} = 0 \,. \tag{2.75}$$

   Since $\xi_s \neq \xi_r$ when $s \neq r$, this equality is true if and only if $\int_\Omega \phi_s \phi_s \, d\hat{x} = 0$.

2. $\int_\Omega \phi_s^2 \, d\hat{x} = 1$

   This result requires significantly more steps as a number of trigonometric integrals

must be computed. Begin by defining three terms:

$$\begin{aligned} P_1 &= \left(\cos\xi_s\hat{x} - \cosh\xi_s\hat{x}\right)^2 \\ P_2 &= \mu^2\left(\sin\xi_s\hat{x} - \sinh\xi_s\hat{x}\right)^2 \\ P_3 &= -2\mu\left(\cos\xi_s\hat{x} - \cosh\xi_s\hat{x}\right)\left(\sin\xi_s\hat{x} - \sinh\xi_s\hat{x}\right) \ , \end{aligned} \tag{2.76}$$

where $\mu \equiv \frac{\cos\xi_s+\cosh\xi_s}{\sin\xi_s+\sinh\xi_s}$. The sum of these three terms is ϕ_s^2. Evaluating and summing the integrals for each of these terms will then yield the result for the integral of the squared mode shape. Several trigonometric integrals will be useful in determining this result:

$$\begin{aligned} \int_\Omega \cos^2\xi_s\hat{x}\ d\hat{x} &= \tfrac{1}{2} + \tfrac{\sin\xi_s\cos\xi_s}{2\xi_s} \\ \int_\Omega \cos\xi_s\hat{x}\cosh\xi_s\hat{x}\ d\hat{x} &= \tfrac{\cos\xi_s\sinh\xi_s+\sin\xi_s\cosh\xi_s}{2\xi_s} \\ \int_\Omega \cosh^2\xi_s\hat{x}\ d\hat{x} &= \tfrac{1}{2} + \tfrac{\sinh\xi_s\cosh\xi_s}{2\xi_s} \\ \int_\Omega \sin^2\xi_s\hat{x}\ d\hat{x} &= \tfrac{1}{2} - \tfrac{\sin\xi_s\cos\xi_s}{2\xi_s} \\ \int_\Omega \sin\xi_s\hat{x}\sinh\xi_s\hat{x}\ d\hat{x} &= \tfrac{\sin\xi_s\cosh\xi_s-\cos\xi_s\sinh\xi_s}{2\xi_s} \\ \int_\Omega \sinh^2\xi_s\hat{x}\ d\hat{x} &= -\tfrac{1}{2} + \tfrac{\sinh\xi_s\cosh\xi_s}{2\xi_s} \\ \int_\Omega \cos\xi_s\hat{x}\sin\xi_s\hat{x}\ d\hat{x} &= \tfrac{\sin^2\xi_s}{2\xi_s} \\ \int_\Omega \sin\xi_s\hat{x}\cosh\xi_s\hat{x}\ d\hat{x} &= \tfrac{\sin\xi_s\sinh\xi_s+2}{2\xi_s} \\ \int_\Omega \cos\xi_s\hat{x}\sinh\xi_s\hat{x}\ d\hat{x} &= \tfrac{\sin\xi_s\sinh\xi_s-2}{2\xi_s} \\ \int_\Omega \cosh\xi_s\hat{x}\sinh\xi_s\hat{x}\ d\hat{x} &= \tfrac{\sinh^2\xi_s}{2\xi_s} \ . \end{aligned} \tag{2.77}$$

Integrating the expanded form of each of P_1, P_2, and P_3 using these relationships results in:

$$\begin{aligned} \int_\Omega P_1\ d\hat{x} &= 1 + \frac{\sin\xi_s\cos\xi_s + \sinh\xi_s\cosh\xi_s - 2\cos\xi_s\sinh\xi_s - 2\sin\xi_s\cosh\xi_s}{2\xi_s} \\ \int_\Omega P_2\ d\hat{x} &= \mu^2\left(\frac{\sinh\xi_s\cosh\xi_s - \sin\xi_s\cos\xi_s - 2\sin\xi_s\cosh\xi_s + 2\cos\xi_s\sinh\xi_s}{2\xi_s}\right) \\ \int_\Omega P_3\ d\hat{x} &= -\frac{\mu}{\xi_s}\left(\sin\xi_s - \sinh\xi_s\right)^2 \ . \end{aligned} \tag{2.78}$$

Consider now the sum of the second integral and the second term of the first integral:

$$S = \frac{(1-\mu^2)\left(\sin\xi_s\cos\xi_s - 2\cos\xi_s\sinh\xi_s\right) + (1+\mu^2)\left(\sinh\xi_s\cosh\xi_s - 2\sin\xi_s\cosh\xi_s\right)}{2\xi_s}\,. \tag{2.79}$$

By the definition of μ:

$$\begin{aligned} 1-\mu^2 &= 1 - \frac{\cos^2\xi_s + 2\cos\xi_s\cosh\xi_s + \cosh^2\xi_s}{\left(\sin\xi_s\sinh\xi_s\right)^2} = \frac{2\sin\xi_s}{\sin\xi_s + \sinh\xi_s} \\ 1+\mu^2 &= 1 + \frac{\cos^2\xi_s + 2\cos\xi_s\cosh\xi_s + \cosh^2\xi_s}{\left(\sin\xi_s + \sinh\xi_s\right)^2} = \frac{2\sinh\xi_s}{\sin\xi_s + \sinh\xi_s}\,, \end{aligned} \tag{2.80}$$

where the characteristic equation, $\cos\xi_s\cosh\xi_s = -1$ and the Pythagorean identity has been used. Substituting these relationships into Eqn. 2.79 and regrouping:

$$S = \frac{\sin^2\xi_s\cos\xi_s + \sinh^2\xi_s\cosh\xi_s - 2\left(\cos\xi_s + \cosh\xi_s\right)\sin\xi_s\sinh\xi_s}{\xi_s\left(\sin\xi_s + \sinh\xi_s\right)}\,. \tag{2.81}$$

Multiplying the characteristic equation by $\cos\xi_s$ or $\cosh\xi_s$, applying trigonometric identities, and rearranging leads to the following two relationships:

$$\begin{aligned} \cos\xi_s + \cosh\xi_s &= \sin^2\xi_s\cosh\xi_s \\ \cos\xi_s + \cosh\xi_s &= -\sinh^2\xi_s\cos\xi_s\,. \end{aligned} \tag{2.82}$$

Using these relationships, substitutions can be made for $\sin^2\xi_s$ and $\sinh^2\xi_s$ in Eqn. 2.81:

$$\begin{aligned} S &= \frac{\mu}{\xi_s}\left(\frac{\cos\xi_s}{\cosh\xi_s} - \frac{\cosh\xi_s}{\cos\xi_s} - 2\sin\xi_s\sinh\xi_s\right) \\ &= \frac{\mu}{\xi_s}\left(\frac{\cos^2\xi_s - \cosh^2\xi_s}{\cos\xi_s\cosh\xi_s} - 2\sin\xi_s\sinh\xi_s\right) \\ &= \frac{\mu}{\xi_s}\left(\sin^2\xi_s + \sinh^2\xi_s - 2\sin\xi_s\sinh\xi_s\right) \\ &= \frac{\mu}{\xi_s}\left(\sin\xi_s - \sinh\xi_s\right)^2\,, \end{aligned} \tag{2.83}$$

where the characteristic equation has been used again.

Since S and the third integral in Eqn. 2.78 sum to zero, the only term remaining in the sum of P_1, P_2, and P_3 is 1, thus:

$$\int_{\Omega} \phi_s^2 \, d\hat{x} = 1 \, . \tag{2.84}$$

2.2.7 Comparison of Models

The first natural frequency for bending in a cantilever beam is predicted by Eqn. 2.54 for the distributed parameter model and by Eqn. 2.70 for the SDOF lumped parameter model. The ratio of these predictions is:

$$\frac{\omega_{n,\text{sdof}}}{\omega_{n,\text{dist.}}} = \left(\sqrt{\frac{EI_y}{\rho A l^4}}\right) \sqrt{\frac{420}{33}} \cdot \left(\sqrt{\frac{\rho A l^4}{EI_y}}\right) \frac{1}{\xi_1^2} = \sqrt{\frac{420}{33\xi_1^4}} \approx 1.0147 \, , \tag{2.85}$$

where ξ_1 is the first solution to the characteristic equation, Eqn. 2.52. Based on this result, the SDOF model over predicts the natural frequency by approximately 1.5% in comparison to the distributed parameter model. This over prediction is a result of additional stiffness introduced in the SDOF model from assuming the static deflection as the mode of vibration.

2.3 Torsional Vibration of a Cantilever Beam

Following a similar format as in the previous section, the equation of motion for the torsional vibration of a cantilever beam and its associated static and dynamic solutions are derived in this section. An SDOF model is then discussed as well as an uncoupled MDOF model which combines bending and torsional vibration. This section ends with a comparison of the natural frequency predictions based on the SDOF and distributed parameter models.

2.3.1 Distributed Parameter Model

Consider the cantilever beam schematic shown in Fig. 2.9. The torsional vibration of this system refers to the angular twist about the beam's centerline, here denoted as θ.

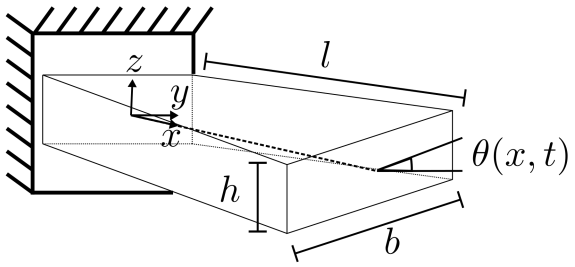

Figure 2.9: Schematic of a cantilever beam in torsion.

In the torsional vibration model described here, cross sections of the beam are assumed to rotate as rigid bodies with no warping in the x-direction. This is only an approximation for beams of rectangular cross section – the effect of warping is considered in Chapter 3 in the discussion of plate twisting.

Newton/Euler Method

Beginning with the equilibrium of a representative beam segment as shown in Fig. 2.10, there is a torque $\mathcal{T}$ acting at each end of the segment and a distributed external moment M acting throughout the length dx [39].

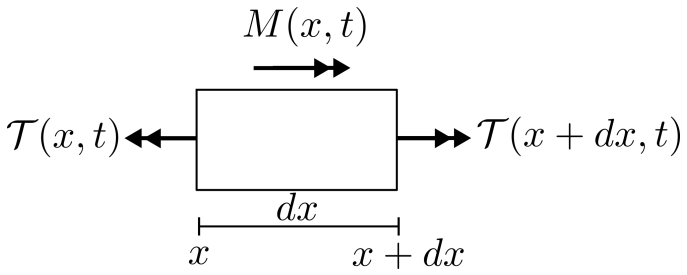

Figure 2.10: Equilibrium of a beam segment in torsion.

The polar mass moment of inertia about the x-axis is given by $\rho I_x\, dx$ where I_x is the second polar moment of area. For a rectangular cross section of dimensions b and h, the second polar moment of area is:

$$I_x = \int_{-\frac{h}{2}}^{\frac{h}{2}} \int_{-\frac{b}{2}}^{\frac{b}{2}} \left(x^2+y^2\right)\, dx\, dy = \int_{-\frac{h}{2}}^{\frac{h}{2}} \left[\frac{x^3}{3}+xy^2\right]_{-\frac{b}{2}}^{\frac{b}{2}} dy = \left[\frac{b^3 y}{12}+\frac{by^3}{3}\right]_{-\frac{h}{2}}^{\frac{h}{2}} = \frac{bh(b^2+h^2)}{12}\,. \tag{2.86}$$

Balancing the moments on the segment:

$$\begin{aligned} \mathcal{T}\left(x+dx,t\right) - \mathcal{T}\left(x,t\right) + M(x,t)dx &= \rho I_x \frac{\partial^2\theta}{\partial t^2}\, dx \\ \frac{\partial \mathcal{T}\left(x,t\right)}{\partial x} + M(x,t) &= \rho I_x \frac{\partial^2\theta}{\partial t^2}\,, \end{aligned} \tag{2.87}$$

where the second line is the result of dividing through by dx and taking the limit as $dx \to 0$.

The Saint-Venant torsional rigidity, defined as $GJ = \mathcal{T}l/\theta(l)$, can be rearranged to write an expression for the torque:

$$\mathcal{T} = GJ\frac{\theta(l)}{l} = GJ\frac{\partial\theta}{\partial x}\,, \tag{2.88}$$

where the second equality results by assuming that the rate of twist, $\frac{\partial\theta}{\partial x}$, is constant throughout the beam domain, i.e. $\theta(x) = \left(\frac{\partial\theta}{\partial x}\right)x$. The properties G and J are the shear modulus and torsional constant of the cross section. Substituting this torque expression into Eqn. 2.87,

and assuming that GJ is constant throughout the beam domain, results in the following equation of motion:

$$\rho I_x \frac{\partial^2 \theta}{\partial t^2} - GJ \frac{\partial^2 \theta}{\partial x^2} = M(x,t)\,. \tag{2.89}$$

As in the transverse equation of motion, viscous damping can be added to the model and the spatial coordinate can be normalized with respect to the beam length $\hat{x} = \frac{x}{l}$:

$$\rho I_x \frac{\partial^2 \theta}{\partial t^2} + c_\theta \frac{\partial \theta}{\partial t} - \frac{GJ}{l^2} \frac{\partial^2 \theta}{\partial \hat{x}^2} = M(\hat{x},t)\,. \tag{2.90}$$

2.3.2 Static Solution

In the static case the time derivative terms, $\rho I_x \frac{\partial^2 \theta}{\partial t^2}$ and $c\frac{\partial \theta}{\partial t}$, are zero and the twist can be determined by direct integration:

$$\theta\left(\hat{x}\right) = C_1 \hat{x} + C_2\,, \tag{2.91}$$

where the constants C_1 and C_2 are determined based on the boundary conditions. For a cantilever beam with a tip torque $\mathcal{T}$, these boundary conditions are:

$$\begin{aligned} \theta(0) &= 0 \\ \frac{GJ}{l} \left.\frac{d\theta}{d\hat{x}}\right|_{\hat{x}=1} &= \mathcal{T}\,. \end{aligned} \tag{2.92}$$

Solving for the constants of integration then yields the following static twist equation:

$$\theta\left(\hat{x}\right) = \frac{\mathcal{T} l}{GJ} \hat{x}\,. \tag{2.93}$$

The normalized twist angle and rate are plotted in Fig. 2.11 for a static tip torque, where $\alpha = \theta'(\hat{x})$ is the twist rate.

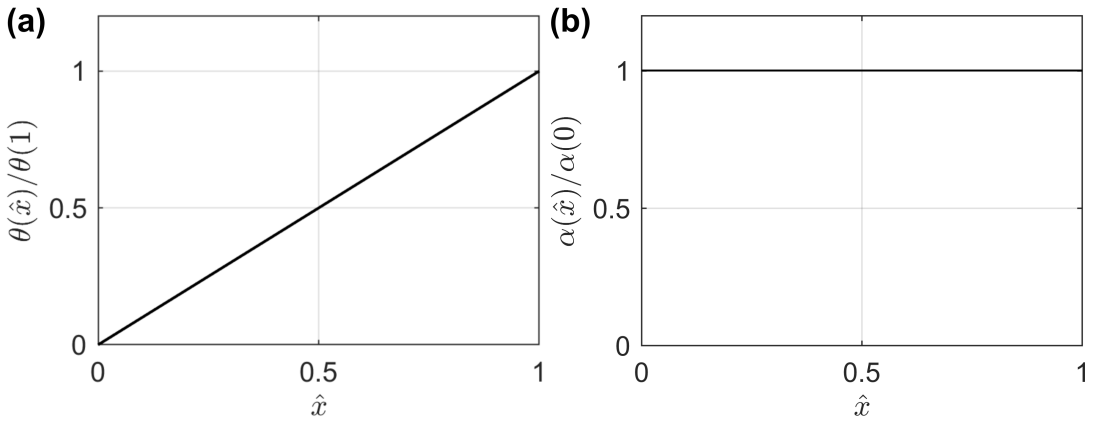

Figure 2.11: Normalized static (a) twist and (b) twist rate shapes of a cantilever beam for a tip torque.

For a beam of rectangular cross section, with dimensions as shown in Fig. 2.12, the torsion constant J is more complex than for a rod of circular cross section.

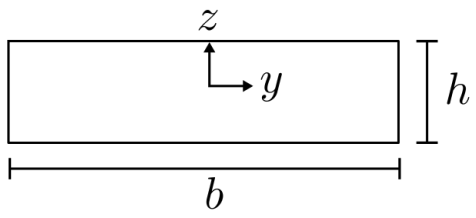

Figure 2.12: Rectangular cross section of beam.

In the case of a vanishingly narrow beam, where the ratio $b/h \to \infty$, the torsion constant is given by $J = bh^3/3$. An approximation for other rectangular cross sections that are not

exceedingly narrow, i.e. where b/h is relatively small, is given by [40]:

$$J = \frac{bh^3}{3}\left[1 - 0.07\frac{h}{b}\left(1 - \frac{h^4}{12b^4}\right)\right] . \tag{2.94}$$

This approximation is based on a Fourier series solution to the exact torsion problem including warping, rather than the approximate problem without warping discussed in this section. In solving the exact problem [41], the torsional constant is found to be:

$$J = \frac{bh^3}{3}\left[1 - \frac{192}{\pi^5}\frac{h}{b}\sum_{i=1,3,5,\ldots}^{\infty}\frac{1}{i^5}\tanh j\pi\frac{b}{2h}\right] . \tag{2.95}$$

Using this second equation, the value of J can be determined to arbitrary numerical accuracy by increasing the number of terms in the infinite series.

2.3.3 Dynamic Solution

The undamped, unforced, form of the beam torsional equation of motion, Eqn. 2.90, can be arranged as:

$$\frac{\partial^2\theta}{\partial t^2} = \frac{GJ}{\rho I_x l^2}\frac{\partial^2\theta}{\partial\hat{x}^2} . \tag{2.96}$$

The boundary conditions corresponding to a cantilever beam are given below, where the beam is clamped at $\hat{x} = 0$ and free at $\hat{x} = 1$:

$$\begin{aligned} \theta(0,t) &= 0 \\ \left.\frac{\partial\theta(\hat{x},t)}{\partial\hat{x}}\right|_{\hat{x}=1} &= 0 . \end{aligned} \tag{2.97}$$

Following the separation of variables method, an assumed solution of the form $\theta(\hat{x},t) =$

$\phi_\theta(\hat{x})\,\eta_\theta(t)$ is substituted into the governing equation:

$$\begin{aligned} \phi_\theta \ddot{\eta}_\theta &= \frac{GJ}{\rho I_x l^2}\phi_\theta'' \eta_\theta \\ \Rightarrow \frac{\ddot{\eta}_\theta}{\eta_\theta} &= \left(\frac{GJ}{\rho I_x l^2}\right)\frac{\phi_\theta''}{\phi_\theta} = -\omega_\theta^2 \,. \end{aligned} \tag{2.98}$$

Since both sides of the second equation are equal, yet functions of different variables, they must be equal to a constant, called here $-\omega_\theta^2$. The boundary conditions given in Eqn. 2.97 can also be rewritten in terms of $\phi_\theta(\hat{x})$:

$$\begin{array}{lllllll} \theta(0,t) & = \phi_\theta(0)\,\eta_\theta(t) & = 0 & \Rightarrow & \phi_\theta(0) & = 0 \\ \left.\frac{\partial\theta(\hat{x},t)}{\partial\hat{x}}\right|_{\hat{x}=1} & = \left.\frac{\partial\phi_\theta(\hat{x})}{\partial\hat{x}}\right|_{\hat{x}=1}\eta_\theta(t) & = 0 & \Rightarrow & \left.\frac{\partial\phi_\theta(\hat{x})}{\partial\hat{x}}\right|_{\hat{x}=1} & = 0\,, \end{array} \tag{2.99}$$

since for all of these cases, $\eta_\theta(t)$ cannot equal zero for all t. Two equations can then be written using Eqn. 2.98:

$$\begin{aligned} \phi_\theta'' + \left(\frac{\rho I_x l^2}{GJ}\right)\omega_\theta^2\phi_\theta &= 0 \\ \ddot{\eta}_\theta + \omega_\theta^2\eta_\theta &= 0\,. \end{aligned} \tag{2.100}$$

Spatial Solution

The characteristic polynomial of the first differential equation is $r^2 + \left(\frac{\rho I_x l^2}{GJ}\right)\omega_\theta^2 = 0$, whose solutions are $r = \pm j\left(\sqrt{\frac{\rho I_x l^2}{GJ}}\omega_\theta\right)$. Thus the solution to this differential equation is [37]:

$$\phi_\theta(\hat{x}) = C_1 \sin\left(\sqrt{\frac{\rho I_x l^2}{GJ}}\omega_\theta\hat{x}\right) + C_2\cos\left(\sqrt{\frac{\rho I_x l^2}{GJ}}\omega_\theta\hat{x}\right)\,, \tag{2.101}$$

where C_1 and C_2 are constants to be determined from the boundary conditions.

Evaluating each of the boundary conditions given in Eqn. 2.99:

1. $\phi_\theta(0) = 0$

$$C_2 = 0 \tag{2.102}$$

2. $\left.\frac{\partial \phi_\theta(\hat{x})}{\partial \hat{x}}\right|_{\hat{x}=1} = 0$

$$C_1 \cos\left(\sqrt{\frac{\rho I_x l^2}{GJ}}\omega_\theta\right) = 0 \tag{2.103}$$

Since $C_1 = 0$ would lead to a trivial solution $\phi_\theta(\hat{x}) = 0$, this indicates that $\cos\left(\sqrt{\frac{\rho I_x l^2}{GJ}}\omega_\theta\right) = 0$, or:

$$\begin{aligned}\left(\sqrt{\frac{\rho I_x l^2}{GJ}}\omega_{\theta,r}\right) &= \frac{(2r-1)\,\pi}{2} \\ \Rightarrow \omega_{\theta,r} &= \left(\sqrt{\frac{GJ}{\rho I_x l^2}}\right)\left(\frac{(2r-1)\,\pi}{2}\right),\end{aligned} \tag{2.104}$$

for $r = 1, 2, 3, \ldots$.

The constant C_1 is an arbitrary scaling of the eigenfunction ϕ_θ, which can be chosen to normalize the mode shape as desired. Choosing here $C_1 = 1$ yields the mode shapes as given by Eqn. 2.101:

$$\phi_{\theta,r}(\hat{x}) = \sin\left(\frac{(2r-1)\,\pi}{2}\hat{x}\right). \tag{2.105}$$

The first four of these mode shapes are shown in Fig. 2.13 along with their corresponding twist rate shapes. As with the transverse curvature plots, the twist rate plot is included as it is proportional to the shear strain in the beam which can be measured using distributed strain sensors, as will be discussed in Chapter 3.

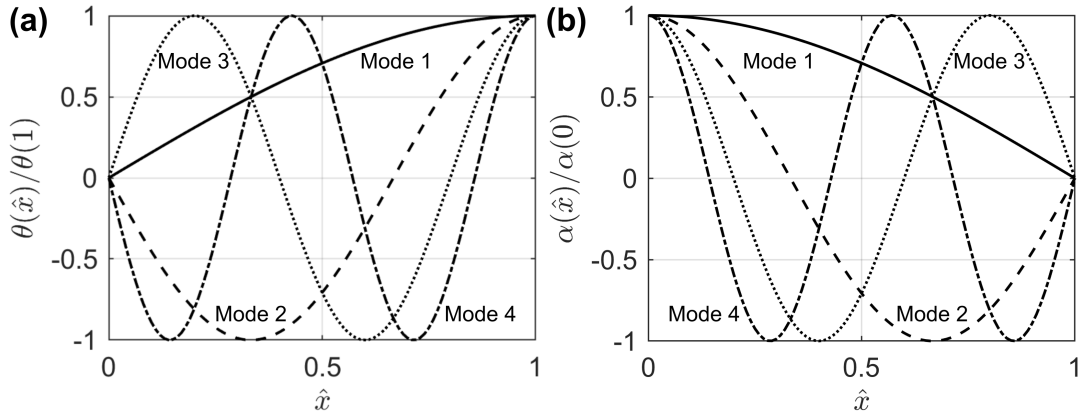

Figure 2.13: Normalized dynamic (a) mode and (b) twist rate shapes of a cantilever beam.

Time Solution

The second differential equation of Eqn. 2.100 has the characteristic polynomial $r^2 + \omega_\theta^2 = 0$, whose solutions are $r = \pm j\omega_\theta$. Thus the solution to this differential equation is a simple harmonic oscillator:

$$\eta_{\theta,r}(t) = a_r \sin \omega_\theta t + b_r \cos \omega_\theta t \,, \tag{2.106}$$

where the coefficients a_r and b_r are constants for each mode determined from the initial conditions.

Total Free Solution

From the above results given in Eqn. 2.105 and Eqn. 2.106, the total solution can be formed as the infinite sum:

$$\theta(\hat{x}, t) = \sum_{r=1}^{\infty} \eta_{\theta,r}(t)\, \phi_{\theta,r}(\hat{x}) \,. \tag{2.107}$$

As with the infinite degree of freedom model for transverse bending, this model can be truncated to N modes by grouping the residual contributions of modes with natural frequencies significantly higher than a particular range of interest.

Forced Solution

Following the same process as for transverse vibration, substituting the total solution given in Eqn. 2.107 into the undamped form of Eqn. 2.90 results in:

$$\begin{aligned}\sum_{r=1}^{\infty}\left[\rho I_x \ddot{\eta}_{\theta,r}\phi_{\theta,r}\left(\hat{x}\right) - \frac{GJ}{l^2}\eta_{\theta,r}\phi''_{\theta,r}(\hat{x})\right] &= M\left(\hat{x},t\right)\\ \rho I_x \sum_{r=1}^{\infty}\left(\ddot{\eta}_{\theta,r} + \omega^2_{\theta,r}\eta_{\theta,r}\right)\phi_{\theta,r}\left(\hat{x}\right) &= M\left(\hat{x},t\right)\ ,\end{aligned} \tag{2.108}$$

where by Eqn. 2.100:

$$\phi''_{\theta} = -\frac{\rho I_x l^2 \omega^2_{\theta}}{GJ}\phi_{\theta}\,. \tag{2.109}$$

Multiplying by an arbitrary mode $\phi_{\theta,s}$, integrating over the beam's domain Ω, and dividing through by ρI_x yields:

$$\ddot{\eta}_{\theta,r} + \omega^2_{\theta,r}\eta_{\theta,r} = \frac{2}{\rho I_x}\int_0^1 M\left(\hat{x},t\right)\phi_{\theta,r}\left(\hat{x}\right)\ d\hat{x}\,, \tag{2.110}$$

where the infinite sum is eliminated by the orthogonality of the mode shapes:

$$\int_{\Omega}\phi_{\theta,s}\phi_{\theta,r}\ d\hat{x} = \begin{cases}\frac{1}{2}, & s = r\\ 0, & s \neq r\,.\end{cases} \tag{2.111}$$

The modal forcing function can then be defined as:

$$M_r\left(t\right) \equiv 2\int_0^1 M\left(\hat{x},t\right)\phi_{\theta,r}\left(\hat{x}\right)\ d\hat{x}\,, \tag{2.112}$$

yielding the following differential equation for the r-th modal coordinate:

$$\ddot{\eta}_{\theta,r} + \omega^2_{\theta,r}\eta_{\theta,r} = \frac{1}{\rho I_x}M_r\left(t\right)\ . \tag{2.113}$$

2.3.4 Single Degree of Freedom Model

The twisting motion of a cantilever beam tip can be represented by an SDOF model, with a system schematic similar to that shown in Fig. A.1, but where the degree of freedom is not translational but rather angular. The equation of motion for the system is:

$$m_{\theta,\text{eff}}\ddot{\theta} + c_\theta\dot{\theta} + k_{\theta,\text{eff}}\theta = \mathcal{T}(t) \ , \tag{2.114}$$

where the effective mass $m_{\theta,\text{eff}}$ (here rotational inertia), damping constant c_θ, and effective stiffness $k_{\theta,\text{eff}}$ of the system must be determined to produce a dynamically equivalent response to the behavior of the beam tip in the distributed parameter model.

The effective tip stiffness, defined as the ratio of the torque acting at the tip to the corresponding angular deflection, is determined by considering the static deflection equation, given in Eqn. 2.93:

$$k_{\theta,\text{eff}} = \frac{\mathcal{T}}{\theta(1)} = \mathcal{T}\cdot\frac{GJ}{\mathcal{T}l} = \frac{GJ}{l} \, . \tag{2.115}$$

Turning now to determining the effective mass, it is assumed here that the twist of the cantilever beam for its first mode of vibration can be approximated by the static deflection curve of Eqn. 2.93. The static deflection equation can be rewritten in terms of the twist at the tip of the beam $\theta(1) = \frac{\mathcal{T}l}{GJ}$, and then differentiated to write an expression for the velocity:

$$\begin{aligned} \theta(\hat{x}) &= \frac{\mathcal{T}L}{GJ}\hat{x} = \theta(1)\hat{x} \\ \Rightarrow \dot{\theta}(\hat{x}) &= \dot{\theta}(1)\hat{x} \, . \end{aligned} \tag{2.116}$$

Substituting this expression into the equation for kinetic energy:

$$T = \frac{1}{2}\int_\Omega \dot{\theta}^2 \, dI_x = \frac{\rho I_x l}{2}\left[\int_0^1 \hat{x}^2 \, d\hat{x}\right]\left(\dot{\theta}(1)\right)^2 = \frac{1}{2}\left[\frac{\rho I_x l}{3}\right]\left(\dot{\theta}(1)\right)^2 \, , \tag{2.117}$$

where $dI_x = \rho I_x \, dx = \rho I_x l \, d\hat{x}$. By analogy with the rotational kinetic energy of an SDOF

system, $T = \frac{1}{2} m_\theta \dot{\theta}^2$, the effective inertia is:

$$m_{\theta,\text{eff}} = \frac{1}{3} \rho I_x l \, . \tag{2.118}$$

Based on these system parameters, the natural frequency of the SDOF system is:

$$\omega_{\theta,n} = \sqrt{\frac{k_{\theta,\text{eff}}}{m_{\theta,\text{eff}}}} = \left(\sqrt{\frac{GJ}{\rho I_x l^2}} \right) \sqrt{3} \, , \tag{2.119}$$

and the equation of motion given in Eqn. 2.114 can also be written in a non-dimensional form as:

$$\ddot{\theta} + 2\zeta \omega_{\theta,n} \dot{\theta} + \omega_{\theta,n}^2 \theta = \frac{1}{m_{\theta,\text{eff}}} \mathcal{T}(t) \, . \tag{2.120}$$

2.3.5 Multiple Degrees of Freedom Model: Bending and Torsion

An assumption underlying the development above is that the transverse bending and twisting degrees of freedom are completely uncoupled. If valid, these models can be taken as the uncoupled equations of motion for an MDOF model:

$$\begin{bmatrix} \frac{33}{140}\rho A l & 0 & 0 \\ 0 & \frac{33}{140}\rho A l & 0 \\ 0 & 0 & \frac{1}{3}\rho I_x l \end{bmatrix} \begin{Bmatrix} \ddot{w} \\ \ddot{v} \\ \ddot{\theta} \end{Bmatrix} + \begin{bmatrix} c_1 & 0 & 0 \\ 0 & c_2 & 0 \\ 0 & 0 & c_\theta \end{bmatrix} \begin{Bmatrix} \dot{w} \\ \dot{v} \\ \dot{\theta} \end{Bmatrix} + \begin{bmatrix} \frac{3EI_y}{l^3} & 0 & 0 \\ 0 & \frac{3EI_z}{l^3} & 0 \\ 0 & 0 & \frac{GJ}{l} \end{bmatrix} \begin{Bmatrix} w \\ v \\ \theta \end{Bmatrix} = \begin{Bmatrix} F_z \\ F_y \\ \mathcal{T} \end{Bmatrix} , \tag{2.121}$$

where the degrees of freedom describe the uncoupled bending and twisting motions of the beam. Note that an additional bending degree of freedom, v, has been added to describe deflection in the y-direction in addition to w for deflection in the z-direction. This additional degree of freedom will be used in Chapter 3 in comparison to its associated bending mode predicted through finite element (FE) analysis.

2.3.6 Orthogonality of Mode Shapes

As for the transverse mode shapes, here it is shown that the torsional mode shapes form an orthogonal set. The process is to show: (1) if $s \neq r$, then $\int_\Omega \phi_{\theta,s}\phi_{\theta,s}\ d\hat{x} = 0$ and (2) $\int_\Omega \phi_{\theta,s}^2\ d\hat{x} = \frac{1}{2}$ for the chosen scaling.

1. $\int_\Omega \phi_{\theta,s}\phi_{\theta,s}\ d\hat{x} = 0$ for $s \neq r$

   This result is shown in the same manner as for the transverse mode shapes. Consider the spatial governing differential equation given in Eqn. 2.100, which states that all modes must satisfy $\phi''_{\theta,r} = -\left(\frac{\rho I_x l^2}{GJ}\right)\omega_{\theta,r}^2\phi_{\theta,r}$ when the derivative is taken with respect to the non-dimensional length coordinate $\hat{x}$. The integral of $\left(\frac{\rho I_x l^2}{GJ}\right)\omega_{\theta,r}^2\int_\Omega \phi_{\theta,s}\phi_{\theta,r}\ d\hat{x}$ can then be written as:

$$\left(\frac{\rho I_x l^2}{GJ}\right)\omega_{\theta,r}^2\int_\Omega \phi_{\theta,s}\phi_{\theta,r}\ d\hat{x} = -\int_\Omega \phi_{\theta,s}\phi''_{\theta,r}\ d\hat{x}\,. \tag{2.122}$$

   Integrating by parts the right hand side of the above equation two times results in:

$$\left(\frac{\rho I_x l^2}{GJ}\right)\omega_{\theta,r}^2\int_\Omega \phi_{\theta,s}\phi_{\theta,r}\ d\hat{x} = \left[-\phi_{\theta,s}\phi'_{\theta,s} + \phi'_{\theta,s}\phi_{\theta,r}\right]_0^1 + \left(\frac{\rho I_x l^2}{GJ}\right)\omega_{\theta,s}^2\int_\Omega \phi_{\theta,s}\phi_{\theta,r}\ d\hat{x}\,, \tag{2.123}$$

   where $\phi''_{\theta,s} = -\left(\frac{\rho I l^2}{GJ}\right)\omega_{\theta,s}^2\phi_{\theta,s}$ has been substituted. Each of the terms in the square brackets can be eliminated due to the boundary conditions of the cantilever beam, which state that $\phi_{\theta,i} = 0$ at $\hat{x} = 0$ and that $\phi'_{\theta,i} = 0$ at $\hat{x} = 1$. Upon rearrangement, Eqn. 2.123 can be written:

$$\left(\omega_{\theta,r}^2 - \omega_{\theta,s}^2\right)\int_\Omega \phi_{\theta,s}\phi_{\theta,r}\ d\hat{x} = 0\,. \tag{2.124}$$

   Since $\omega_{\theta,s} \neq \omega_{\theta,r}$ when $s \neq r$, this equality is true if and only if $\int_\Omega \phi_{\theta,s}\phi_{\theta,r}\ d\hat{x} = 0$.

2. $\int_\Omega \phi_{\theta,s}^2\ d\hat{x} = \frac{1}{2}$

This integral can be directly evaluated using one of the trigonometric integrals stated for the case of transverse bending:

$$\int_{\Omega} \sin^2 \xi_s \hat{x} \; d\hat{x} = \frac{1}{2} - \frac{\sin \xi_s \cos \xi_s}{2\xi_s} \,. \tag{2.125}$$

The desired relationship is then:

$$\int_{\Omega} \phi_{\theta,s}^2 \; d\hat{x} = \int_{\Omega} \sin^2 \left(\frac{(2s-1)\pi}{2} \hat{x} \right) \; d\hat{x} = \frac{1}{2} - \frac{\sin\left(\frac{(2s-1)\pi}{2}\right) \cos\left(\frac{(2s-1)\pi}{2}\right)}{2\left(\frac{(2s-1)\pi}{2}\hat{x}\right)} = \frac{1}{2} \,, \tag{2.126}$$

since $\cos\left(\frac{(2s-1)\pi}{2}\right) = 0$ for all s.

2.3.7 Comparison of Models

The first natural frequency for torsion in a cantilever beam is predicted by Eqn. 2.104 for the distributed parameter model and by Eqn. 2.119 for the SDOF lumped parameter model. The ratio of these predictions is:

$$\frac{\omega_{\theta,n,\text{sdof}}}{\omega_{\theta,n,\text{dist.}}} = \left(\sqrt{\frac{GJ}{\rho I_x l^2}} \right) \sqrt{3} \cdot \left(\sqrt{\frac{\rho I_x l^2}{GJ}} \right) \left(\frac{2}{\pi} \right) = \frac{2\sqrt{3}}{\pi} \approx 1.1027 \,. \tag{2.127}$$

Based on this result, the SDOF model over predicts the natural frequency by approximately 10% in comparison to the distributed parameter model. This over prediction is again the result of additional stiffness introduced in the SDOF model by assuming the static deflection as the mode of vibration.

2.4 Vibration of a Cantilever Plate

In comparison to the cantilever beam, the partial differential equation describing the motion of the cantilever plate does not yield as easily to direct analysis. Instead, in this section the approximate Rayleigh-Ritz method is invoked to predict natural frequencies based on a set of

assumed mode shapes. This section begins with a derivation of the cantilever plate equation of motion and then proceeds to introduce the Rayleigh-Ritz method and a reduced order MDOF model for the plate. Due to the nature of the equation of motion, no comparisons are made between the approximate methods as they are largely numerical and dependent on the specific dimensions and properties of the plate. These comparisons will be given in Chapter 3 for the specific structure to be tested.

2.4.1 Distributed Parameter Model

As with the beam, several assumptions are utilized in the derivation and analysis of the plate: (1) the plate's thickness is much smaller than its length and width, (2) the plate's deflection is small, (3) the plate's mid-plane does not stretch, (4) cross sections of the plate are rigid and remain to normal to the plate's mid-plane, and (5) rotational inertia and transverse shear are negligible. The plate's deflection is assumed to be a function only of the x- and y-coordinates and time, so its motion is assumed to be fully described by the deformation of the mid-plane shown in gray in Fig. 2.14.

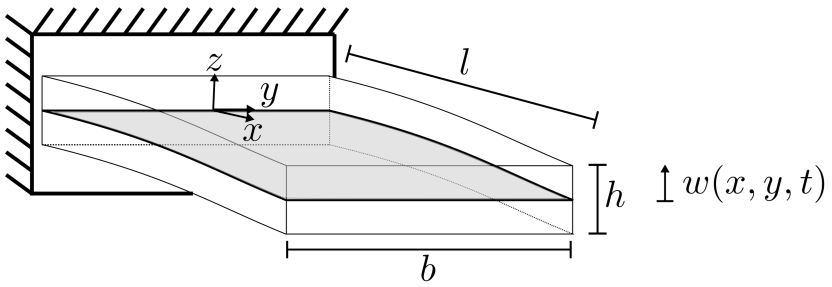

Figure 2.14: Schematic of a cantilever plate.

The bending deformation of the mid-plane surface can be described analogously to the

beam centerline deflection with the displacement components[1]:

$$\begin{aligned} u &= -z\partial_x w \\ v &= -z\partial_y w\,. \end{aligned} \tag{2.128}$$

These displacements, which result from bending about the x- and y-axes, can be seen by referring to the kinematics of bending as shown in Fig. 2.15 for the u displacement [35]. The rotation due to bending of the rigid planes initially in the z-direction and normal to the mid-plane surface can be seen in this figure as point P rotates to point P'. The corresponding relationship for the v component of the displacement field can similarly be shown by replacing all x's with y's in the figure.

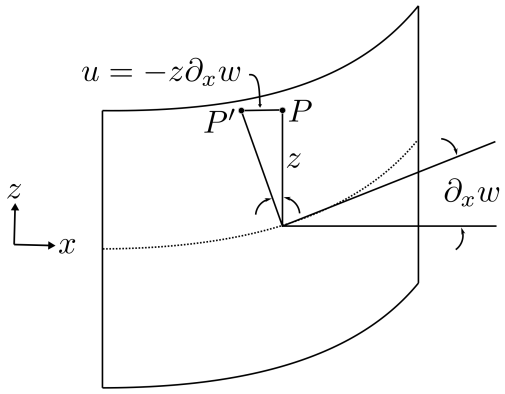

Figure 2.15: Deformation in x-direction due to bending for a plate segment.

[1] Due to the increased presence of partial differentiation with respect to different coordinate directions in this section, a compact notation for vector fields, tensors, and partial differentiation will be employed. Components of a vector field or tensor will be denoted with subscripts, e.g. τ_{xy} indicates the xy cross term of the stress tensor. In addition, partial differentiation with respect to a variable, for example x, will be shortened as $\frac{\partial}{\partial x}(\cdot) = \partial_x$

From this displacement field, the strain field can be written:

$$\begin{aligned} \varepsilon_{xx} &= u_x = -z\partial_{xx}w \\ \varepsilon_{yy} &= v_y = -z\partial_{yy}w \\ \varepsilon_{xy} &= \frac{1}{2}\left(\partial_y u + \partial_x v\right) = -z\partial_{xy}w\,. \end{aligned} \tag{2.129}$$

Hooke's Law states that $\varepsilon_{ij} = \frac{1}{E}\left[\left(1+\nu\right)\tau_{ij} - \nu\tau_{kk}\delta_{ij}\right]$, where ν is Poisson's ratio and δ_{ij} is the Kronecker delta, so these strain components can also be written in terms of the stress components τ_{ij}:

$$\begin{aligned} \varepsilon_{xx} &= \frac{1}{E}\left[\tau_{xx} - \nu\tau_{yy}\right] = -z\partial_{xx}w \\ \varepsilon_{yy} &= \frac{1}{E}\left[\tau_{yy} - \nu\tau_{xx}\right] = -z\partial_{yy}w \\ \varepsilon_{xy} &= \frac{1+\nu}{E}\tau_{xy} = -z\partial_{xy}w\,, \end{aligned} \tag{2.130}$$

where plane stress in the z-plane ($\tau_{xz} = \tau_{yz} = \tau_{zz} = 0$) has been assumed. The solution to the first two equations is:

$$\begin{aligned} \tau_{xx} &= -\frac{Ez}{1-\nu^2}\left(\partial_{xx}w + \nu\partial_{yy}w\right) \\ \tau_{yy} &= -\frac{Ez}{1-\nu^2}\left(\partial_{yy}w + \nu\partial_{xx}w\right)\,, \end{aligned} \tag{2.131}$$

while the rearranged form of the third is:

$$\tau_{xy} = -\frac{Ez}{1+\nu}\partial_{xy}w\,. \tag{2.132}$$

These relationships for the stress can now be used to write expressions for the resultant

moments M in the cross section of the plate element:

$$\begin{aligned} M_x &= -\int_{-\frac{h}{2}}^{\frac{h}{2}} \tau_{xx} \cdot z \; dz = \tfrac{Eh^3}{12(1-\nu^2)} \left(\partial_{xx} w + \nu \partial_{yy} w\right) &&= D\left(\partial_{xx} w + \nu \partial_{yy} w\right) \\ M_y &= -\int_{-\frac{h}{2}}^{\frac{h}{2}} \tau_{yy} \cdot z \; dz = \tfrac{Eh^3}{12(1-\nu^2)} \left(\partial_{yy} w + \nu \partial_{xx} w\right) &&= D\left(\partial_{yy} w + \nu \partial_{xx} w\right) \\ M_{xy} &= -\int_{-\frac{h}{2}}^{\frac{h}{2}} \tau_{xy} \cdot z \; dz = \tfrac{Eh^3}{12(1+\nu)} \partial_{xy} w &&= (1-\nu) D \partial_{xy} w \,, \end{aligned} \tag{2.133}$$

where $D \equiv \frac{Eh^3}{12(1+\nu)}$ is known as the flexural rigidity of the plate. The moment M_x is the bending moment about the y-axis due to the stress distribution τ_{xx} on a face with normal parallel to the x-axis, the moment M_y is the bending moment about the x-axis due to the stress distribution τ_{yy} on a face with normal parallel to the y-axis, and the moment M_{xy} is the twisting moment about the x-axis due to the shear stress distribution τ_{xy} on a face with normal parallel to the x-axis.

Now consider a representative plate element, shown in Fig. 2.16, where only the shear $\mathcal{V}_x$ and moments acting on the faces with normals parallel to the x-axis are represented.

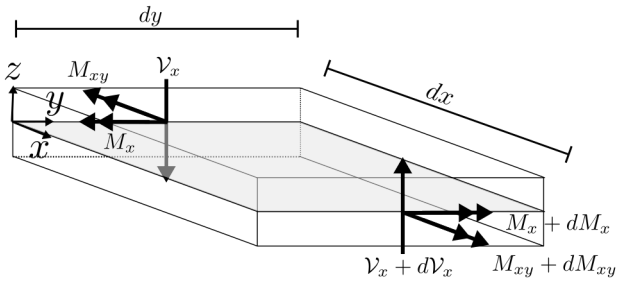

Figure 2.16: Equilibrium on two faces of a plate element.

Corresponding forces and moments, not represented in the figure for clarity, also act on the two faces with normals parallel to the y-direction. A distributed external force $f(x, y, t)$, also acts in the z-direction on the face with normal in the z-direction.

The segment has a total mass of $\rho h\ dx\ dy$. Following the Newton/Euler method, force balance on the plate element in the z-direction results in [41]:

$$\begin{aligned}\left(\mathcal{V}_x + \partial_x \mathcal{V}_x dx - \mathcal{V}_x\right) dy + \left(\mathcal{V}_y + \partial_y \mathcal{V}_y dy - \mathcal{V}_y\right) dx + f\ dx\ dy &= \rho h\ dx\ dy\ \partial_{tt} w \\ \partial_x \mathcal{V}_x + \partial_y \mathcal{V}_y + f &= \rho h \partial_{tt} w\,.\end{aligned} \tag{2.134}$$

The sum of moments about the x-axis is:

$$\begin{aligned}\left(M_{xy} + \partial_x M_{xy} dx - M_{xy}\right) dy + \left(M_y + \partial_y M_y dy - M_y\right) dx & \\ + \left(\mathcal{V}_y + \partial_y \mathcal{V}_y dy\right) dx\ dy + f\ dx\ dy \frac{dy}{2} &= 0 \\ \mathcal{V}_y + \partial_y M_y + \partial_x M_{xy} &= 0\,,\end{aligned} \tag{2.135}$$

where the second line is a result of dividing through by $dx\ dy$ and taking the limit as both differentials approach zero. Following in a similar manner, the sum of moments about the y-axis results in:

$$\mathcal{V}_x + \partial_x M_x + \partial_y M_{xy} = 0\,. \tag{2.136}$$

Taking the derivative of Eqn. 2.135 with respect to y and Eqn. 2.136 with respect to x:

$$\begin{aligned}\partial_y \mathcal{V}_y + \partial_{yy} M_y + \partial_{xy} M_{xy} &= 0 \\ \partial_x \mathcal{V}_x + \partial_{xx} M_x + \partial_{xy} M_{xy} &= 0\,,\end{aligned} \tag{2.137}$$

which can now be substituted into Eqn. 2.134:

$$\rho h \partial_{tt} w + \partial_{yy} M_y + \partial_{xy} M_{xy} + \partial_{xx} M_x + \partial_{xy} M_{xy} = f\,. \tag{2.138}$$

Now substituting the results of Eqn. 2.133 yields the plate equation of motion:

$$\begin{aligned}\rho h \partial_{tt} w + D\left(\partial_{xxxx} w + 2\partial_{xxyy} w + \partial_{yyyy} w\right) &= f \\ \rho h \frac{\partial^2 w\left(x, y, t\right)}{\partial t^2} + D\nabla^4 w\left(x, y, t\right) &= f\left(x, y, t\right)\,,\end{aligned} \tag{2.139}$$

where $\nabla^4(\cdot) = (\partial_{xxxx} + 2\partial_{xxyy} + \partial_{yyyy})(\cdot)$ is the biharmonic operator.

As with the beam, this equation of motion and associated boundary conditions can be derived using the energy approach. Here, the boundary conditions resulting from that method will simply be stated for a rectangular beam oriented with sides parallel to the x- and y-axes:

$$\begin{aligned} M_x\ \delta(\partial_x w) &= 0 \\ M_y\ \delta(\partial_y w) &= 0 \\ (\mathcal{V}_x + \partial_y M_{xy})\,\delta w &= 0 \\ (\mathcal{V}_y + \partial_x M_{xy})\,\delta w &= 0\,. \end{aligned} \tag{2.140}$$

These state that for the sides with normals parallel to the x-axis: (1) either the moment is zero or the slope is prescribed and (2) either the "effective" shear force is zero or the deflection is prescribed. The same holds for the sides with normals parallel to the y-axis. The only difference between these boundary conditions and those for the beam is in the distinction between the shear force and the "effective" shear force. As described in [35], the terms $\mathcal{V}_x + \partial_y M_{xy}$ and $\mathcal{V}_y + \partial_x M_{xy}$ can be interpreted as effective shear forces acting on an element which is "far away" from the corner of the plate. The important takeaway is that the boundary conditions for a beam and plate are somewhat similar in form and can be interpreted in a similar manner, but whose differences are sufficient to make analysis difficult when a free edge is present.

2.4.2 Approximate Solution: Cylindrical Bending

For a static plate, the time derivative term $\rho h \frac{\partial^2 w(x,y,t)}{\partial t^2}$ is zero, and the equation of motion is given by:

$$D\nabla^4 w(x,y,t) = f(x,y)\,. \tag{2.141}$$

If it is assumed that the only nonzero component after applying the biharmonic operator to w is ∂_{xxxx}, then the plate is said to undergo cylindrical bending (i.e. bending about only one axis). Under this assumption, the governing equation can be written:

$$D\partial_{xxxx}w\left(x,t\right)=f(x)\,, \tag{2.142}$$

where the y dependence of both the mid-plane deflection and force has been removed by assumption. The boundary conditions for the cantilever rectangular plate with distributed tip load f, using Eqn. 2.140, are:

$$\begin{aligned} w(0)&=0 \qquad & \partial_x w\Big|_{x=0}&=0 \\ M_x(l)&=0 \qquad & \mathcal{V}_x(l)+\partial_y M_{xy}(l)-f&=0\,. \end{aligned} \tag{2.143}$$

By the definition of M_x in Eqn. 2.133, the first boundary condition in the second line is:

$$M_x(l)=D\left(\partial_{xx}w\Big|_{x=l}+\nu\partial_{yy}w\Big|_{x=l}\right)=0\Rightarrow\partial_{xx}w\Big|_{x=l}=0\,, \tag{2.144}$$

since under cylindrical bending, the curvature in the y-direction is necessarily zero ($\partial_{yy}w=0$). The "effective shear" boundary condition in Eqn. 2.143 is, by Eqn. 2.136:

$$\begin{aligned} \mathcal{V}_x(l)+\partial_y M_{xy}(l)-f&=-\partial_x M_x(l)-f=0 \\ \Rightarrow\partial_{xxx}w\Big|_{x=l}&=-\frac{f}{D}\,. \end{aligned} \tag{2.145}$$

Thus the boundary conditions for cylindrical bending can be written:

$$\begin{aligned} w(0)&=0 \qquad & \partial_x w\Big|_{x=0}&=0 \\ \partial_{xx}w\Big|_{x=l}&=0 \qquad & \partial_{xxx}w\Big|_{x=l}&=-\tfrac{f}{D}\,, \end{aligned} \tag{2.146}$$

which are the same as those for a cantilever beam when the flexural rigidity of the beam, EI_y, is replaced with the flexural rigidity of the plate, D. Using the beam result, the mid-plane

deflection can be written:

$$w\left(\hat{x}\right) = \frac{fl^3}{6D}\hat{x}^2\left(3-\hat{x}\right) . \tag{2.147}$$

It should be noted that f here is given as a distributed tip load with units force per unit length. The total tip load for calculation of the effective stiffness below is thus $F = fb$.

As a result of the similarities between beam and cylindrical plate bending, the following lumped parameter results are easily shown by comparison with those in Section 2.2:

$$\begin{aligned} k_{\text{eff}} &= \frac{F}{w(1)} = fb \cdot \frac{3D}{fl^3} = \frac{3Db}{l^3} \\ m_{\text{eff}} &= \frac{33}{140}\rho bhl \\ \omega_n &= \left(\sqrt{\frac{D}{\rho hl^4}}\right)\sqrt{\frac{420}{33}} . \end{aligned} \tag{2.148}$$

Alternatively, the distributed parameter model can be used directly under the assumption of cylindrical bending. The free vibration form of the plate equation of motion is given by:

$$\partial_{tt}w(\hat{x},t) + \frac{D}{\rho hl^4}\partial_{\hat{x}\hat{x}\hat{x}\hat{x}}w(\hat{x},t) = 0 , \tag{2.149}$$

where the dependence of w on y has been removed by assumption, and as before differentiation with respect to the spatial coordinate x can be written in terms of the non-dimensional coordinate $\hat{x}$ as $\partial_x = \frac{1}{l}\partial_{\hat{x}}$. By direct comparison with the dynamic beam governing equation and solution, the natural frequencies for the cylindrically bending plate are:

$$\omega_r = \left(\sqrt{\frac{D}{\rho hl^4}}\right)\xi_r^2 , \tag{2.150}$$

where ξ_r is defined by the characteristic equation for the beam transverse vibration and the mode shapes are the same as those for the transverse beam for all y-values in the plate domain. While this approximation can serve as a prediction for the natural frequencies of the bending modes of a cantilever plate, the natural frequencies will necessarily be larger than

those of the real system through the artificial stiffness added by assuming bending about only one axis.

2.4.3 Approximate Solution: Torsion

As in the case of the beam in Section 2.2, the torsional modes of vibration can be approximated using the theory of Saint-Venant to develop distributed and SDOF models. Since these approximations are exactly the same for the plate and beam, the key results for the natural frequency predictions are simply summarized here for the distributed parameter model:

$$\omega_{\theta,r} = \left(\sqrt{\frac{GJ}{\rho I_x l^2}}\right)\left(\frac{(2r-1)\,\pi}{2}\right)\,, \tag{2.151}$$

and for the SDOF model:

$$\omega_{\theta,n} = \left(\sqrt{\frac{GJ}{\rho I_x l^2}}\right)\sqrt{3}\,, \tag{2.152}$$

where for a rectangular cross section, the torsion constant can be approximated using one of Eqns. 2.94 or 2.95. These models do not take into account warping in the x-direction due to the non-circular cross section of the plate; thus, they are stiff approximations of the plate's dynamics.

2.4.4 Approximate Solution: Rayleigh-Ritz Method

Following the approximate method described and utilized extensively by others [35, 42, 43, 44, 45], the Rayleigh-Ritz method can be used to determine an upper bound of the natural frequencies for plate structures utilizing candidate functions to describe the mode shapes. For rectangular plates, one of the more useful sets of candidate functions are those composed of products of the beam functions corresponding to the boundary conditions at opposite sides of the plate. The total plate response is then given by the summation of these beam products:

$$w(\hat{x},\hat{y}) = \sum_r \sum_s C_{rs}\phi_r(\hat{x})\chi_s(\hat{y})\,, \tag{2.153}$$

where ϕ_r and χ_s are the beam mode shapes corresponding to the boundary conditions in the $\hat{x}$- and $\hat{y}$-directions, and C_{rs} are coefficients describing the contribution of each candidate mode shape to the total response. For a given number n of beam mode shapes in each of the coordinate directions, the Rayleigh-Ritz method can be used to yield estimated eigenvalues for the n^2 modes of the plate which are approximated by corresponding products of those beam functions. The square root of these eigenvalues, or frequency parameters, can then be used to estimate the natural frequencies of the plate using the equation, $\omega_i = \left(\sqrt{\frac{D}{\rho h l^4}}\right) \lambda_i$, where λ_i are the frequency parameters.

For a cantilever plate, the first beam mode shape is that of the clamped-free beam:

$$\phi_r(\hat{x}) = \cos\xi_r\hat{x} - \cosh\xi_r\hat{x} - \left(\frac{\cos\xi_r + \cosh\xi_r}{\sin\xi_r + \sinh\xi_r}\right)(\sin\xi_r\hat{x} - \sinh\xi_r\hat{x}) \ . \tag{2.154}$$

The second mode shape, denoted $\chi_s(\hat{y})$, is given by the modes of a free-free beam.

Free-free Beam Vibration

Based on the solution to the beam eigenfunction, given in Eqn. 2.42, the free-free beam mode is:

$$\chi_s(\hat{y}) = C_1\sin\beta_s\hat{y} + C_2\cos\beta_s\hat{y} + C_3\sinh\beta_s\hat{y} + C_4\cosh\beta_s\hat{y}\,, \tag{2.155}$$

where the constants C_1, C_2, C_3, and C_4 are determined to satisfy the free-free boundary conditions, which state that the shear and moment equal zero at each end of the beam. The free-free weighted frequencies are denoted β instead of ξ to distinguish them from those of the clamped-free beam.

Evaluating each of the boundary conditions:

1. $\partial_{\hat{y}\hat{y}}\chi_s(0) = 0$

$$C_4 = C_2 \tag{2.156}$$

2. $\partial_{\hat{y}\hat{y}\hat{y}}\chi_s(0) = 0$

$$C_3 = C_1 \tag{2.157}$$

The mode shape can then be written:

$$\chi_s(\hat{y}) = C_1\left(\sin\beta_s\hat{y} + \sinh\beta_s\hat{y}\right) + C_2\left(\cos\beta_s\hat{y} + \cosh\beta_s\hat{y}\right) . \tag{2.158}$$

3. $\partial_{\hat{y}\hat{y}}\chi_s(1) = 0$

$$C_2 = -\left(\frac{\sinh\beta_s - \sin\beta_s}{\cosh\beta_s - \cos\beta_s}\right) C_1 \tag{2.159}$$

Substituting this result into the previous expression:

$$\chi_s(\hat{y}) = \sin\beta_s\hat{y} - \sinh\beta_s\hat{y} - \left(\frac{\sinh\beta_s - \sin\beta_s}{\cosh\beta_s - \cos\beta_s}\right)\left(\cos\beta_s\hat{y} + \cosh\beta_s\hat{y}\right) , \tag{2.160}$$

where the arbitrary scaling factor C_1 is chosen to be 1.

4. $\partial_{\hat{y}\hat{y}\hat{y}}\chi_s(1) = 0$

Taking the required derivative:

$$\beta_s^3\left[-\cos\beta_s + \cosh\beta_s - \left(\frac{\sinh\beta_s - \sin\beta_s}{\cosh\beta_s - \cos\beta_s}\right)\left(\sin\beta_s + \sinh\beta_s\right)\right] = 0 . \tag{2.161}$$

Since $\beta_s = 0$ is a trivial solution, the above equation can be rearranged to find the characteristic equation for the free-free beam:

$$\begin{aligned} \left(\cos\beta_s - \cosh\beta_s\right)^2 &= \left(\sinh\beta_s - \sin\beta_s\right)\left(\sin\beta_s + \sinh\beta_s\right) \\ \cos^2\beta_s + \cosh^2\beta_s - 2\cos\beta_s\cosh\beta_s &= -\sin^2\beta_s + \sinh^2\beta_s \\ 1 - \cos\beta_s\cosh\beta_s &= 0 . \end{aligned} \tag{2.162}$$

As with the clamped-free beam, this characteristic equation has infinitely many solu-

tions. The first several of these solutions are:

$$\beta_s = \{4.73004074, 7.85320462, 10.99560784, 14.13716549, 17.27875966\ldots\}\ . \quad (2.163)$$

In addition to these flexible modes, the free-free beam also has two rigid body modes: (1) pure translation, which has a mode shape described by $\chi_1^r(\hat{y}) = 1$, and (2) pure rotation, which has a mode shape described by $\chi_2^r(\hat{y}) = 1 - 2\hat{y}$.

Comment on Boundary Conditions

As will be shown in Chapter 3, using these products of beam functions to describe the mode shapes of a plate yield reasonably accurate models for the mode shapes and natural frequencies of a cantilever plate. It should be noted, however, that mode shapes defined in this manner do not meet the free edge boundary conditions specified for the cantilever plate exactly. To see why, consider the free end opposite the clamped end of the plate. Since the slope and deflection at this end are not specified, the boundary conditions according to Eqns. 2.133, 2.136, and 2.140 must be:

$$\begin{aligned} M_x &= D\left(\partial_{xx}w + \nu\partial_{yy}w\right) = 0 \\ \mathcal{V}_x + \partial_y M_{xy} &= -\partial_x M_x = D(\partial_{xxx}w + \nu\partial_{xyy}w) = 0\,. \end{aligned} \quad (2.164)$$

At the free end, $\partial_{xx}w = \phi''\chi = 0$, since $\phi'' = 0$ from the clamped-free boundary conditions. However, $\partial_{yy}w = \phi\chi'' \neq 0$ except for the rigid body modes of the free-free beam. Thus, the first equation is not satisfied for all beam products. In addition, $\partial_{xxx}w = \phi'''\chi = 0$ for all modes due to the clamped-free boundary condition, but $\partial_{xyy}w = \phi'\chi'' \neq 0$ for any but the rigid body modes of the free-free beam. With that said, the beam products still yield a useful approximation to the eigenfunctions and natural frequencies.

2.4.5 Multiple Degrees of Freedom Models

As described for the cantilever beam, given a set of N orthogonal mode shapes, the total motion of the plate can be described using a summation of N second order systems for the modal coordinates. Ordering the modes given by beam products according to their frequency parameter λ_i determined through the Rayleigh-Ritz procedure, a truncated model of the cantilever plate can then be written as:

$$w(\hat{x},\hat{y}) = \sum_{i=1}^{N} \eta_i(t) W_i(\hat{x},\hat{y})\,, \tag{2.165}$$

where W_i is the i-th beam product mode shape when ordered from least to greatest frequency parameter, and η_i is the modal coordinate for the i-th mode. Modes with natural frequencies far outside the range of interest can be grouped in the residual term yielding a reduced-order model of desired accuracy.

Alternatively, if the bending and torsional modes are assumed to be uncoupled, two other approximate models can be utilized. The SDOF cylindrical bending and torsional modes can be combined to write one set of uncoupled equations of motion:

$$\begin{bmatrix} \frac{33}{140}\rho bhl & 0 \\ 0 & \frac{1}{3}\rho I_x l \end{bmatrix} \begin{Bmatrix} \ddot{w} \\ \ddot{\theta} \end{Bmatrix} + \begin{bmatrix} c & 0 \\ 0 & c_\theta \end{bmatrix} \begin{Bmatrix} \dot{w} \\ \dot{\theta} \end{Bmatrix} + \begin{bmatrix} \frac{3Db}{l^3} & 0 \\ 0 & \frac{GJ}{l} \end{bmatrix} \begin{Bmatrix} w \\ \theta \end{Bmatrix} = \begin{Bmatrix} F_z \\ \mathcal{T} \end{Bmatrix}. \tag{2.166}$$

Another method to model uncoupled bending and torsion of the plate is to use the distributed parameter models of cylindrical bending and torsion. Since comparisons between these approximations and the Rayleigh-Ritz method are only possible after determining the frequency parameters λ_i corresponding to specific plate dimensions and properties, this model comparison will be postponed until Chapter 3 where a particular plate structure is analyzed.

2.5 Summary

In this chapter, the distributed parameter equations of motion for cantilever beams and plates are derived, and exact and approximate solution methods are discussed. Several methods related to model reduction, to include modal truncation and lumped parameter approximations, are introduced, and key results are shown. The results reviewed here will be used in the following chapters to model specific beam and plate structures and compare the predictions of each to experimental results. Several important equations derived in this chapter are summarized in Table 2.1 for cantilever beams and Table 2.2 for cantilever plates.

Table 2.1: Summary of important cantilever beam equations.

	Equation	Description
Transverse Dynamics	$\rho A\frac{\partial^2 w(\hat{x},t)}{\partial t^2}+c\frac{\partial w(\hat{x},t)}{\partial t}+\frac{EI_y}{l^4}\frac{\partial^4 w(\hat{x},t)}{\partial \hat{x}^4}=f(\hat{x},t)$	Equation of Motion
	$w(\hat{x})=\frac{Fl^3}{6EI_y}\hat{x}^2\left(3-\hat{x}\right)$	Static Deflection
	$\varepsilon_{\hat{x}\hat{x}}(\hat{x})=-\frac{h}{2l^2}\cdot\frac{\partial^2 w(\hat{x})}{\partial \hat{x}^2}$	Maximum Bending Strain
	$\phi_r(\hat{x})=\cos\xi_r\hat{x}-\cosh\xi_r\hat{x}$ $-\left(\frac{\cos\xi_r+\cosh\xi_r}{\sin\xi_r+\sinh\xi_r}\right)(\sin\xi_r\hat{x}-\sinh\xi_r\hat{x})$	Mode Shapes
	$1+\cos\xi_r\cosh\xi_r=0$	Characteristic Equation
	$\omega_r=\left(\sqrt{\frac{EI_y}{\rho Al^4}}\right)\xi_r^2$	Natural Frequencies
	$\ddot{\eta}_r+\omega_r^2\eta_r=\frac{1}{\rho A}F_r(t)$	Modal Equation of Motion
	$F_r(t)=\int_0^1 f(\hat{x},t)\phi_r(\hat{x})\,d\hat{x}$	Modal Force
	$k_{\text{eff}}=\frac{3EI_y}{l^3}$	Lumped Stiffness
	$m_{\text{eff}}=\frac{33}{140}\rho Al$	Lumped Mass
Torsional Dynamics	$\rho I_x\frac{\partial^2\theta}{\partial t}+c\frac{\partial\theta}{\partial t}-\frac{GJ}{l^2}\frac{\partial^2\theta}{\partial\hat{x}^2}=M(\hat{x},t)$	Equation of Motion
	$\theta(\hat{x})=\frac{\mathcal{T}l}{GJ}\hat{x}$	Static Twist
	$\phi_{\theta,r}(\hat{x})=\sin\left(\frac{(2r-1)\pi}{2}\hat{x}\right)$	Mode Shapes
	$\omega_{\theta,r}=\left(\sqrt{\frac{GJ}{\rho I_x l^2}}\right)\left(\frac{(2r-1)\pi}{2}\right)$	Natural Frequencies
	$\ddot{\eta}_{\theta,r}+\omega_{\theta,r}^2\eta_{\theta,r}=\frac{1}{\rho I_x}M_r(t)$	Modal Equation of Motion
	$k_{\theta,\text{eff}}=\frac{GJ}{l}$	Lumped Stiffness
	$m_{\theta,\text{eff}}=\frac{1}{3}\rho I_x l$	Lumped Mass

Table 2.2: Summary of important cantilever plate equations.

Equation	Description
$\rho h \dfrac{\partial^2 w(x,y,t)}{\partial t^2} + D\nabla^4 w(x,y,t) = f(x,y,t)$	Equation of Motion
$\omega_r = \left(\sqrt{\dfrac{D}{\rho h l^4}}\right) \xi_r^2$	Cylindrical Bending Natural Frequencies
$k_{\text{eff}} = \dfrac{3Db}{l^3}$	Cylindrical Bending Lumped Stiffness
$m_{\text{eff}} = \dfrac{1}{3}\rho b h l$	Cylindrical Bending Lumped Mass
$w(\hat{x},\hat{y}) = \sum_r \sum_s C_{rs}\phi_r(\hat{x})\chi_s(\hat{x})$	Approximate Plate Response
$\phi_r(\hat{x}) = \cos\xi_r\hat{x} - \cosh\xi_r\hat{x} - \left(\dfrac{\cos\xi_r + \cosh\xi_r}{\sin\xi_r + \sinh\xi_r}\right)(\sin\xi_r\hat{x} - \sinh\xi_r\hat{x})$	Clamped-Free Beam Mode Shape
$1 + \cos\xi_r \cosh\xi_r = 0$	Clamped-Free Characteristic Equation
$\chi_s(\hat{y}) = \sin\beta_s\hat{y} - \sinh\beta_s\hat{y} - \left(\dfrac{\sinh\beta_s - \sin\beta_s}{\cosh\beta_s - \cos\beta_s}\right)(\cos\beta_s\hat{y} + \cosh\beta_s\hat{y})$	Free-Free Beam Mode Shape
$1 - \cos\beta_s \cosh\beta_s = 0$	Free-Free Characteristic Equation

CHAPTER 3
DISTRIBUTED SENSING: FIBER OPTIC STRAIN SENSING

3.1 Introduction

In this chapter, the use of distributed strain sensors for static and dynamic shape identification is considered. In the first section, the operating principles behind fiber optic strain sensing (FOSS) systems are introduced and two types of optical methods to determine strain in a fiber are compared. In the second section, results are presented which utilize distributed strain measurements to determine static deformation and dynamic mode shapes for cantilever beams and plates. Estimation of the system natural frequencies based on the dynamic responses will also be discussed. These results will be compared with analytical and finite element (FE) results to evaluate the accuracy of FOSS in estimating the deformation fields of the tested specimens.

3.2 Theory

Two different methods of using FOSS for distributed sensing are briefly described in this section: Optical Frequency Domain Reflectometry and Wavelength Division Multiplexing. While both methods are based on the same operating principle of a coupled response between the optical and mechanical characteristics of an optical sensor, each has unique characteristics and strengths which indicate the circumstances in which one or the other may be most useful.

Both types of optical interrogators utilize the same type of sensors, which are known as Fiber Bragg Gratings (FBGs). During manufacture, FBGs which interact most strongly with a specified nominal wavelength of light, known as the Bragg wavelength, are etched into the optical fiber. Incident light which encounters an FBG has the highest reflectivity at the Bragg wavelength – wavelengths far from the Bragg wavelength are mostly transmitted through the FBG. The Bragg wavelength for an FBG is given by $\lambda_B = 2n_{\text{eff}}\Lambda$, where n_{eff}

is the effective index of refraction for the fiber material and Λ is the grating period of the FBG.

The usefulness of these sensors is that the Bragg wavelength of an FBG is proportionally related to the axial strain at that sensor. At zero strain, the Bragg wavelength of the FBG is the nominal value. When the axial strain at the sensor changes, its Bragg wavelength changes proportionally by the relationship:

$$\frac{\Delta\lambda_B}{\lambda_B} = (1 - p_e)\,\varepsilon \tag{3.1}$$

where p_e is the photoelastic coefficient for the fiber material and ε is its axial strain. Using this relationship, an interrogator which can track changes in the Bragg wavelength of an FBG can thus calculate the axial strain at that sensor. Changes in temperature also cause changes in the Bragg wavelength, however here the "tare" Bragg wavelength is taken before each experimental measurement and the temperature is assumed to be constant during a single measurement.

3.2.1 Optical Frequency Domain Reflectometry

In the Optical Frequency Domain Reflectometry (OFDR) method, changes in the Bragg wavelength are detected by scanning a tunable laser in a saw-tooth frequency sweep and measuring the interaction between the light reflected by the sensor and that reflected by a coupled broadband reflector. Many FBGs with the same nominal Bragg wavelength can be positioned in series along one optical fiber. Since the reflected spectrum from the sensors overlap, individual sensor changes in Bragg wavelength can only be measured through a digital signal processing (DSP) routine involving two Fast Fourier Transforms (FFTs). Typical raw reflectivity data, as shown in Fig. 3.1(a), represents the power detected from all sensors in a fiber for wavelengths from 1556 to 1573 nm during a frequency sweep. This raw data is FFT'd to bring the wavelength domain data into the spatial domain, yielding the spatial

set, shown in Fig. 3.1(b) for 10 gratings located in a 10 cm section of fiber.

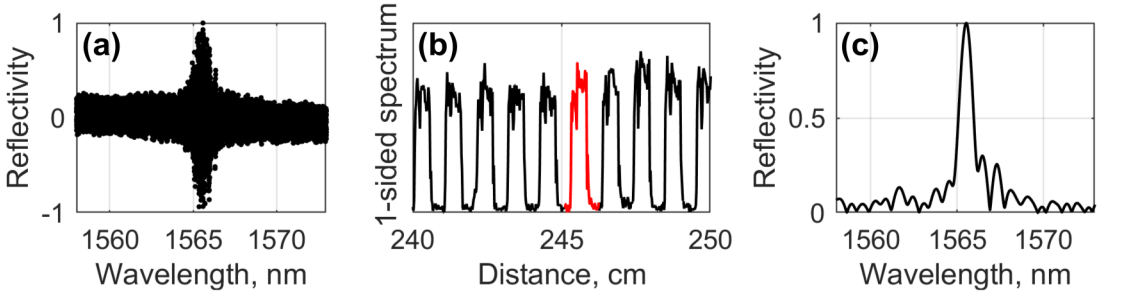

Figure 3.1: Processing of FOSS data for OFDR interrogation systems. (a) Raw reflectivity data. (b) Spatial set. (c) Spectral peak.

The spatial set is notch-filtered to extract the data for each individual FBG, represented by the red response of a single grating in Fig. 3.1(b), which is then inverse FFT'd to return the spatial data to the wavelength domain. A typical plot of an individual sensor's wavelength data is shown in Fig. 3.1(c). Finally, the spectral peak of this wavelength data can be estimated to determine the measured Bragg wavelength for that sensor. This notch-filtering, inverse FFT, and peak detection must occur for each FBG located on the fiber at each measurement. Changes in the detected Bragg wavelength, or peak shifts, for each sensor can then be mapped to corresponding changes in strain by Eqn. 3.1; thus, the axial strain distribution in the fiber can be determined.

3.2.2 Wavelength Division Multiplexing

In an alternate interrogation technique, known as Wavelength Division Multiplexing (WDM), the FBGs on one sensing fiber are manufactured at distinct nominal Bragg wavelengths. Each FBG occupies its own discrete bin in wavelength space, and it is assumed that its measured spectral peak will remain distinct from those of all the other FBGs on the sensing fiber.

During an incident wavelength sweep the contribution of each FBG to the total measured response can thus be determined by directly tracking the movement of individual spectral peaks. The strain for each FBG can then be determined by Eqn. 3.1.

Since the lasers providing incident light have a limited wavelength sweep range, the number of bins, and therefore sensors, which can be accommodated is also limited. For a given bin size, a laser capable of scanning a larger wavelength range can support more sensors; for a given laser, smaller bin sizes increase the number of sensors. The bin size for a given sensor is related to the magnitude of strain that it can measure accurately. For example, if the bin size for the sensor is doubled (i.e. the maximum and minimum $\Delta\lambda_B$ is doubled), the maximum measurable absolute strain, by Eqn. 3.1, also doubles. Depending on the anticipated maximum strain, the bin size of the FBG can be modified.

3.2.3 Interrogation Comparison

OFDR and WDM interrogation systems have different strengths. In OFDR, hundreds of sensors can be etched along a single fiber, yielding high density strain measurements at many locations. Its dynamic measurement characteristics, however, are relatively poor. The current maximum sampling rates for OFDR systems is generally less than 100 Hz, with relatively high measurement latency. WDM interrogators, on the other hand, are able to achieve significantly higher sampling rates, on the order of 1 kHz. The tradeoff, however, is that fewer sensors can be etched on a single fiber, with most systems supporting approximately 40 sensors per fiber.

The decision between which interrogation system to use depends on the test objectives. For static or low frequency tests requiring high spatial strain resolution, an OFDR system would be the best option. For tests requiring real-time dynamic strain measurements, such as in active control applications, the characteristics of WDM systems are superior.

3.2.4 Experimental Hardware

Since the focus in this thesis is on dynamic phenomena, a WDM system is utilized for data acquisition. The interrogator is the Micron Optics si-155, shown in Fig. 3.2, which supports 4 channels of sensing fibers and a sampling rate of 1 kHz.

Figure 3.2: Micron Optics si-155 fiber optic interrogator.

The sensor latency, measured in comparison with a collocated strain gage, is approximately 0.65 ms. Each sensing fiber utilized in this thesis is manufactured by FBGS and is etched with 39 FBGs located 20 mm center-to-center.

The fibers are attached to the beam and plate (discussed later) using a two part aircraft adhesive known as Hysol EA 9394. The surface is first thoroughly cleaned using 200 proof ethanol, and then the fiber is temporarily positioned using Kapton tape. Kapton tape is also used to lay down a masking line on either side of the fiber. A final cleaning of the surface is conducted with the ethanol immediately prior to application of the adhesive. The adhesive is applied in a layer approximately 0.5-1.0 mm thick, and care must be taken to roll the fiber back and forth to ensure the adhesive forms an effective bond between the fiber and the substrate.

3.3 Shape Estimation from Strain Field: Cantilever Beam

In this section, a method to estimate the deformation of a cantilever beam using distributed strain measurements is first described. Next, simulated data from analytical relationships are used to evaluate the accuracy of the shape estimation procedures. Experimental data are then analyzed using the method described to yield static deflection and mode shape estimates to compare with the analytical results.

3.3.1 Strain Integration Method

By Eqn. 2.20, the surface strain for a cantilever beam in bending is given by:

$$\varepsilon_{xx}(\hat{x}) = -\frac{h}{2} \cdot \frac{\partial^2 w(\hat{x})}{\partial x^2} = -\frac{h}{2l^2} \cdot \frac{\partial^2 w(\hat{x})}{\partial \hat{x}^2}, \tag{3.2}$$

where w is the deflection, h is the thickness, and l is the length of the beam (see Fig. 2.1). If the strain field is known, the curvature throughout the beam domain can be directly determined from Eqn. 3.2. Integrating the curvature function twice then yields the cantilever beam's deflection based on zero integration constants at the root. One method to estimate the beam's deflection, then, is to use estimates of the surface strain along the beam's domain to estimate the curvature, and then integrate twice to determine the corresponding deflection.

One such numerical method, known as the Newmark-β method [46], is a single step procedure used in structural dynamics for integration of known accelerations to yield velocities and displacements [47]. It can be applied here to the estimated curvature, computed from the strain field using Eqn. 3.2, to yield slope and deflection estimates at the FOSS strain stations. Using the common parameters of the Newmark method ($\alpha = \frac{1}{2}$ and $\beta = \frac{1}{4}$), which is equivalent to assuming that the curvature is constant between strain stations, the

slope and deflection at station $i+1$ are given by:

$$\begin{aligned} w'_{i+1} &= w'_i + \frac{\Delta x}{2} \cdot \left(w''_i + w''_{i+1}\right) \\ w_{i+1} &= w_i + \Delta x \cdot w'_i + \frac{\Delta x^2}{4} \cdot \left(w''_i + w''_{i+1}\right) \ , \end{aligned} \tag{3.3}$$

where Δx is the distance between strain stations and $'$ indicates differentiation with respect to x. Similar numerical techniques for determining structural deformation based on strain measurements have been used by other researchers [1, 8].

Assuming that the discrete strain measurements either span the domain of the beam or are extrapolated to do so, one way to implement the numerical integration based on Eqn. 3.3 uses matrices as the integrators. For the boundary conditions of the cantilever beam, the first several terms for the slope estimates are:

$$\begin{aligned} w'_0 &= 0 \\ w'_1 &= \frac{\Delta x}{2} \cdot (w''_0 + w''_1) \\ w'_2 &= w'_1 + \frac{\Delta x}{2} \cdot (w''_1 + w''_2) = \frac{\Delta x}{2} \cdot (w''_0 + 2w''_1 + w''_2) \\ w'_3 &= w'_2 + \frac{\Delta x}{2} \cdot (w''_2 + w''_3) = \frac{\Delta x}{2} \cdot (w''_0 + 2w''_1 + 2w''_2 + w''_3) \\ &\vdots . \end{aligned} \tag{3.4}$$

Assuming this pattern is true for the i-th term, the $i+1$ term is:

$$\begin{aligned} w'_{i+1} &= w'_i + \frac{\Delta x}{2} \cdot \left(w''_i + w''_{i+1}\right) \\ &= \frac{\Delta x}{2} \cdot \left(w''_0 + 2\sum_{k=1}^{i-1} w''_k + w''_i\right) + \frac{\Delta x}{2} \cdot \left(w''_i + w''_{i+1}\right) \\ &= \frac{\Delta x}{2} \cdot \left(w''_0 + 2\sum_{k=1}^{i} w''_k + w''_{i+1}\right) \ , \end{aligned} \tag{3.5}$$

thus establishing the general pattern by induction. These equations for the slope estimates

w'_i can be arranged as an $N \times 1$ vector:

$$\begin{Bmatrix} w'_0 \\ w'_1 \\ w'_2 \\ w'_3 \\ \vdots \\ w'_{N-1} \end{Bmatrix} = \frac{\Delta x}{2} \begin{bmatrix} 0 & 0 & 0 & 0 & 0 & \cdots \\ 1 & 1 & 0 & 0 & 0 & \cdots \\ 1 & 2 & 1 & 0 & 0 & \cdots \\ 1 & 2 & 2 & 1 & 0 & \cdots \\ \vdots & & & & \ddots & \\ 1 & 2 & 2 & \cdots & 2 & 1 \end{bmatrix} \begin{Bmatrix} w''_0 \\ w''_1 \\ w''_2 \\ w''_3 \\ \vdots \\ w''_{N-1} \end{Bmatrix} = \boldsymbol{W}\boldsymbol{w}'' \,. \tag{3.6}$$

The matrix $\boldsymbol{W}$ can be interpreted as the "integration matrix" which can be used to determine the slope vector from the curvature vector.

Similarly, the first several terms for the deflection estimates are:

$$\begin{aligned} w_0 &= 0 \\ w_1 &= \frac{\Delta x^2}{4} \cdot (w''_0 + w''_1) = \frac{\Delta x}{2} (w'_0 + w'_1) \\ w_2 &= w_1 + \Delta x \cdot w'_1 + \frac{\Delta x^2}{4} \cdot (w''_1 + w''_2) = \frac{\Delta x}{2} \cdot (w'_0 + 2w'_1 + w'_2) \\ w_3 &= w_2 + \Delta x \cdot w'_2 + \frac{\Delta x^2}{4} \cdot (w''_2 + w''_3) = \frac{\Delta x}{2} \cdot (w'_0 + 2w'_1 + 2w'_2 + w'_3) \\ &\vdots, \end{aligned} \tag{3.7}$$

where the results for the slope estimates have been substituted and w'_0 has been added to the final sums on each row to show that the pattern is the same as for the slope estimates. Since this value is zero by the boundary condition, its addition has no effect on the sums. The validity of the pattern for all terms follows from the same induction argument as before.

These equations for the deflection estimates w_i can then be arranged as:

$$\boldsymbol{w} = \boldsymbol{W}\boldsymbol{w'} = \boldsymbol{W}^2\boldsymbol{w}'' \,, \tag{3.8}$$

where the integration matrix $\boldsymbol{W}$ is applied twice to determine the deflection vector $\boldsymbol{w}$ from

the curvature vector $\boldsymbol{w}''$.

An additional numerical integration strategy is to interpolate the acquired discrete data between the strain stations using a polynomial in order to increase the number of integration points and resulting accuracy. One such scheme uses piecewise cubic polynomials for interpolation. This method, known as a cubic spline, also ensures that the curvature of the spline is continuous throughout the interpolation region. This method has previously been used in various formulations to assess its effectiveness in shape reconstruction [7]. The Newmark numerical integration scheme can then be applied to the interpolated data to determine the beam deflection.

One note on applying this numerical integration strategy that should be emphasized is that the discrete strain measurements must span the domain of the beam, i.e. measurements at the root and tip must be available in order to apply this technique. Practically speaking, neither estimate is easy to make using bonded sensing fibers. Instead, in the experimental cases the discrete strain measurements are always extrapolated using a cubic spline to yield estimates spanning the beam's length.

3.3.2 Shape Estimation from Simulated Strain Data

In the next two sections, simulated strain data based on the analytical static and mode shape curvatures of a cantilever beam are integrated using the methodology described above. The accuracy of these numerical results is then compared to the analytical deflection shapes.

Static Simulation

With the known deflection and strain profiles for a tip loaded cantilever beam, simulated FOSS measurements can be computed from Eqn. 3.2 using the static curvature profile given by Eqn. 2.34 at discrete strain stations along the beam domain. For the simulated data, the curvature/strain is calculated based on an applied tip load of 1 N. These simulated measurements can then be integrated using the schemes described above and compared to

the analytical deflection profile given by Eqn. 2.33.

For the simulation, the beam will have the same material and geometric properties, summarized in Table 3.1, of the specimen to be analyzed experimentally later. The first FBG is located at 20 mm from the root of the beam and each subsequent FBG is located 20 mm farther down the fiber. This arrangement is based on the bonding scheme of the bench top cantilever beam specimen, which is instrumented with a WDM fiber with FBGs 20 mm on center.

Table 3.1: Material properties of the beam specimen.

Parameter	Variable	Value
Material		Aluminum 6061
Mass, Total	m	157 g
Density	ρ	2640 kg/m^3
Elastic modulus	E	68.9 GPa [48]
Poisson's ratio	ν	0.35 [48]
Length, Total		488 mm
Length, Free	l	450 mm
Width	b	38.1 mm
Height	h	3.20 mm

Two cases are compared here: one without interpolation and the second with a cubic spline. The cubic spline used for the second case interpolates the simulated strain measurements every 5 mm, corresponding to a quadroupling of the integrated strain measurements in comparison to the simulated data. As previously noted, the root and tip measurements must be extrapolated in the implementation of this integration scheme. For the interpolation case, the same 5 mm spacing is used in the extrapolation regions from the root to the first sensor and from the last sensor to the tip. In the integration case without interpolation,

only the root and tip measurements are extrapolated.

The integrated deflection profiles using the simulated data is shown in comparison to the analytical deflection in Fig. 3.3 for exclusive Newmark integration and Newmark integration of the cubic spline. Qualitatively, integration after the cubic spline leads to a result that is almost identical to the analytical result (an error of only 0.003% at the tip) while the exclusive Newmark integration of the simulation strain is significantly farther from the analytical (an error of more than 3% at the tip).

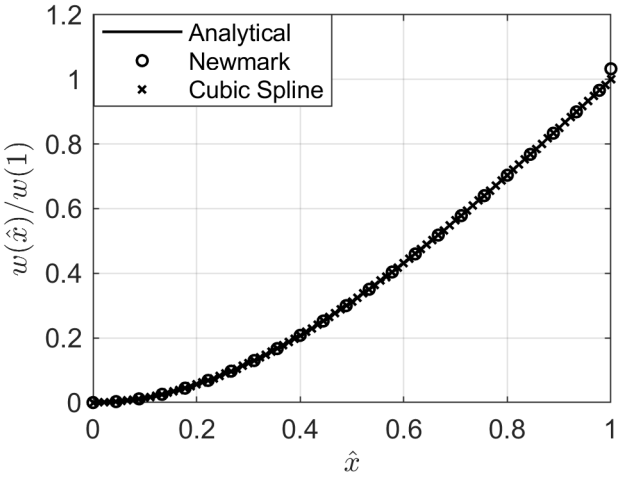

Figure 3.3: Estimated static deflection of the cantilever beam for a point tip load based on different integration algorithms of simulated FOSS strain data.

Mode Shapes Simulation

The same integration methods described for the static cases can also be applied for dynamic mode shape identification. Here, simulated FOSS strain data is computed as previously described using Eqn. 3.2 with the mode shapes given by Eqn. 2.53 to compute the strain for the first four modes. The same Newmark integration scheme with and without cubic spline interpolation is then conducted and the results compared to the analytical mode shapes in

Fig. 3.4.

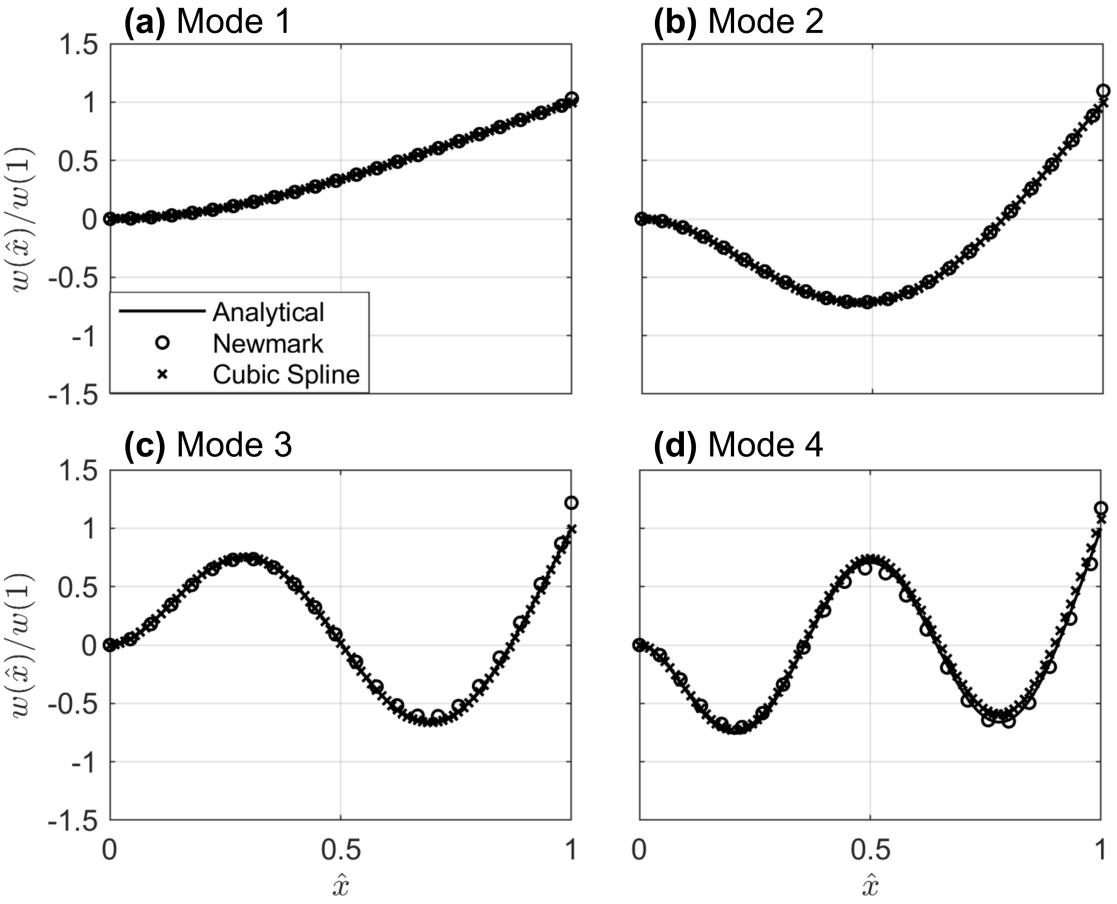

Figure 3.4: Estimated mode shapes of the cantilever beam based on different integration algorithms of simulated FOSS strain data.

To compare the results of these integration schemes with the analytical mode shapes, the maximum relative errors in shape for both integration methods, which occur at the beam tip, are reported in Table 3.2.

Table 3.2: Mode shape tip deflection error for different integration algorithms of simulated FOSS strain data.

Method	Mode 1	Mode 2	Mode 3	Mode 4
Newmark	3.0%	9.6%	21.8%	17.2%
Cubic Spline plus Newmark	0.002%	0.002%	0.9%	7.8%

As for the static integration of simulated strain data, interpolating the discrete strain measurements before integration yields results that are significantly more accurate than exclusive integration of the simulated strain measurements. Based on these results, cubic spline interpolation will be implemented for static and dynamic shape estimation in the experimental section.

3.3.3 Shape Estimation from Experimental Strain Data

Following the development based on simulated strain data in the previous two sections, the integration scheme is implemented in this section for experimental data. The estimated tip displacement is then compared with experimental measurements for the static cases, and the estimated mode shapes are compared with the analytical beam results of Chapter 2.

Static Testing

Validation of the static shape estimation process using distributed strain measurements is conducted here on a cantilever beam. A schematic and image of the test setup are given in Fig. 3.5, and the material and geometric properties are the same as those given in Table 3.1 for the simulation.

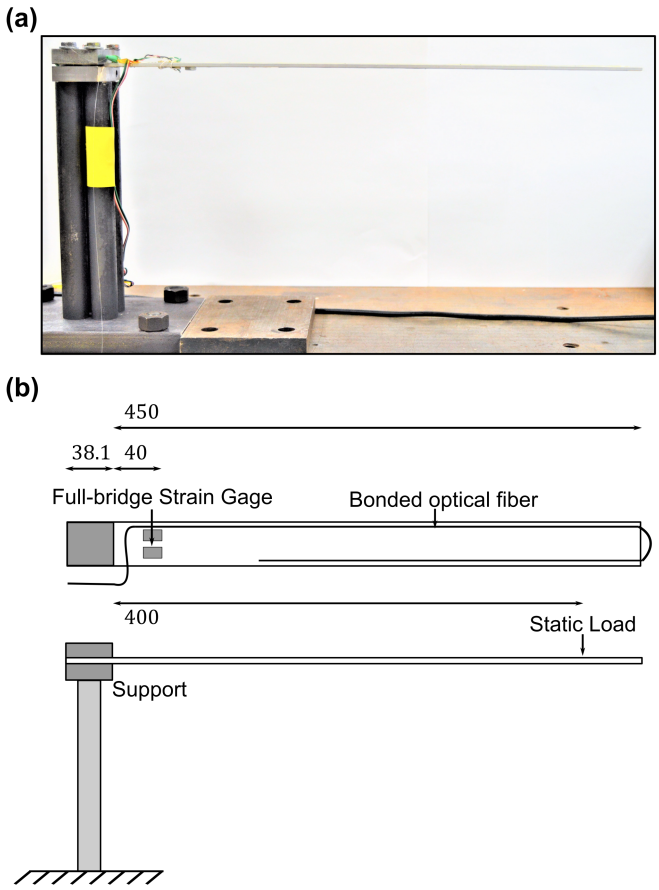

Figure 3.5: (a) Photograph and (b) schematic of the cantilever beam static experimental set up. Dimensions are in mm.

For this set of static tests, the beam is instrumented with a single FOSS fiber on its lower surface oriented in the span-wise direction. Although a section of the fiber with FBGs is looped back after reaching the tip, these sensors are not used for analysis. The first FBG is located at 20 mm from the root of the beam and each subsequent FBG is located 20 mm further down the fiber, for a total of 22 FBGs in the sensing run. A full-bridge strain gage is also located on the beam at 40 mm from the root for calibration and comparison with the FOSS strain measurement located at the same position. The signal flow for the static test is given in Fig. 3.6.

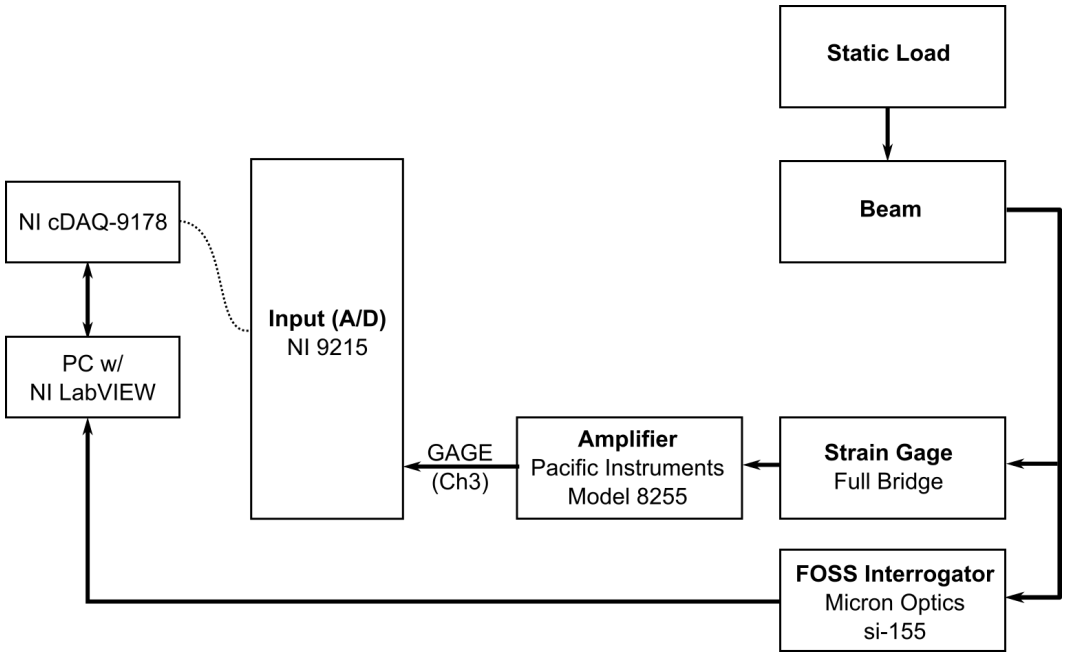

Figure 3.6: Signal flow for static testing of the cantilever beam.

Static loads are applied to the beam by a hanger and masses at 400 mm from the root. For the tip load results reported here, the x-coordinate is normalized by 400 mm, i.e. $\hat{x} = 1$ at $x = 400$. This location is chosen in order to facilitate the application of static loads, which would be practically difficult to accomplish directly at the beam tip. Five different mass loads are applied: 100, 200, 300, 400, and 500 g. Each increasing load is applied slowly and measurements taken after 60 s in order to allow any transient vibration to damp out. For each loading, FOSS and strain gage measurements are taken for 10 s at a sampling rate of 1000 Hz. The mean of these data for each sensor is then used as its static strain measurement in the analysis.

The nominal photo-elastic coefficient for the FBGs, as reported by the fiber manufacturer FBGS, is $p_e = 0.22\ \varepsilon^{-1}$. To account for small differences in that sensitivity due to differential bonding location, adhesive, or manufacturing, the sensitivity of each FBG can be estimated by comparing its strain measurement with its corresponding analytical value

for a given load case. This calibration process is completed for all five load cases and the sensitivity for each gage estimated as the mean of these comparisons. Based on this method, the empirical photo-elastic coefficients for the gages in this sequence of tests ranged from 0.19 to 0.22 ε^{-1}, with a mean value of 0.22 ε^{-1}.

Static Results

In Fig. 3.7(a), the calculated curvature distribution based on the splined FOSS measurements is shown for each load case and compared with: (1) the calculated curvature based on the strain gage and (2) the analytical curvature based on the measured tip deflection.

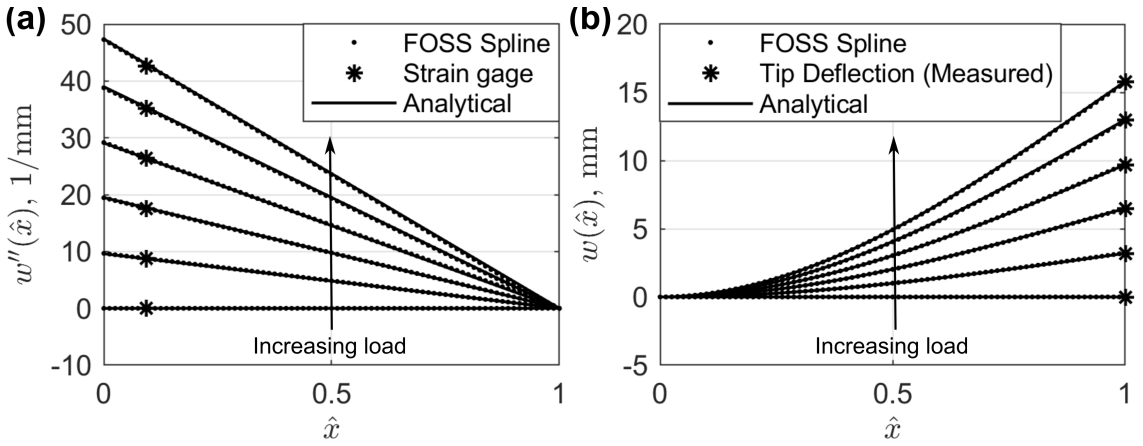

Figure 3.7: (a) Curvature and (b) deflection of the cantilever beam based on integration of static experimental FOSS strain data for concentrated loads applied at 400 mm.

The analytical curvature profiles are determined by evaluating Eqn. 2.33 for the tip deflection ($\hat{x} = 1$), yielding the expression: $w(1) = \frac{Fl^3}{3EI_y}$. Substituting this relationship into Eqn. 2.34, the curvature distribution for a measured tip deflection, $w(1)$, is given by:

$$\frac{d^2w(\hat{x})}{d\hat{x}^2} = 3(1-\hat{x}) \cdot w(1) \tag{3.9}$$

The splined FOSS data is then integrated twice using the method described above and compared to the analytical deflection based on the measured tip deflection in Fig. 3.7(b). The relative errors between the FOSS estimated and measured tip deflections are reported in Table 3.3.

Table 3.3: Error between FOSS estimated and measured static tip deflections.

Load Case	Tip Mass (g)	Error
1	100	-0.90%
2	200	0.18%
3	300	-0.30%
4	400	0.59%
5	500	0.43%

With errors less than 1% for all cases, the results based on the described integration method are relatively accurate even though strain measurements are only available at 20 locations on the "shortened" beam section. Using an OFDR system would likely provide even more accurate integrated results as less interpolation would be required to achieve high strain resolution throughout the beam.

Mode Shape Testing

A similar bench top test setup is used to validate the accuracy of the integration routine for determining the mode shapes of a vibrating cantilever beam. A schematic and image of the test setup are given in Fig. 3.8.

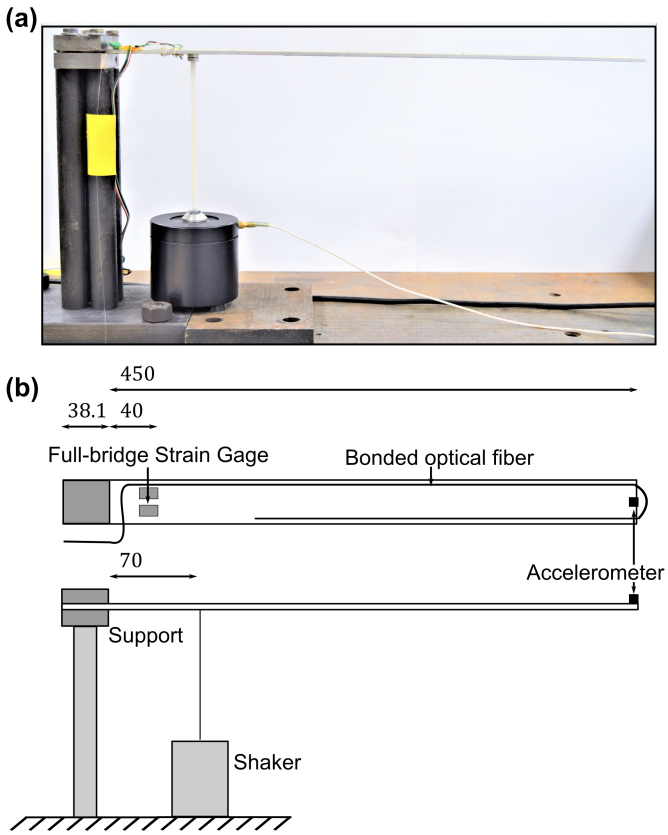

Figure 3.8: (a) Photograph and (b) schematic of the cantilever beam dynamic experimental set up.

The same beam is used here as above and the material and geometric properties are the same as those given in Table 3.1. The only two additions to the experimental set up are a shaker positioned at 70 mm from the beam root and an accelerometer positioned at the beam tip. The signal flow for the experiment is given in Fig. 3.9.

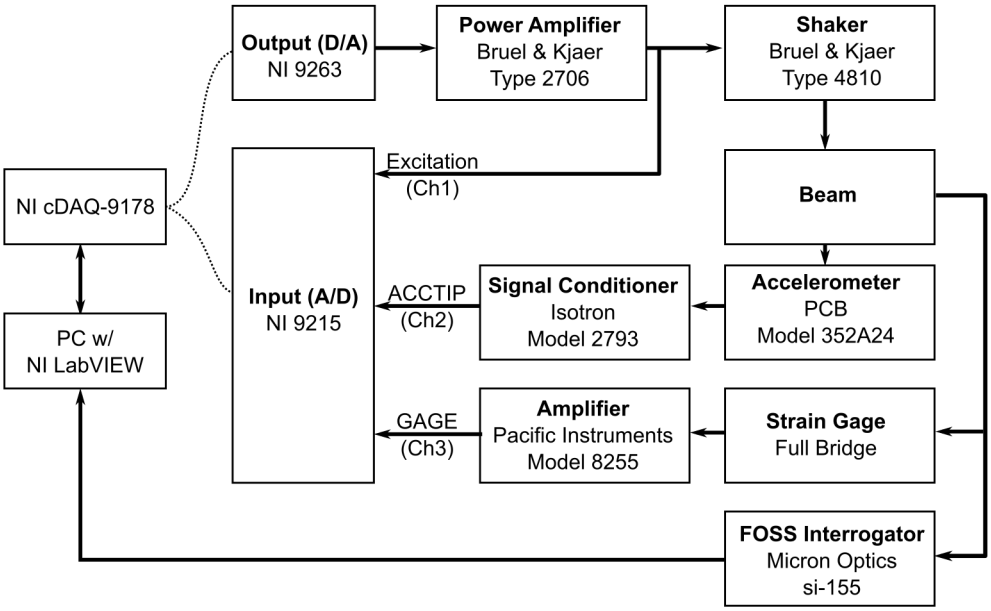

Figure 3.9: Signal flow for dynamic testing of the cantilever beam.

A sine sweep from 2-450 Hz with frequency steps of 0.1 Hz at a constant amplitude of excitation is conducted in order to determine the frequency response at each FBG. At each frequency, 10 cycles of excitation are recorded at a sampling rate of 1000 Hz. The standard deviation of this time data is then computed to yield an estimated amplitude of the strain response at each sensor for each frequency. The mean of the calibrated photo-elastic coefficient, which is equal to the nominal value reported by the manufacturer ($p_e = 0.22\,\varepsilon^{-1}$), is used for all FBGs in these tests.

Mode Shape Results

In Fig. 3.10, the character of the strain distribution as a function of the frequency of excitation is illustrated, where the absolute value of the strain amplitude is plotted for each FBG. As the frequency increases from top to bottom, the absolute value of the strain at each sensor is plotted as a color map, with dark blue corresponding to low absolute strain and dark red to

high absolute strain. The regions of high strain response occur near the resonant frequencies of the beam, and the movement of and increase in curvature nodal points can be observed as the frequency increases by tracking the dark blue regions at these resonant frequencies. Detailed plots of the regions around the first four bending resonant frequencies are shown in Fig. 3.11.

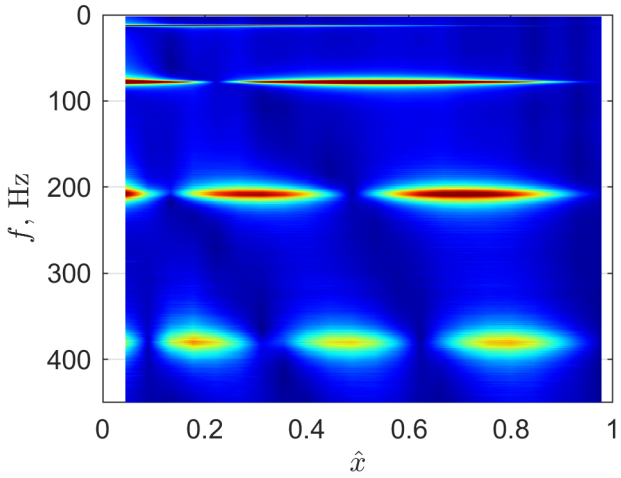

Figure 3.10: Strain distribution in the cantilever beam subjected to pure tone excitation as a function of excitation frequency. Color map with dark blue/dark red corresponding to low/high absolute strain.

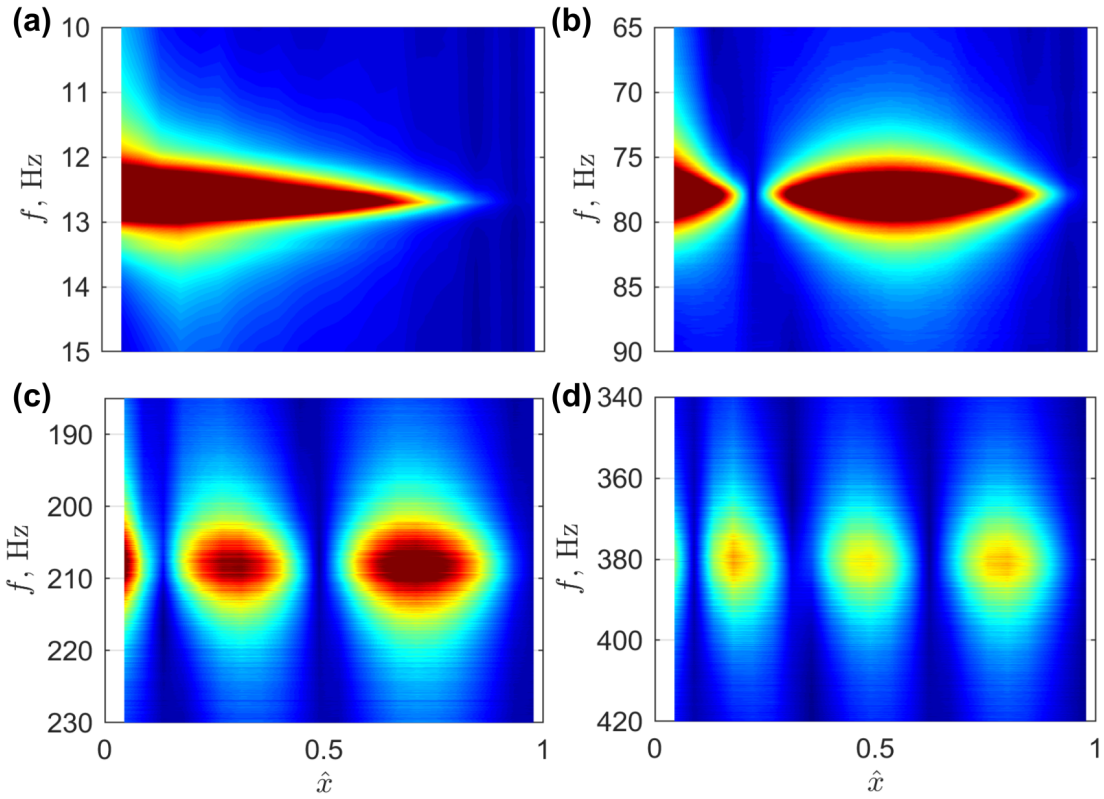

Figure 3.11: Detail of strain distribution in the cantilever beam subjected to pure tone excitation for the regions around the first four resonant frequencies. Color map with dark blue/dark red corresponding to low/high absolute strain. (a-d) Modes 1-4.

In order to determine the experimental resonant frequencies of the beam, the total strain is calculated at each excitation frequency. This response metric, plotted in Fig. 3.12, is less noisy than the strain at any particular FBG and yields an improved estimate of the frequencies corresponding to maximum total strain response.

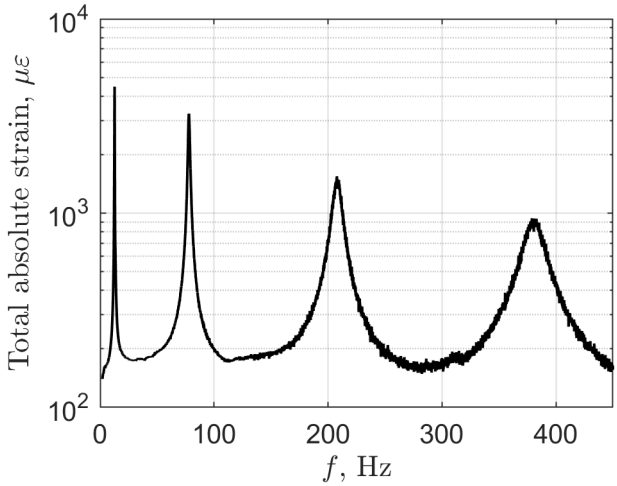

Figure 3.12: Total measured strain in the cantilever beam as a function of excitation frequency.

The experimental resonant frequencies are then determined by choosing the four frequencies at which the total strain in the beam has a peak.

The normalized FOSS curvature splines at these identified resonant frequencies are plotted in Fig. 3.13(a) along with the analytical curvature shapes developed in Chapter 2. The normalization of the experimental data is conducted by adjusting a scaling factor to minimize the least squares residual between the analytical and scaled experimental curvature shapes. The reason for this scaling is to directly compare the shapes of the curvature distributions. The FOSS spline is then integrated twice to yield the normalized mode shapes, which are plotted with the analytical mode shapes in Fig. 3.13(b).

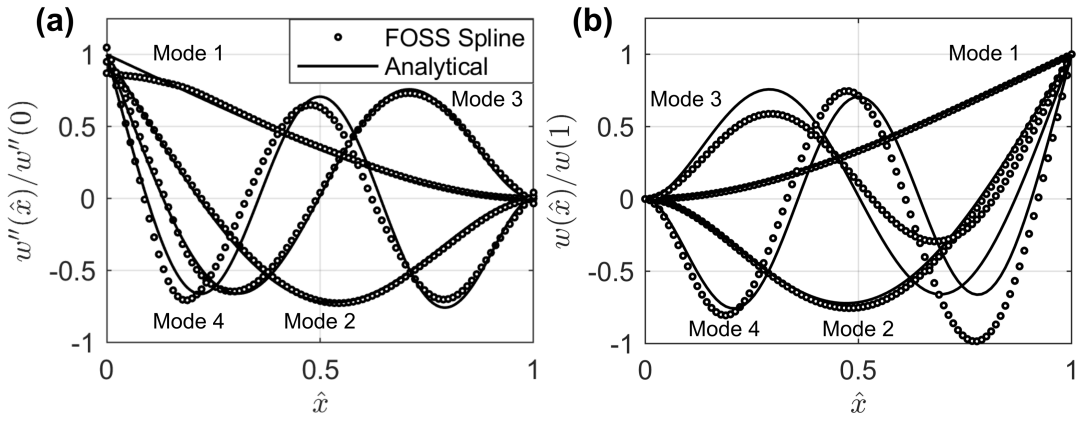

Figure 3.13: (a) Curvature and (b) mode shapes of the cantilever beam based on integration of experimental FOSS strain data.

The curvature distributions based on FOSS agree relatively well with the analytical functions, although the accuracy does decrease as the mode number increases. The integrated mode shapes follow the same pattern, where the differences in shape increase for higher modes. These differences may be attributable to physical differences between the experiment and the analytical model or to experimental uncertainties, but the relative accuracy of these methods and correspondence to the results of Euler-Bernoulli beam theory, particularly for the first two modes, is notable.

Resonant Frequency Comparison

In this section, the beam resonant frequencies deduced from experimental data are compared with the predictions based on the models described in Chapter 2. Although the natural frequency is only one parameter to be identified in modal analysis, it is useful for comparing the accuracy of the analytical models with experimental systems. Comments on and procedures for the estimation of the damping ratio will be discussed in Chapter 4, where a case study of the first beam bending mode is thoroughly analyzed.

Although the torsion and bending modes about the z-axis are not estimated experi-

mentally due to the transverse method of excitation, the different analytical predictions will be compared here for the specimen properties given in Table 3.1. Based on the infinite series method of determining J for rectangular sections (Eqn. 2.95), the torsional constant for the beam geometry in Table 3.1 is $J = 394.562$ mm^4 based on evaluating 10 terms in the series. This is the value used in the reported results. If the approximate equation were used instead (Eqn. 2.94), the computed torsional constant is 394.571 mm^4, so the approximate equation would yield predicted torsional natural frequencies approximately equal to those reported below.

The beam FE model was analyzed in MSC NASTRAN 2018.0 [49] using SOL 103 (normal modes analysis)[1]. Two models were analyzed, one created with CBEAM elements and the other with CQUAD4 elements, in order to determine the impact of modeling the beam using more elements approaching the real three-dimensional structure. The mesh for both elements was refined until convergence in the reported natural frequencies to three decimal places.

The analytical natural frequencies of the beam can be computed using the properties in Table 3.1 and the lumped and distributed parameter models described in Chapter 2. These values and those determined experimentally are summarized in Table 3.4.

Table 3.4: Comparison of theoretical and experimental resonant frequencies for the cantilever beam (Hz). Theoretical models do not include damping.

Method	Mode 1 (Bending 1)	Mode 2 (Bending 2)	Mode 3 (Bending 3)	Mode 4 (Bending 4)	Mode 5 (Torsion 1)	Mode 6 (Bending 5)
Lumped Parameter	13.2	-	157.7	-	309.9	-
Distributed Parameter	13.0	81.7	155.4	228.8	281.1	448.4
FE (CBEAM)	13.0	81.7	155.4	228.8	281.1	448.4
FE (CQUAD4)	13.1	82.4	154.6	230.8	296.5	453.0
Experimental	12.7	77.8	-	207.8	-	380.5

[1]A brief note on FE analysis using beam elements is given in Appendix E.

As expected, the analytical natural frequencies using the distributed parameter model and the CBEAM FE model correspond exactly. The lumped parameter model, on the other hand, yields natural frequencies slightly greater than these models due to its increased stiffness as a result of assuming the static deflection shape. The natural frequencies determined using the CQUAD4 FE model are comparable to those predicted using the other methods.

All bending modes reported in Table 3.4 are bending modes about the y-axis shown in Fig. 2.1 except for the "Bending 3" mode, which is bending about the z-axis. The lumped parameter estimate for this bending mode about the z-axis is based on the model given by Eqn. 2.121, where the mode's natural frequency is determined by switching the role of the cross section width and height in the computation of its second moment of area.

For the four bending modes about the y-axis (Modes 1, 2, 4, and 6), the distributed parameter/CBEAM FE model estimates have natural frequencies slightly less than those predicted by the CQUAD4 FE model. A part of these differences results from the former two models having slightly lower bending stiffness than the cylindrical bending stiffness of an equivalent plate. From Eqn. 2.54, $\frac{EI}{\rho AL^4} = \frac{Eh^2}{12\rho L^4}$ is the term multiplying the fourth-power of the eigenvalues to yield the squared natural frequencies of a beam. Poisson's ratio, ν, does not figure into this calculation. For cylindrical bending of a plate, on the other hand, the corresponding term is $\frac{D}{\rho hL^4} = \frac{Eh^2}{12(1-\nu^2)\rho L^4}$ by Eqn. 2.150. The difference, therefore, is the appearance of ν for cylindrical plate bending. Since $0 \leq \nu \leq 0.5$ for isotropic materials [44], the plate bending term is at least as large as the beam bending term for the same material and geometric properties. If $\nu = 0$ the terms are the same, but for $\nu > 0$ the plate term is larger (i.e. the system is more stiff) which contributes to the increased natural frequency estimates.

Although there is a general agreement between the theoretical and experimental values, the relative difference between them increases as the mode number increases. The influence of damping on the experimental values, which is not accounted for in the theoretical models (analytical and FE), is a contributing factor to these increasing differences. In

addition to the increasing structural and air damping as the excitation frequency increases, the impact of experimental conditions (e.g. unmodeled mass/stiffness contributions from shaker/sensors/boundary conditions) increases for higher excitation frequencies.

3.4 Shape Estimation from Strain Field: Cantilever Plate

This section begins by extending the method of integrating distributed strain measurements to the case of estimating twist. Next, the approximate plate mode shapes based on beam functions and the corresponding frequency parameters are determined for a specific plate geometry. The bending and twist numerical methods are then compared with experimental data for a cantilever plate.

3.4.1 Estimating Twist Rate from Measured Strain

Establishing the analytical foundation for using axial strain measurements to make deductions about the deformation of a plate is somewhat more involved than the curvature/strain relationship previously established for beam bending. It will be shown here that axial strain on the surface of a plate can be used not only to determine the curvature due to bending but also the rate of twist.

Measuring Shear Strain

The first task will be to show that the shear strain, ε_{xy}, can be determined based on the principal tensile strain in a 45-deg orientation, $\varepsilon_{x'x'}$. The primed axes refer to a 45-deg rotation from the unprimed axes as shown in Fig. 3.14.

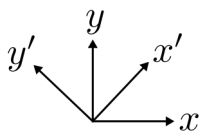

Figure 3.14: Reference coordinate axes for shear and axial strain.

The strain in the direction of the rotated x'-axis can be determined by the strain in the unrotated axes using the transformation equation for strain [35]:

$$\varepsilon_{x'x'} = a_{x'x}^2 \varepsilon_{xx} + 2a_{x'x}a_{x'y}\varepsilon_{xy} + a_{x'y}^2 \varepsilon_{yy} = \frac{1}{2}\left(\varepsilon_{xx} + \varepsilon_{yy}\right) + \varepsilon_{xy}\,, \tag{3.10}$$

where the direction cosines between the two frames are $a_{x'x} = a_{x'y} = \frac{\sqrt{2}}{2}$ for a 45-deg rotation. Under pure torsion, however, $\varepsilon_{xx} = \varepsilon_{yy} = 0$, so:

$$\varepsilon_{x'x'} = \varepsilon_{xy}\,. \tag{3.11}$$

Thus, measurement of the axial strain in the x'-direction is equivalent to measurement of the shear strain in the unrotated axes for pure torsion. Similarly, strain in the direction of the rotated y'-axis can be determined by the strain in the unrotated axes using the transformation equation for strain:

$$\varepsilon_{y'y'} = a_{y'x}^2 \varepsilon_{xx} + 2a_{y'x}a_{y'y}\varepsilon_{xy} + a_{y'y}^2 \varepsilon_{yy} = \frac{1}{2}\left(\varepsilon_{xx} + \varepsilon_{yy}\right) - \varepsilon_{xy} = -\varepsilon_{xy}\,, \tag{3.12}$$

where the direction cosines between two frames are $a_{y'x} = -a_{y'y} = -\frac{\sqrt{2}}{2}$ for a 45-degree rotation and $\varepsilon_{xx} = \varepsilon_{yy} = 0$ for pure torsion.

Twist Rate from Shear Strain

Next, the relationship between the twist rate and the shear strain will be derived [35, 50]. Consider the arbitrary cross section shown in Fig. 3.15, where r is the distance from point P to the origin, θ is the angle of twist, and β is the angle between the y-axis and P.

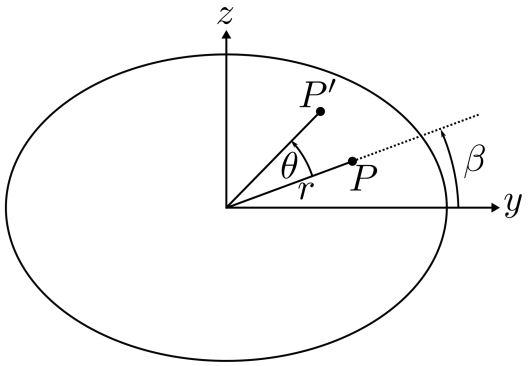

Figure 3.15: Arbitrary cross section of a beam.

The displacement field from P to P' is given by:

$$\begin{aligned} u &= \varkappa(y,z) \\ v &= -r\theta(x)\sin\beta = -\theta(x)z \\ w &= r\theta(x)\cos\beta = \theta(x)y\,, \end{aligned} \tag{3.13}$$

where u,v, and w are the displacements in the x-, y-, and z-directions, and $\varkappa$ is a function describing warping in the x-direction. Substituting the assumed constant twist rate relationship, $\theta(x) = \alpha x$, where α is the twist rate:

$$\begin{aligned} u &= \varkappa(y,z) \\ v &= -\alpha xz \\ w &= \alpha xy\,. \end{aligned} \tag{3.14}$$

From this displacement field, the strain field can be written[2]:

$$\begin{aligned}
\varepsilon_{xx} &= \partial_x u = 0 \\
\varepsilon_{yy} &= \partial_y v = 0 \\
\varepsilon_{zz} &= \partial_z w = 0 \\
\varepsilon_{xy} &= \frac{1}{2}\left(\partial_y u + \partial_x v\right) = \frac{1}{2}\left(\partial_y \varkappa - \alpha z\right) \\
\varepsilon_{yz} &= \frac{1}{2}\left(\partial_z v + \partial_y w\right) = \frac{1}{2}\left(-\alpha x + \alpha x\right) = 0 \\
\varepsilon_{xz} &= \frac{1}{2}\left(\partial_z u + \partial_x w\right) = \frac{1}{2}\left(\partial_z \varkappa + \alpha y\right) .
\end{aligned} \tag{3.15}$$

By Hooke's Law ($\varepsilon_{ij} = \frac{1}{E}\left[\left(1+\nu\right)\tau_{ij} - \nu\tau_{kk}\delta_{ij}\right]$), these strain components can also be written in terms of the stress components:

$$\begin{aligned}
\varepsilon_{xx} &= \frac{1}{E}\left[\tau_{xx} - \nu\left(\tau_{yy} + \tau_{zz}\right)\right] = 0 \\
\varepsilon_{yy} &= \frac{1}{E}\left[\tau_{yy} - \nu\left(\tau_{xx} + \tau_{zz}\right)\right] = 0 \\
\varepsilon_{zz} &= \frac{1}{E}\left[\tau_{zz} - \nu\left(\tau_{xx} + \tau_{yy}\right)\right] = 0 \\
\varepsilon_{xy} &= \frac{1+\nu}{E}\tau_{xy} = \frac{1}{2}\left(\partial_y \varkappa - \alpha z\right) \\
\varepsilon_{yz} &= \frac{1+\nu}{E}\tau_{yz} = 0 \\
\varepsilon_{xz} &= \frac{1+\nu}{E}\tau_{xz} = \frac{1}{2}\left(\partial_z \varkappa + \alpha y\right) .
\end{aligned} \tag{3.16}$$

Based on the valid range for Poisson's ratio, the only solution to the first three equations is $\tau_{xx} = \tau_{yy} = \tau_{zz} = 0$, and from the fifth, $\tau_{yz} = 0$. The only two non-zero stresses are thus:

$$\begin{aligned}
\tau_{xy} &= G\left(\partial_y \varkappa - \alpha z\right) \\
\tau_{xz} &= G\left(\partial_z \varkappa + \alpha y\right) ,
\end{aligned} \tag{3.17}$$

[2] As in the plate section of Chapter 2, the compact notation for vector fields, tensors, and partial differentiation will be employed. As a reminder: (1) components of a vector field or tensor will be denoted with subscripts, e.g. τ_{xy} indicates the xy cross term of the stress tensor and (2) partial differentiation with respect to a variable, here x for example, will be shortened as $\frac{\partial}{\partial x}\left(\cdot\right) = \partial_x$

where $G = \frac{E}{2(1+\nu)}$ is the shear modulus. A useful relationship between these stresses is:

$$\partial_z \tau_{xy} - \partial_y \tau_{xz} = G\left(\partial_{yz}\varkappa - \alpha\right) - G\left(\partial_{yz}\varkappa + \alpha\right) = -2G\alpha\,. \tag{3.18}$$

In static equilibrium and with no body forces, the equations of motion require that $\partial_j \tau_{ij} = 0$:

$$\begin{aligned} \partial_x \tau_{xx} + \partial_y \tau_{xy} + \partial_z \tau_{xz} &= 0 \\ \partial_x \tau_{yx} + \partial_y \tau_{yy} + \partial_z \tau_{yz} &= 0 \\ \partial_x \tau_{zx} + \partial_y \tau_{zy} + \partial_z \tau_{zz} &= 0\,. \end{aligned} \tag{3.19}$$

The second two equations are trivially satisfied, as each term is individually zero. In the first equation, $\tau_{xx} = 0$, so the only non-trivial relationship from the equations of equilibrium is:

$$\partial_y \tau_{xy} + \partial_z \tau_{xz} = 0\,. \tag{3.20}$$

In order to determine the stress distribution which satisfies this equation of equilibrium, the Prandtl stress function $\varphi(y, z)$, can be defined such that:

$$\begin{aligned} \tau_{xy} &= \partial_z \varphi \\ \tau_{xz} &= -\partial_y \varphi\,. \end{aligned} \tag{3.21}$$

Employing this definition in Eqn. 3.18 results in the Poisson equation:

$$\partial_{zz}\varphi + \partial_{yy}\varphi = -2G\alpha\,. \tag{3.22}$$

The necessary boundary conditions of this function can be found by determining the boundary conditions for the stress distribution. For the case of zero tractions, the stress must satisfy $\tau_{ij}\nu_j = 0$ on the boundary, where ν_j is the direction cosine of the outward pointing

normal $\boldsymbol{\nu}$ in the j-direction.

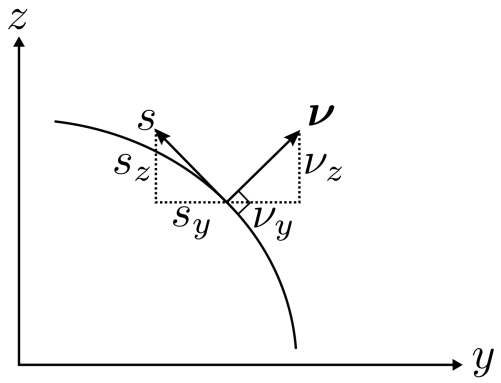

Figure 3.16: Normal and tangential vectors on the cross section of a beam.

Since the beam is assumed to be prismatic, the outward pointing normal only has components in the y- and z-directions, so the boundary conditions are:

$$\begin{aligned} \tau_{xy}\nu_y + \tau_{xz}\nu_z &= 0 \\ \tau_{yy}\nu_y + \tau_{yz}\nu_z &= 0 \\ \tau_{zy}\nu_y + \tau_{zz}\nu_z &= 0\,. \end{aligned} \tag{3.23}$$

The second and third lines are trivially satisfied based on the zero components of the stress tensor given in Eqn. 3.16. From the geometry shown in Fig. 3.16, the outward pointing normal $\boldsymbol{\nu}$ can be written in terms of the tangential unit vector $\boldsymbol{s}$ by a 90-degree rotation matrix:

$$\begin{Bmatrix} s_y \\ s_z \end{Bmatrix} = \begin{bmatrix} 0 & -1 \\ 1 & 0 \end{bmatrix} \begin{Bmatrix} \nu_y \\ \nu_z \end{Bmatrix} = \begin{Bmatrix} -\nu_z \\ \nu_y \end{Bmatrix}. \tag{3.24}$$

Substituting the corresponding definitions from Eqn. 3.21 and the tangential directions into

Eqn. 3.23:

$$\begin{aligned} \partial_z \varphi \; s_z + \partial_y \varphi \; s_y &= 0 \\ \Rightarrow \nabla \varphi \cdot \boldsymbol{s} &= 0 \,. \end{aligned} \tag{3.25}$$

Thus, the gradient of the function φ is zero, i.e. φ is constant, along the boundary of the cross section. Since adding any constant value to φ will not change the stress distributions defined in Eqn. 3.21, its value at the boundary is chosen to be zero.

A useful heuristic developed by Prandtl is known as the "membrane analogy" [50]. Noting that the governing equations of the Prandtl stress function for torsion and the deflection of an elastic membrane under uniform pressure are the same, useful insight for the torsion problem can be gained through an understanding of the membrane problem. Approaching the torsion problem using the membrane analogy, consider a rectangular opening over which an elastic membrane is stretched and a uniform pressure is applied to one side. The deformation of the membrane, calculated based on the Fourier series torsion solution in [51], is shown in Fig. 3.17.

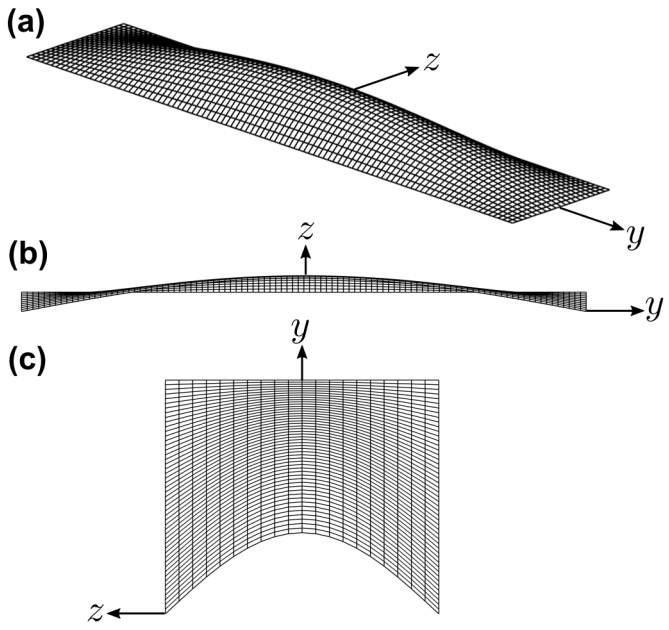

Figure 3.17: (a) Membrane deformation for rectangular cross section (aspect ratio 5) under uniform pressure. (b) Section view in z-direction at 20-deg above horizontal. (c) Section view in y-direction at 20-deg above horizontal.

One particularly useful observation is that the slope of the membrane, and thus of the stress function, is greatest at the midpoint of the long sides of the cross section. Additionally, in the center region far from the narrow ends of the cross section, the stress function is parabolic and approximately constant for small changes in y.

Based on the definition of the stress function φ in Eqn. 3.21, the shear stresses due to torsion are greatest where the gradient of φ is greatest. Thus, from the first observation above, the maximum shear stresses are located at the midpoint of the long cross-sectional side. Another useful representation of the membrane solution is given in Fig. 3.18, where the contour lines of φ clearly demonstrate: (1) the maximum gradient is at the midpoint of the long side and (2) far from the narrow ends, there is a center region where $\partial_y \varphi \approx 0$.

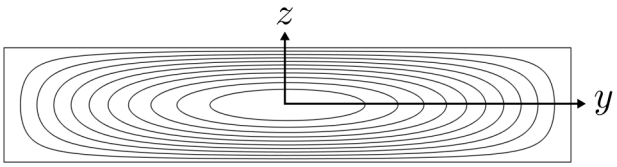

Figure 3.18: Rectangular cross section of beam (aspect ratio 5) with contour lines of the Prandtl stress function, φ.

Thus, for a narrow rectangular cross section, far from the narrow ends it can be assumed that $\partial_{yy}\varphi \approx 0$ since the contour lines are mostly parallel to the y-axis in this region. For this case, the Poisson equation of the stress function, Eqn. 3.22, reduces to:

$$\partial_{zz}\varphi = \varphi''(z) = -2G\alpha\,. \tag{3.26}$$

This equation can be integrated twice to find:

$$\varphi(z) = -G\alpha z^2 + C_1 z + C_2\,. \tag{3.27}$$

Now applying the boundary condition, $\varphi\left(\pm\frac{h}{2}\right) = 0$, the solution for the stress function is:

$$\varphi(z) = G\alpha\left(\frac{a^2}{4} - z^2\right)\,. \tag{3.28}$$

Substituting this solution into Eqn. 3.21 yields the only component of shear stress and the corresponding shear strain:

$$\begin{aligned} \tau_{xy} &= -2G\alpha z \\ \varepsilon_{xy} &= -\alpha z\,, \end{aligned} \tag{3.29}$$

where the second equality is a result of Hooke's Law given in Eqn. 3.16. This equation states that the maximum absolute shear strain ε_{xy} occurs where z is maximum, i.e. at the upper

and lower surfaces of the beam, which matches the observations based on the membrane analogy. Rearranging this shear strain relationship and then substituting Eqn. 3.11 results in an equation relating the twist rate α to the axial strain in the x'-direction:

$$\alpha = -\frac{1}{z}\varepsilon_{xy} = -\frac{1}{z}\varepsilon_{x'x'} \,. \tag{3.30}$$

In terms of the non-dimensional spatial coordinate $\hat{x}$, the twist rate at the surface of the plate is thus:

$$\alpha(\hat{x}) = -\frac{l}{z}\varepsilon_{x'x'} = -\frac{2l}{h} \cdot \varepsilon_{\hat{x}'\hat{x}'} \,. \tag{3.31}$$

Thus, using Eqn. 3.31, axial strain measurements oriented at 45-deg to the x-axis can be used to determine the twist rate due to torsion.

3.4.2 Approximate Mode Shapes

In this section, the results from the Rayleigh-Ritz method using products of beam functions are described for the plate geometry and properties based on the experimental specimen to be tested later. These results are then compared with those obtained using FE analysis.

Rayleigh-Ritz Method: Products of Beam Functions

Based on the method described in Chapter 2 for approximating the plate mode shapes with products of beam functions, the mode shapes and natural frequencies for a specific plate specimen are analyzed here. The plate has the same material and geometric properties, summarized in Table 3.5, of the specimen to be analyzed experimentally later.

Table 3.5: Material properties of the plate specimen.

Parameter	Variable	Value
Material		Aluminum 6061
Mass, Total	m	3.06 kg
Density	ρ	2730 kg/m^3
Elastic modulus	E	68.9 GPa [48]
Poisson's ratio	ν	0.35 [48]
Length, Total		860 mm
Length, Free	l	800 mm
Width	b	406 mm
Height	h	3.20 mm
Aspect ratio (l/b)		1.97

In the Rayleigh-Ritz method, increasing the number of candidate eigenfunctions increases the relative accuracy of the eigenvalues extracted. In Fig. 3.19, the convergence of the frequency parameters as the number of candidate modes increases is shown.

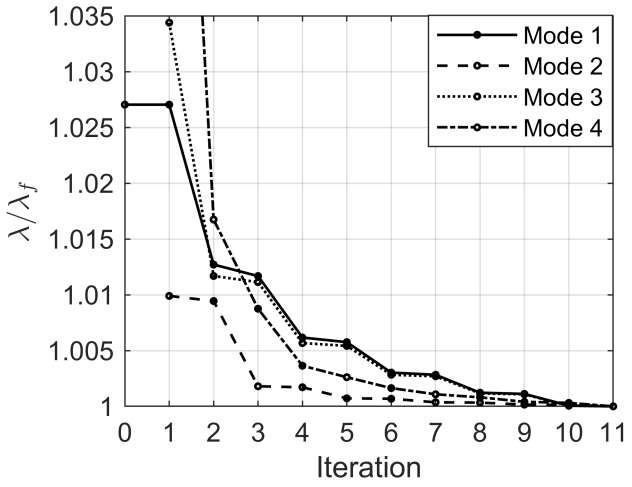

Figure 3.19: Convergence of the frequency parameters λ for the first four modes of the cantilever plate with $l/b = 1.97$ and $\nu = 0.35$ based on the Rayleigh-Ritz method and products of beam functions. The ratio λ/λ_f indicates the percent difference between the iteration value and the final value of the corresponding frequency parameter.

At each step, an additional mode shape is added in both the $\hat{x}$- and $\hat{y}$-directions and the eigenproblem solved to determine the estimated frequency parameters. As the number of mode shapes increases, each frequency parameter is converging from above towards its final value λ_f. The final frequency parameters for this plate configuration are given in Table 3.6 and the shapes corresponding to these modes, which are products of beam functions, are shown in Fig. 3.20.

Table 3.6: Frequency parameters for the cantilever plate with $l/b = 1.97$ and $\nu = 0.35$ based on the Rayleigh-Ritz method and products of beam functions.

Mode	Description	λ
1	Bending 1	3.4271
2	Torsion 1	14.167
3	Bending 2	21.313
4	Torsion 2	46.459

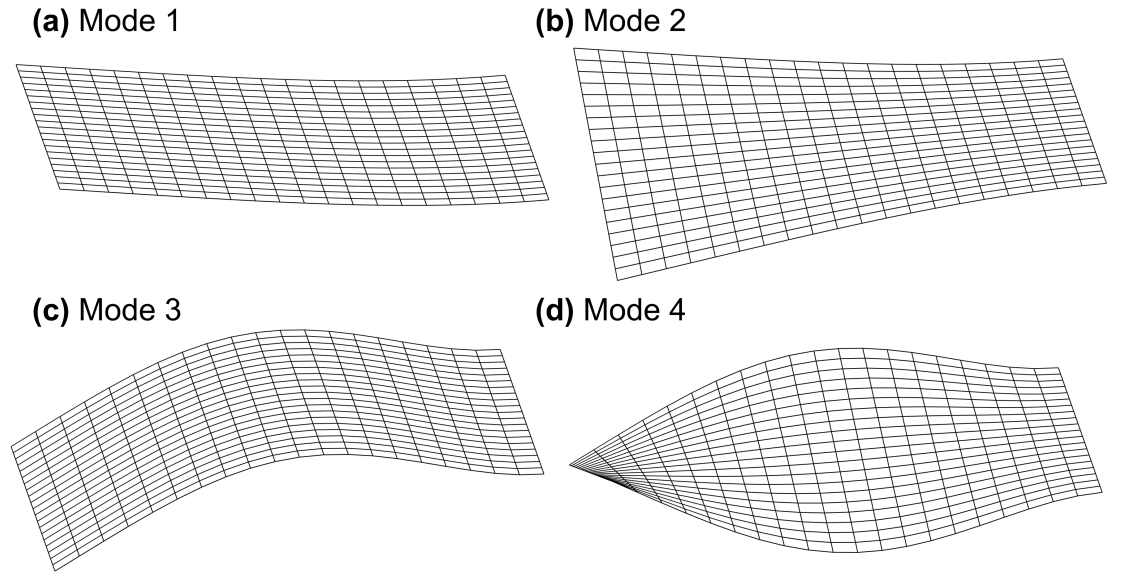

Figure 3.20: Mode shapes of the cantilever plate based on products of beam functions (clamped-free and free-free) – the clamped edge is on the right.

The beam functions for these modes are specified in Table 3.7, where the clamped-free modes ϕ_r are as summarized in Table 2.2, $\chi_1^r = 1$ is the first free-free rigid body mode, and $\chi_2^r = 1 - 2\hat{y}$ is the second free-free rigid body mode.

Table 3.7: Approximate mode shapes corresponding to the first four cantilever plate modes.

Mode	Mode shape based on product of beam functions
1 (Bending 1)	$w_1(\hat{x},\hat{y}) = \phi_1(\hat{x})\chi_1^r(\hat{y}) = \phi_1(\hat{x})$
2 (Torsion 1)	$w_2(\hat{x},\hat{y}) = \phi_1(\hat{x})\chi_2^r(\hat{y}) = \phi_1(\hat{x})\,(1-2\hat{y})$
3 (Bending 2)	$w_3(\hat{x},\hat{y}) = \phi_2(\hat{x})\chi_1^r(\hat{y}) = \phi_2(\hat{x})$
4 (Torsion 2)	$w_4(\hat{x},\hat{y}) = \phi_2(\hat{x})\chi_2^r(\hat{y}) = \phi_2(\hat{x})\,(1-2\hat{y})$

For a given mode shape $w(\hat{x},\hat{y})$, the twist θ is calculated by the cross partial derivative

$\partial_{\hat{x}\hat{y}} w$ and the twist rate by $\frac{1}{l}\partial_{\hat{x}}\theta$. These relationships are summarized in Eqn. 3.32.

$$\begin{aligned} \theta(\hat{x},\hat{y}) &= \frac{1}{bl}\partial_{\hat{x}\hat{y}} w(\hat{x},\hat{y}) \\ \alpha(\hat{x},\hat{y}) &= \frac{1}{bl^2}\partial_{\hat{x}\hat{x}\hat{y}} w(\hat{x},\hat{y})\,. \end{aligned} \tag{3.32}$$

Using Eqn. 3.32, the twists (and twist rates) of modes 1 and 3 in Table 3.7 are zero since their mode shapes are independent of $\hat{y}$. This can be confirmed visually in Fig. 3.20(a) and (c). The twist rates for modes 2 and 4 are:

$$\begin{aligned} \alpha_2(\hat{x}) &= \frac{1}{bl^2}\partial_{\hat{x}\hat{x}\hat{y}} w_2(\hat{x},\hat{y}) = -\frac{2}{bl^2}\phi_1''(\hat{x}) \\ \alpha_4(\hat{x}) &= \frac{1}{bl^2}\partial_{\hat{x}\hat{x}\hat{y}} w_4(\hat{x},\hat{y}) = -\frac{2}{bl^2}\phi_2''(\hat{x})\,. \end{aligned} \tag{3.33}$$

Based on these equations, the twist rates for these modes are proportional to the second derivative of the clamped-free mode shapes (and independent of $\hat{y}$). The normalized twist and twist rate shapes for these modes are shown in Fig. 3.21.

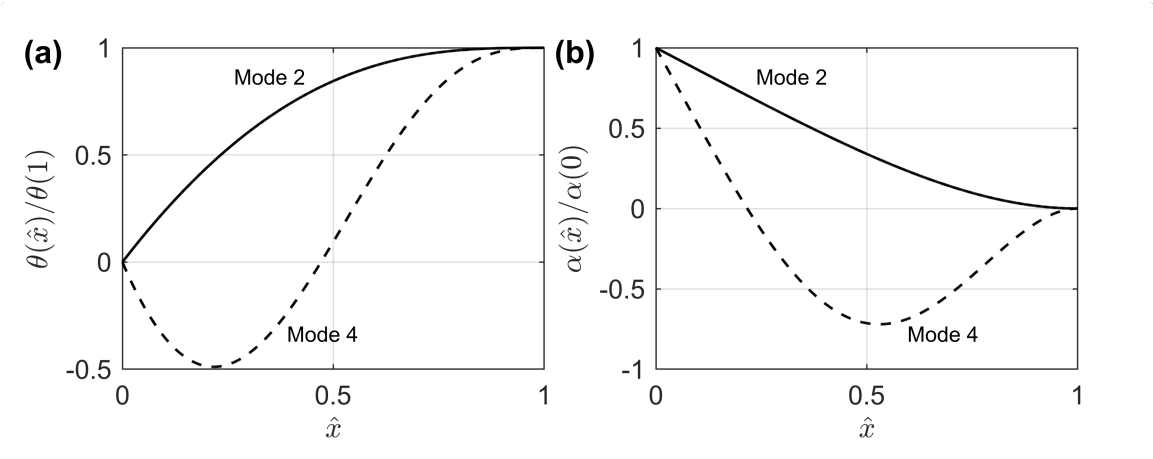

Figure 3.21: (a) Twist and (b) twist rate in the cantilever plate based on a mode shape approximation using products of beam functions.

Comparison with Finite Element

The predictions for the twist rate α based on the products of beam functions will now be compared to the shear stress distribution based on FE analysis, which by Eqn 3.31 is proportional to the twist rate. The plate FE model is analyzed in MSC NASTRAN 2018.0 [49] using SOL 103 (normal modes) and CQUAD4 elements with the same material and geometric properties of the plate specimen summarized in Table 3.5. The mesh is refined until convergence in the reported natural frequencies to three decimal places.

A comparison of the approximate mode shapes based on products of beam functions to the FE mode shapes is shown in Fig. 3.22, where the shapes are scaled to have the same absolute maximum displacement.

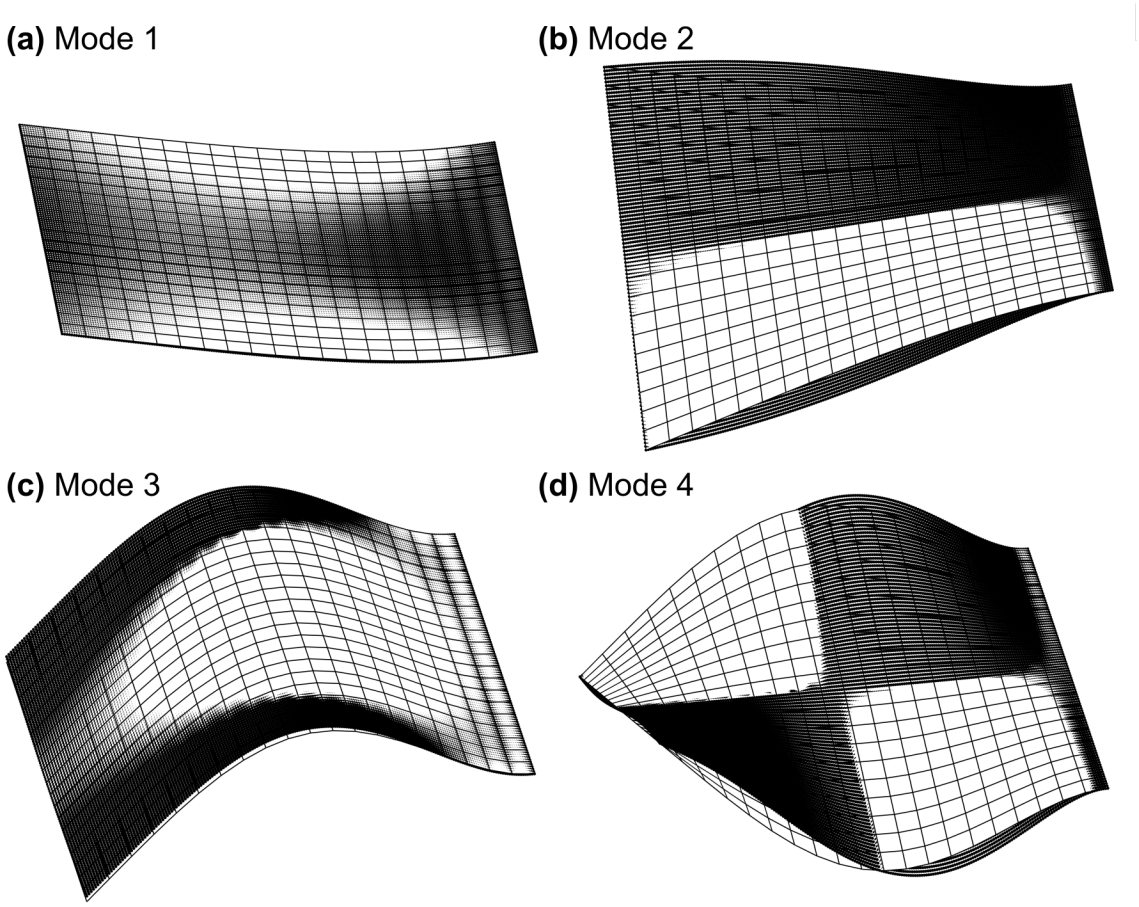

Figure 3.22: Comparison of cantilever plate mode shapes determined by products of beam functions (grids) and FE analysis (dots) – the clamped edge is on the right.

For all the modes presented, the general character of the shapes are the same for both techniques. However, it is also clear that the approximate mode shapes based on products of beam functions (plotted as gridded surfaces), do not perfectly account for the boundary conditions along the free edges. In particular, the increased stiffness of these approximate mode shapes compared to the FE shapes can be seen along the plate edges.

The FE data for three simulated fiber runs are also computed: (1) leading edge span-wise strain, (2) centerline shear strain, and (3) trailing edge span-wise strain. These strain results for the first four modes are given in Fig. 3.23.

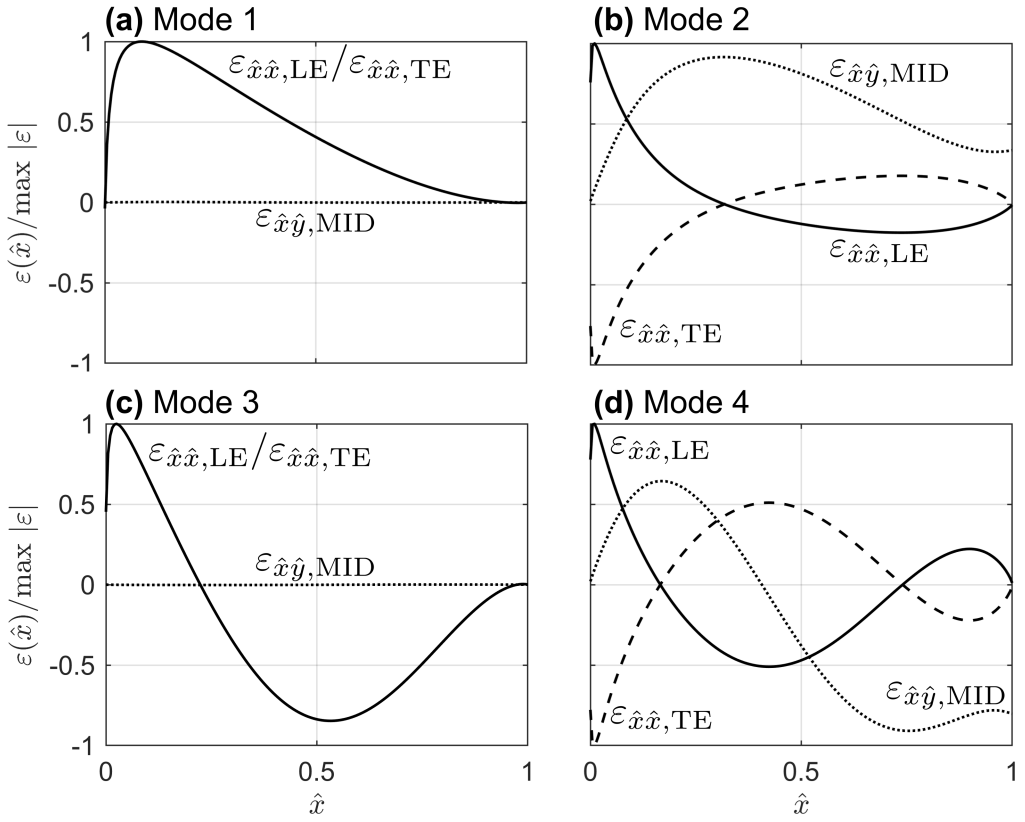

Figure 3.23: Normal strain in the leading and trailing edges, and shear strain along the mid-chord, for the first four modes based on FE model of the cantilever rectangular plate with $l/b = 1.97$ and $\nu = 0.35$.

The qualitative participation of each fiber in a particular mode can be observed in these plots. Modes 1 and 3, for example, are primarily bending modes and show identical responses for the two bending fibers (on the leading and trailing edges), which are approximately the same shape as the analytical curvatures for the first and second beam bending modes. The strain response for the torsional fiber is approximately zero for these modes.

Modes 2 and 4, on the other hand, are somewhat more complex. The expected response of the torsional fiber for modes 2 and 4, based on the products of beam functions, was previously shown in Fig. 3.21 to correspond to the curvature shapes of the first two beam bending modes. A comparison of the shape in Fig. 3.23(b) for $\varepsilon_{\hat{x}\hat{y},\mathrm{MID}}$ to that of $\varepsilon_{\hat{x}\hat{x},\mathrm{LE}}$ in

Fig. 3.23(a) shows a loose correspondence. A similar approximate correspondence can be seen in comparing the shape in Fig. 3.23(d) for $\varepsilon_{\hat{x}\hat{y},\mathrm{MID}}$ to that of $\varepsilon_{\hat{x}\hat{x},\mathrm{LE}}$ in Fig. 3.23(c). The major difference is that the tip boundary condition for the FE torsional fiber is not actually zero, so the products of beam functions do not perfectly satisfy the plate boundary conditions. This particular observation is discussed in Chapter 2.

Several additional observations for modes 2 and 4 are also of interest: (1) the response of the torsional fiber, $\varepsilon_{\hat{x}\hat{y},\mathrm{MID}}$, is of the same magnitude as the bending fibers, (2) the bending fibers respond in opposite directions to each other, and (3) the bending responses correspond approximately to the strain shapes of its preceding bending mode. The first two observations here imply two methods to identify the twisting mode shapes. Either the response of the torsional fiber can be used or the responses of the leading and trailing edge fibers compared. This second method has been used by Pak [5], where multiple longitudinally oriented fibers are used to approximate the deformation along each slice of a plate, which are then used to reconstruct the deformation of the entire structure.

3.4.3 Shape Estimation from Experimental Strain Data

The integration scheme previously described for shape estimation of a cantilever beam in bending is implemented in this section for shape estimation of a cantilever plate. The estimated mode shapes are then compared with the mode shapes based on beam functions as well as those based on FE analysis.

Mode Shape Testing

An image and schematic of the cantilever plate and fiber layout is shown in Fig. 3.24. The leading and trailing edge fibers are oriented span-wise to measure bending, and the centerline (MID) fiber is oriented in a 45-deg sawtooth pattern to measure shear strain.

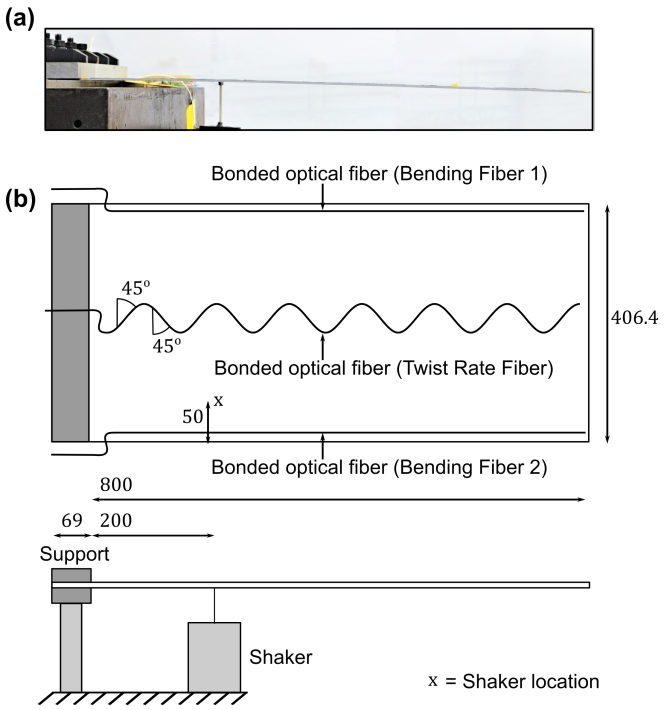

Figure 3.24: (a) Photograph and (b) schematic of the cantilever plate experimental set up.

The first FBG in the bending fibers is located 20 mm from the root of the beam, and each subsequent FBG is located 20 mm farther down the fiber. For the twist rate fiber, the first FBG is located 15 mm from the root of the beam and each subsequent FBG is located 15 mm farther down the fiber. Each fiber has a total of 39 FBGs. By Eqn. 3.11 and Eqn. 3.12, measurement of the axial strain oriented in the $y'y'$-direction for pure torsion is the opposite of the axial strain measured in the $x'x'$-direction at the same position. Thus, the convenient sawtooth layout can be utilized and the strain measurements in the $y'y'$-direction multiplied by -1 to yield the strain measurements in the $x'x'$-direction.

The plate is excited by a shaker positioned at 200 mm from the plate root and 50 mm from the edge. The signal flow for the experiment is given in Fig. 3.25.

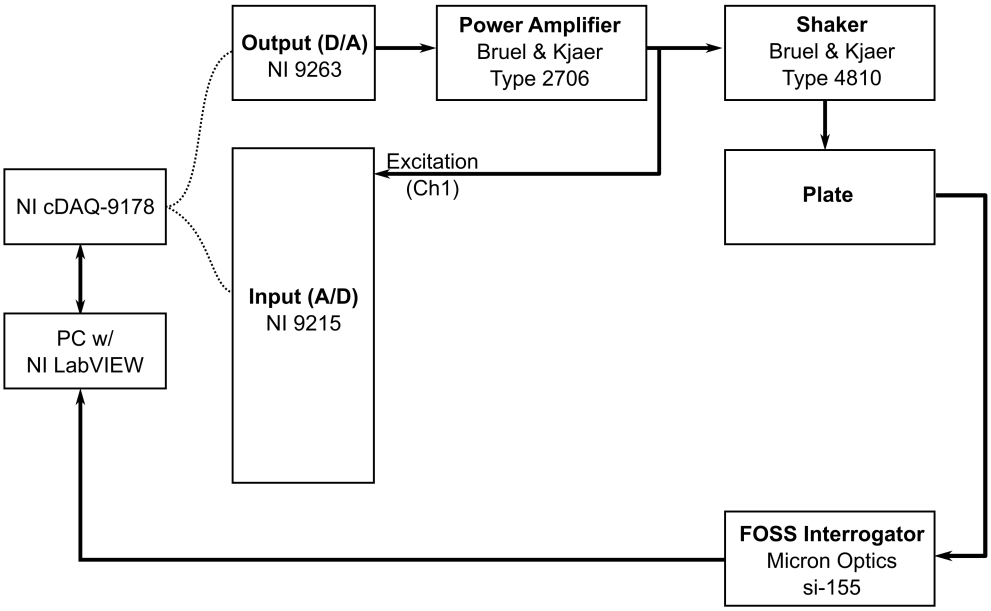

Figure 3.25: Signal flow for dynamic testing of the cantilever plate.

A sine sweep from 2-100 Hz with frequency steps of 0.1 Hz and at a constant amplitude of excitation is conducted in order to determine the strain frequency response along each fiber. At each frequency, 10 cycles of excitation are recorded at a sampling rate of 1000 Hz. The standard deviation of this time data is then computed to yield an estimated amplitude of the strain response at each sensor for each frequency. The mean of the calibrated photo-elastic coefficient, which is equal to the nominal value reported by the manufacturer ($p_e = 0.22\,\varepsilon^{-1}$), is used for all FBGs in these tests.

Mode Shape Results

In Fig. 3.26, the character of the strain distribution as a function of the frequency of excitation is illustrated where the absolute value of the strain amplitude is plotted for each FBG along each fiber. As for the figures in the beam section, the absolute value of the strain at each sensor is plotted as a color map, with dark blue corresponding to low absolute strain and

dark red to high absolute strain. The regions of high strain response occur near the resonant frequencies of the plate. Detail plots of the regions around the first five resonant frequencies are shown in Fig. 3.27. Although 39 FBGs are bonded in each of the fiber runs, the twist rate fiber sensors are positioned every 15 mm and span from 15-585 mm along the plate's total length of 800 mm.

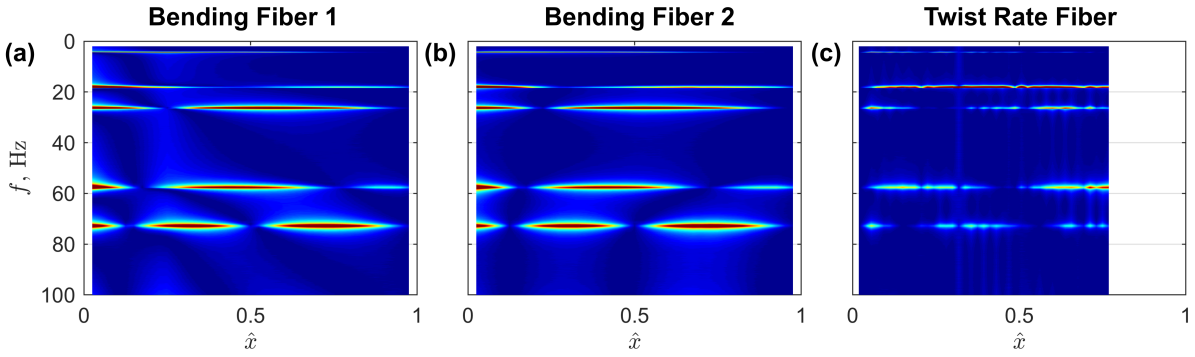

Figure 3.26: Strain distribution in the cantilever plate subjected to pure tone excitation as a function of excitation frequency. (a) Leading edge (bending) fiber. (b) Trailing edge (bending) fiber. (c) Mid-chord (twist rate) fiber. Color map with dark blue/dark red corresponding to low/high strain absolute value.

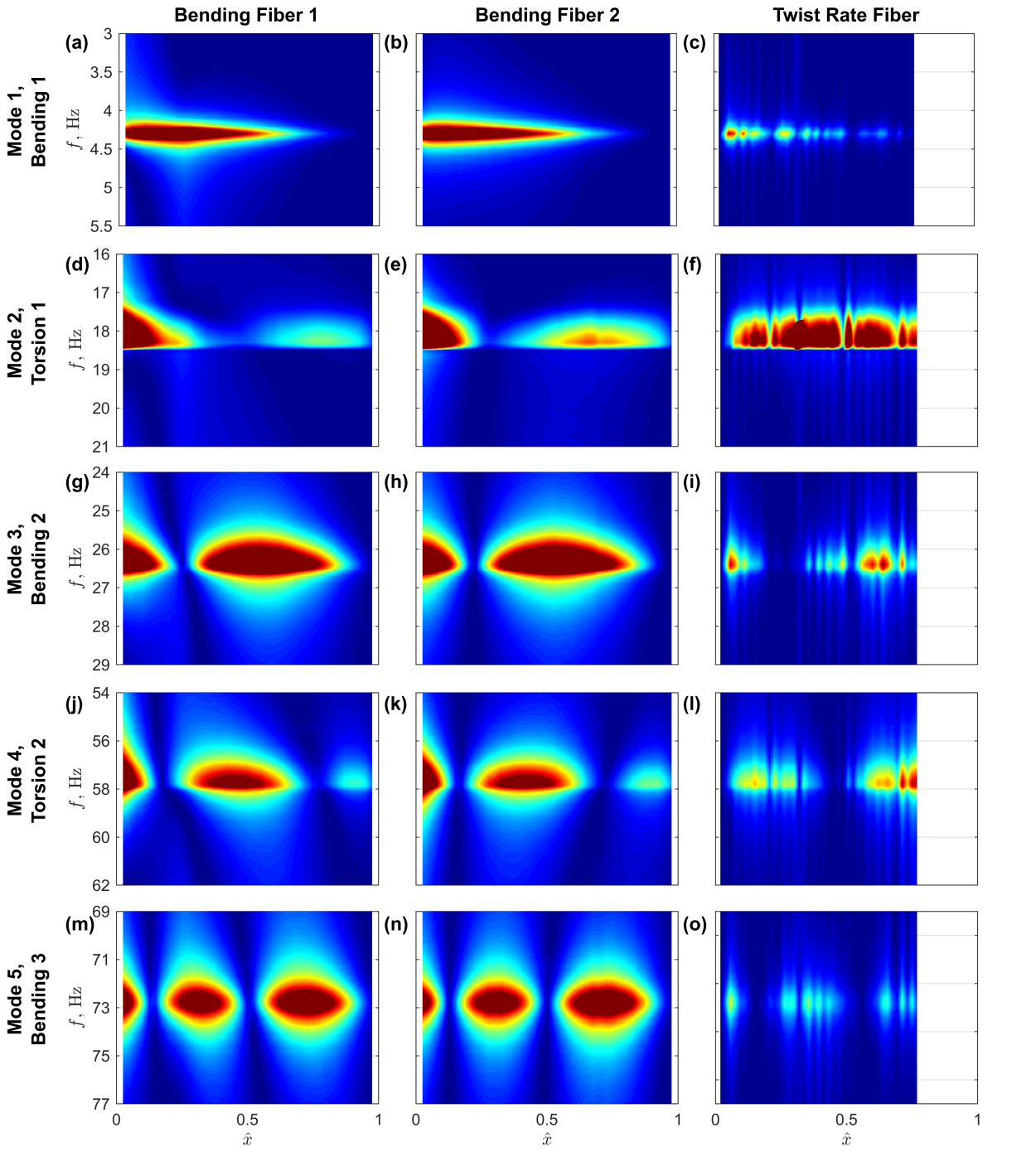

Figure 3.27: Detail of strain distribution in the cantilever plate subjected to pure tone excitation for the regions around the first five resonant frequencies. Columns correspond to the leading edge, trailing edge, and mid-chord fibers, while rows correspond to the modes. Color map with dark blue/dark red corresponding to low/high strain absolute value.

Upon visual inspection of the color map plots, it can be seen that the regions of high strain responses in each fiber correspond to the same frequency regions. In addition, although only a portion of the entire plate's length is covered with the twist rate fiber, this fiber has the largest response at the torsional modes.

In order to determine the experimental resonant frequencies of the plate, the total strain in each fiber is calculated at each excitation frequency. This response metric is plotted in Fig. 3.28 for each fiber.

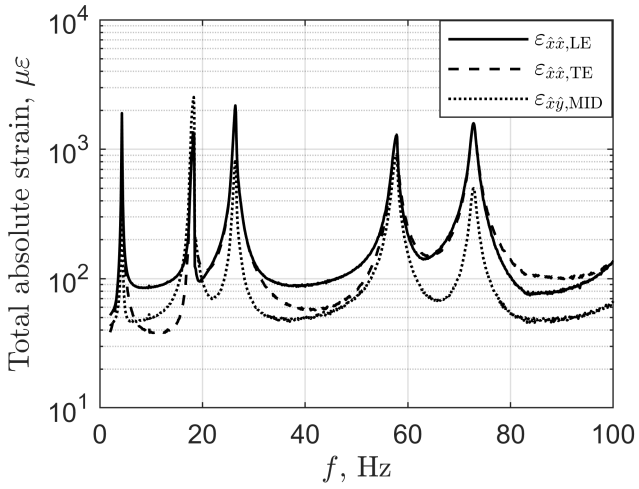

Figure 3.28: Total measured strain in the cantilever plate for the three fibers as a function of excitation frequency.

The experimental resonant frequencies are then determined by choosing the five frequencies at which the total strain in one of the fibers has a peak. The peaks for all fibers are located at the same frequencies.

The normalized strain shapes at the identified resonant frequencies are plotted in Fig. 3.29 in comparison to the FE strain for the first four modes (originally shown in Fig. 3.23).

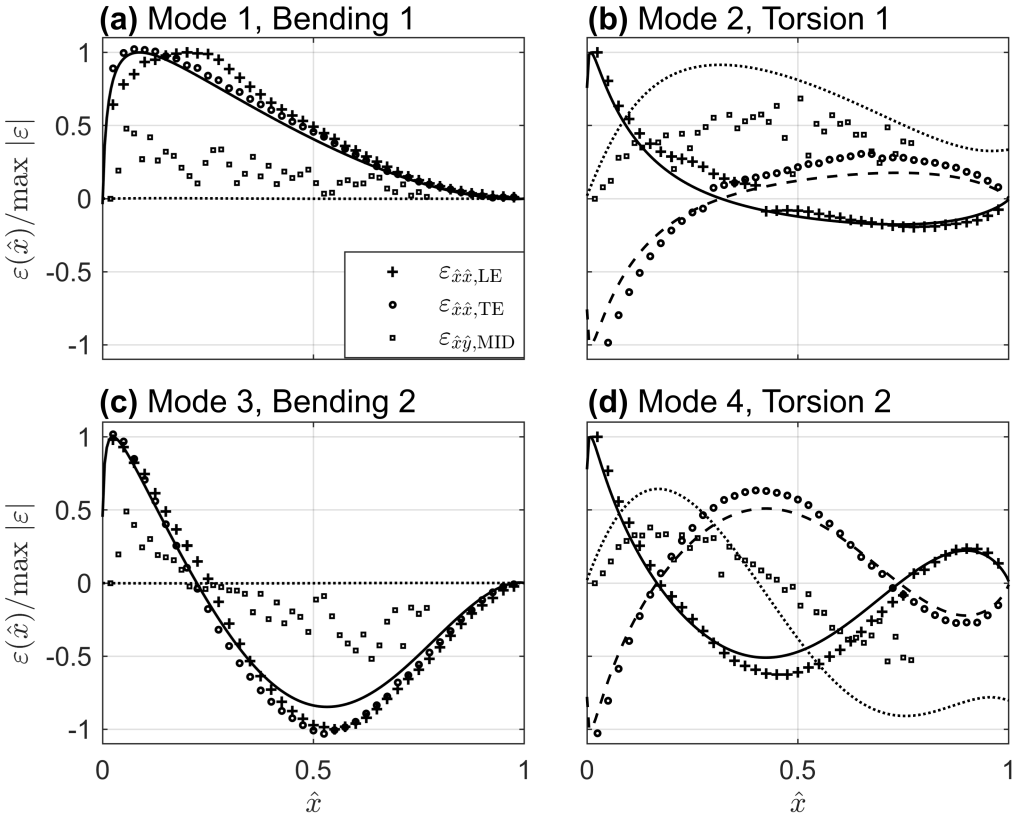

Figure 3.29: Measured strain distribution in three fibers at the first four resonant frequencies of a cantilever plate in comparison to FE results.

The bending fibers show relatively high correspondence with the strain distributions predicted through FE analysis for all four modes. The twist rate fiber, on the other hand, appears significantly more noisy. For the bending modes (modes 1 and 3), the twist rate fiber shows the same trends as the bending fibers – this is expected due to the normal strain contribution ($\varepsilon_{\hat{x}\hat{x}}$) to the 45-deg strain measurement ($\varepsilon_{\hat{x}'\hat{x}'}$) according to Eqn. 3.10. The relatively high measurement noise is likely due to bonding inaccuracies in the orientation of individual FBGs along the fiber. For the torsional modes (modes 2 and 4), the twist rate fiber generally follows the expected distribution based on FE analysis, but is still relatively noisy.

Due to the noisy twist rate measurements, the method of using the leading and trailing edge bending fibers to estimate the mode shape is used here. Based on this method, the bending fibers will be taken to approximate the bending of thin strips at their respective edges, and then a surface between the two used to describe the deflection at interior points of the plate. Since only two bending fibers are available, a linear relationship is used to describe the connection between the bending lines:

$$w(\hat{x}, \hat{y}) = \hat{y} \cdot w_{\mathrm{LE}}(\hat{x}) + (1 - \hat{y}) \cdot w_{\mathrm{TE}}(\hat{x}) \,, \tag{3.34}$$

where $w_{\mathrm{LE}}(\hat{x})$ and $w_{\mathrm{TE}}(\hat{x})$ are the bending deflections at the leading and trailing edges calculated using the integration matrix method describe above for beams. Comparisons between these calculated mode shapes and those based on FE analysis/products of beam functions are shown in Figs. 3.30 and 3.31.

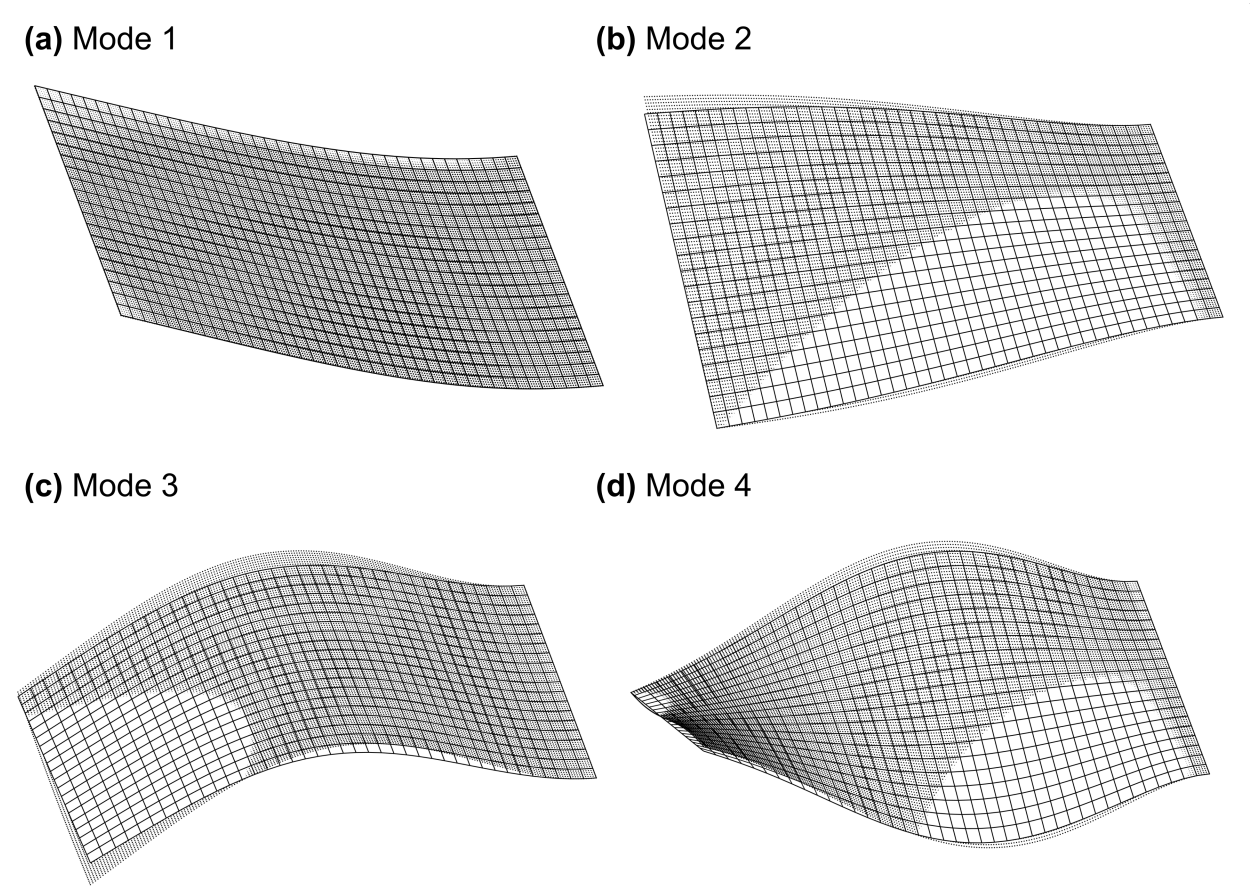

Figure 3.30: Comparison of cantilever plate mode shapes determined experimentally (grids) and by FE analysis (dots) for the first four modes.

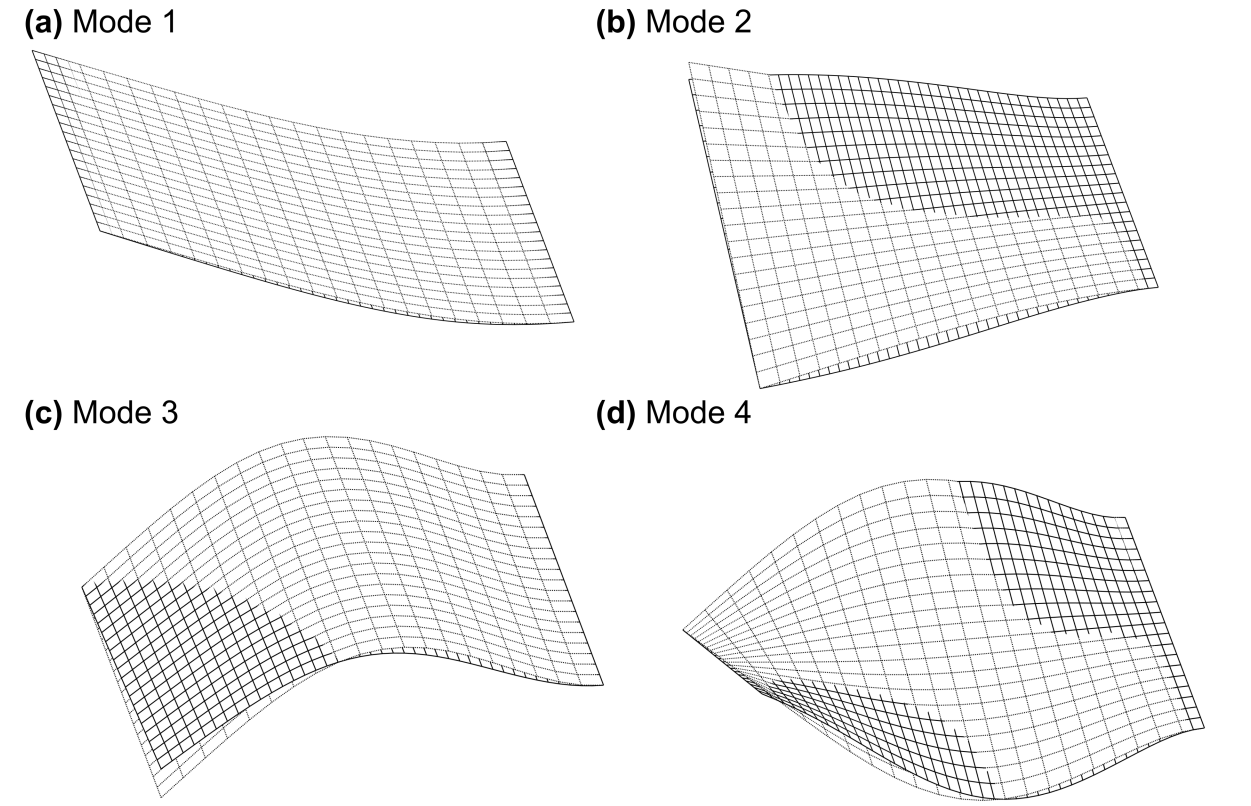

Figure 3.31: Comparison of cantilever plate mode shapes determined experimentally (solid grids) and by products of beam functions (dotted grids) for the first four modes.

Although there are noticeable differences between the FOSS estimated shapes and the numerical models, the FOSS integration method based on measured strain is relatively accurate in comparison. In addition to experimental uncertainties, a portion of these differences may be attributable to physical differences between the experiment and the analytical models (e.g. the effect of the shaker).

Resonant Frequency Comparison

In this section, the plate resonant frequencies deduced from experimental data are compared with the predictions based on the models described in Chapter 2.

Using the properties of the plate given in Table 3.5 and Eqns. 2.150 and 2.151, the analytical bending and torsional natural frequencies of the plate can be computed using the distributed parameter model. Alternatively, by Eqns. 2.148 and 2.152, the lumped parameter natural frequency predictions can be calculated. The torsional constant used in the results reported below is $J = 4416.943$ mm^4, which is based on evaluating 10 terms in the series given in Eqn. 2.95. If the approximate equation were used instead (Eqn. 2.94), the computed torsional constant is 4416.952 mm^4, which would yield predicted torsional natural frequencies approximately equal to those reported below.

The natural frequencies based on the lumped and distributed parameter models, FE analysis, frequency parameters from the Rayleigh-Ritz method, and those determined experimentally are summarized in Table 3.8.

Table 3.8: Comparison of theoretical and experimental resonant frequencies for the cantilever plate (Hz). Theoretical models do not include damping.

Method	Mode 1 (Bending 1)	Mode 2 (Torsion 1)	Mode 3 (Bending 2)	Mode 4 (Torsion 2)	Mode 5 (Bending 3)
Lumped Parameter	4.4	16.5	-	-	-
Distributed parameter, approximation	4.3	15.0	27.1	45.0	76.0
Rayleigh-Ritz, approximation	4.2	17.5	26.3	57.2	73.7
FE (CQUAD4)	4.2	17.4	26.1	57.1	73.3
Experimental	4.3	18.3	26.4	57.8	72.8

It is interesting to note that the analytical and FE natural frequency predictions for each of the beam and plate bending modes are all relatively close to one another (the maximum difference is less than 5%). For the torsional modes, however, the predictions vary significantly more (greater than 15%). The Rayleigh-Ritz method yields natural frequencies for

the torsional modes which are much closer to the FE model than the torsional distributed parameter model, which does not account for warping.

The experimental frequencies agree relatively well with the analytical predictions, and even more so with the numerical methods (Rayleigh-Ritz and FE). Damping, imperfect boundary conditions, and un-modeled contributions from the shaker/fiber bonds are all potential sources of differences between the experiments and the theoretical predictions.

3.5 Summary

In this chapter, a brief overview of fiber optic sensing is given, and a method for using distributed strain measurements to estimate the bending and twisting of beams and plates is described. Experimental results for the bending modes of a cantilever beam are analyzed and compared with theoretical models of the mode shapes and natural frequencies. These same comparisons are made for the first several bending and torsional modes of a cantilever plate. Based on these results, it is shown that distributed sensing using FOSS can be used to estimate the mode shapes of flexible structures and that these estimates compare quite well with analytical and numerical models.

CHAPTER 4
EXPERIMENTAL SYSTEM IDENTIFICATION IN THE PRESENCE OF WEAK NONLINEARITIES

4.1 Introduction

In this chapter, the concepts of modal analysis (Chapter 2) are applied to the dynamics of the cantilever beam previously analyzed (Chapter 3) to describe a general procedure for system identification in the presence of weak nonlinearities. A key contribution of this work is the empirical models which are developed to account for certain nonlinearities in the identified system. This chapter begins with a brief background for system identification and then proceeds with an in-depth analysis of a process to identify the parameters of a cantilever beam undergoing electromagnetic (shaker) or strain-induced (piezoelectric) actuation. This case study demonstrates the modal method of system identification and highlights the impact of the choice of experimental techniques on the identified parameters of a weakly nonlinear second order system.

4.2 Background

A brief overview of some key concepts related to system identification are reviewed in this section – many of these concepts are discussed in more detail in Appendix A.

The displacement frequency response of a second order system is a complex-valued function, where the modulus describes the amplitude of the frequency response and the angle describes its phase. The equations for these components are given by Eqn. A.31. Under harmonic excitation, the amplitude of the acceleration frequency response function (FRF) can be determined by multiplying the displacement FRF amplitude by ω^2, which corresponds to differentiating the displacement FRF twice. By Eqn. A.33, the normalized acceleration FRF amplitude can then be written $k\omega^2 \cdot |H(j\omega)|$. Defining the frequency ratio

$r = \omega/\omega_n$, a plot of the acceleration FRF amplitude is shown in Fig. 4.1.

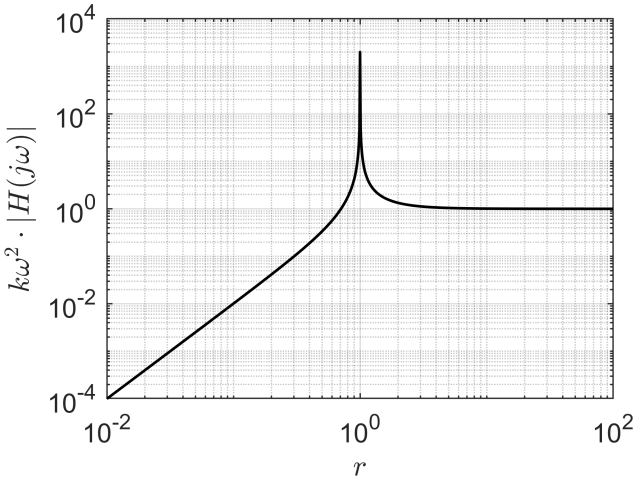

Figure 4.1: Normalized acceleration FRF amplitude versus frequency ratio, $r = \omega/\omega_n$, for a representative second order system.

At low frequency ratios, the acceleration response is low and increases at a constant rate per decade. Normalized responses less than 1 indicate attenuation of the input force. At resonance ($r \approx 1$), the normalized response increases rapidly to a peak somewhere near $r = 1$, where the input force is magnified. A brief discussion of the influence of damping on the frequency location and magnitude of this peak can be found in Appendix A. The response magnitude levels off to 1 for high frequency ratios, indicating that the input force is neither attenuated nor magnified. Based on experimental measurements of an FRF amplitude, the second order system parameters (mass, stiffness, and damping) can be estimated. Methods such as these are the focus of system identification procedures and are touched on in the following sections.

One complicating issue is if nonlinearities are present in the system under test. Consider Fig. 4.2, which is a detail view of the acceleration FRF magnitude in the region around

resonance.

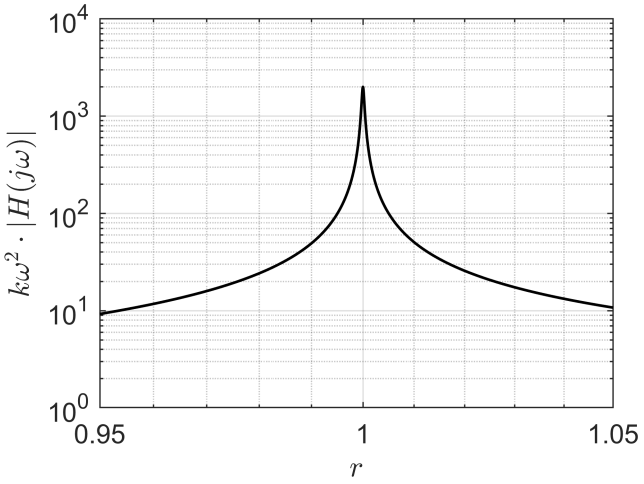

Figure 4.2: Normalized acceleration response versus frequency ratio, $r = \omega/\omega_n$, for a representative second order system in the region around resonance.

For the frequency ratios in this figure, the FRF magnitude is approximately symmetric about its peak. This is one characteristic of a linear system, and any deviation from this symmetry indicates the presence of a nonlinearity. In the results section to follow, a deviation known as softening will be shown to exist in the experimental response of a cantilever beam. In addition, system nonlinearities are demonstrated to lead to shifts in the resonance frequency and changes in the amplitude of the peak response. An empirical method to account for this type of nonlinear response is described in the remainder of this chapter.

4.3 Case Study: Cantilever Beam Modal Testing

In this section, an experimental system identification case study is presented to illustrate methods to estimate the system parameters of a second order model. The same cantilever beam which has been studied in Chapter 3 is analyzed in this section in the frequency

range around its first bending mode of vibration. First, static and dynamic experimental procedures for system identification of a single degree of freedom (SDOF) model of a cantilever beam are discussed. For the dynamic identification component, three experimental approaches are examined: (1) open loop, (2) constant input, and (3) constant response methodologies. Experimental results from the testing of a representative cantilever beam under electromagnetic and strain-induced excitation are then reported, and comparisons are made between the experimental methodologies for a range of excitation amplitudes.

4.3.1 Models Assumed for System Identification

This section describes a generalized system identification problem for a vibrating cantilever beam as an example of a common second order system. The transverse vibration of such a system can be described by Euler-Bernoulli beam theory with a partial differential equation in space and time. Alternatively, a lumped parameter model of the transverse vibration of the tip of the cantilever beam can be employed, which yields a second order ordinary differential equation in time.

The equation governing the transverse vibration of the tip of a cantilever beam serves as the model for the experimental system identification processes described in this chapter. The well-known model is given by Eqn. 4.1, where the parameters to be identified are the natural frequency ω_n, damping ratio ζ, and effective stiffness k_{eff} of the system.

$$\ddot{w}(t) + 2\zeta\omega_n\dot{w}(t) + \omega_n^2 w(t) = \frac{\underline{\omega}_n^2}{k_{\text{eff}}} F(t)\,. \tag{4.1}$$

The factor multiplying the force, $\frac{\underline{\omega}_n^2}{k_{\text{eff}}}$, is an equivalent way to write the normalization with respect to mass for a second order system. This form is more convenient for identifying a system where the stiffness and natural frequency are more readily identifiable. Here, the under bar on $\underline{\omega}$ indicates its value at a low amplitude force, i.e. the natural frequency of the system with minimal nonlinear effects, or the so-called baseline natural frequency. This

ratio can then define the effective mass, $m_{\text{eff}} = k_{\text{eff}}/\underline{\omega}_n^2$, for system identification. For an ideal linear system, $\underline{\omega}_n = \omega_n$ for all amplitudes of excitation.

To identify these system parameters, the steady-state system response and input force ($w(t)$ and $F(t)$) can be measured for a pure harmonic frequency sweep (i.e. sine sweep) of the input. The excitation of the system is often accomplished by an electromagnetic shaker, and the concentrated input force to the system can be measured directly using a load cell positioned at the connection between the shaker and the system under test. The response can be measured using various transducers such as an accelerometer, a laser Doppler velocity transducer (i.e. vibrometer), or a laser displacement sensor. When available, contactless transducers are preferred to avoid altering the dynamics of the system that is being examined.

A common alternative to concentrated (i.e. single point) excitation is strain-induced (distributed) excitation with a piezoelectric material actuator. In this case, the distributed input force is difficult to measure directly, and the model to be identified is instead given by Eqn. 4.2, where the parameters to be identified are the same as the previous model except for the forcing term. This model is described in Appendix C. The factor g is a coefficient which multiplies the input voltage V to yield an equivalent input force, and γ is the coupling correction to account for unmodeled characteristics that are specific to an actuator and which are not of interest. In this form, the only additional parameter to be estimated is the coupling correction γ.

$$\ddot{w}(t) + 2\zeta\omega_n\dot{w}(t) + \omega_n^2 w(t) = \left(\frac{\underline{\omega}_n^2}{k_{\text{eff}}}\right)\gamma g \cdot V(t)\,. \tag{4.2}$$

The model can be identified through measurements of the steady-state system response and input voltage ($w(t)$ and $V(t)$) in a frequency sweep of the input excitation. A summary of the parameters to be identified for both excitation methods is given in Table 4.1.

Table 4.1: Model parameters for system identification.

Actuation Method	Model	Required Parameters
Electromagnetic (Shaker)	Eqn. 4.1	Effective stiffness (k_{eff})
		Natural frequency (ω_n)
		Damping ratio (ζ)
Strain-induced (Piezoelectric)	Eqn. 4.2	Effective stiffness (k_{eff})
		Natural frequency (ω_n)
		Damping ratio (ζ)
		Coupling correction (γ)

These parameters will be estimated using the testing procedures outlined in the following sections. First, static testing will be used to deduce the effective stiffness of a cantilever beam. Next, dynamic testing will be used to deduce three model parameters: natural frequency, damping ratio, and coupling correction.

4.3.2 Static Testing for Effective Stiffness

In this section, the properties of the beam specimen and test setup are first presented. Next, the procedure to identify the system's static stiffness is described. Finally, static load and deflection results are used to determine the system's effective stiffness.

Specimens and Setup

A slender aluminum beam with rectangular cross-section is used as the base structure for all experiments presented in this chapter, including the dynamic testing presented later. Properties of the baseline beam specimen are the same as those for the beam tested in Chapter 3 and given in Table 3.1. The density of the beam is calculated based on the total volume and total mass of a blank beam specimen, which is then used to determine the mass

of the cantilevered (free) section of the beam.

The experimental setup used for static testing is shown in Fig. 4.3. The beam is clamped on a support structure, and this clamped boundary condition is maintained throughout all experiments.

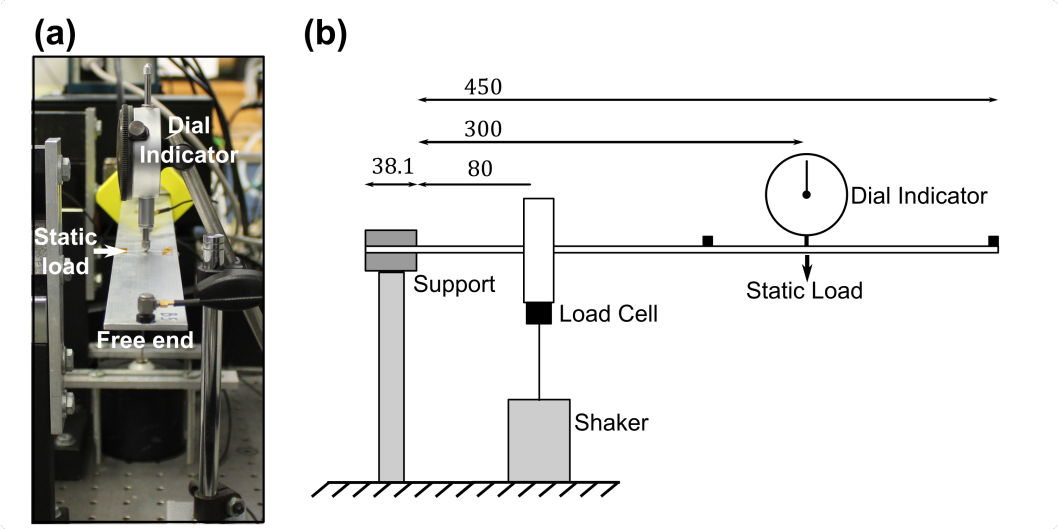

Figure 4.3: Static experimental setup. (a) End view of the beam. (b) Illustration with critical components. Dimensions are listed in mm

To determine the system's stiffness, a series of static loads are applied to the cantilever beam through a hanger located at 300 mm from the clamped end. An analog displacement dial indicator, collocated at the same position as the load, is used to measure the displacement of the beam. Note that although a shaker is not needed for this test, it is kept as a part of the setup to maintain consistency between the static and dynamic experiments. Its stiffness contribution is accounted for as described in the next section.

Identification Procedure

From Eqn. 4.1, if the system is static (i.e. $\ddot{w} = \dot{w} = 0$ and $\omega_n^2 = \underline{\omega}_n^2$) then the apparent system stiffness can be determined by $k_{\text{total}} = F/w$, where w is the tip displacement for an applied tip force F. In practice, loading the beam and measuring the displacement exactly at the beam tip can be difficult. Alternatively, the effective stiffness can be measured by loading the beam at a convenient position l_0, and calculating the stiffness for a beam with that length. The loading position can be normalized with respect to the beam length, $\tilde{l} = l_0/l \in (0, 1)$, where lengths with a tilde are normalized by the beam length. For the static testing setup in this chapter, the normalized loading position is $\tilde{l} = 300/450$. The stiffness is then given by:

$$k_{\text{total}}(\tilde{l}) = \frac{F}{w(\tilde{l})}\,. \tag{4.3}$$

Since the total stiffness of the system shown in Fig. 4.3 includes the shaker's axial stiffness in addition to the beams effective stiffness, the contribution of the shaker to the total stiffness must be considered. For a given shaker axial stiffness, by Eqn. D.11, the effective stiffness of the shaker for motion at the beam tip is given by Eqn. 4.4,

$$k_{\text{eff,shaker}}(\tilde{l}) = \frac{3EI_y}{l^3}\left(\frac{k_{\text{shaker}}\alpha^4(3-\alpha)^2}{4\left(\frac{3EI}{l^3}\right) + k_{\text{shaker}}\alpha^3(1-\alpha)^2(4-\alpha)}\right)\,, \tag{4.4}$$

where I_y is the second moment of area of the cross section with respect to the y-axis and $\alpha = \tilde{x}_{\text{shaker}}/\tilde{x}$ is the normalized position of the shaker in reference to the position at which the static load is applied. For the current setup, the normalized shaker position is $\alpha = 80/300$. Furthermore, the shaker device used is a Type 4810 Mini Shaker manufactured by Bruel & Kjaer, which has an axial stiffness of $k_{\text{shaker}} = 2000$ N/m as reported by the manufacturer [52].

The beam's contribution to this total stiffness ($k_{\text{eff}}(\tilde{l})$) is then given by:

$$k_{\text{eff}}(\tilde{l}) = k_{\text{total}}(\tilde{l}) - k_{\text{eff,shaker}}(\tilde{l})\,. \tag{4.5}$$

With constant elastic modulus and area moment of inertia throughout the beam's longitudinal domain, the effective stiffness of the entire beam can then be found:

$$k_{\text{eff}} = \left(\frac{k_{\text{eff}}}{k_{\text{eff}}(\tilde{l})} \right) k_{\text{eff}}(\tilde{l}) = \frac{l_0^3}{l^3} k_{\text{eff}}(\tilde{l}) = \tilde{l}^3 k_{\text{eff}}(\tilde{l}) \,. \tag{4.6}$$

This result is based on the equation for a cantilever beam's effective stiffness:

$$k_{\text{eff}} = \frac{3EI_y}{l^3} \,. \tag{4.7}$$

By measuring the resulting displacement for several loads within the linear elastic region, the slope coefficient for a linear model will yield the estimated stiffness. Empirical estimation of the effective stiffness of the system under test will provide the baseline stiffness parameter.

Results and Analysis

The static force as a function of deflection for loading and unloading of the beam is shown in Fig. 4.4.

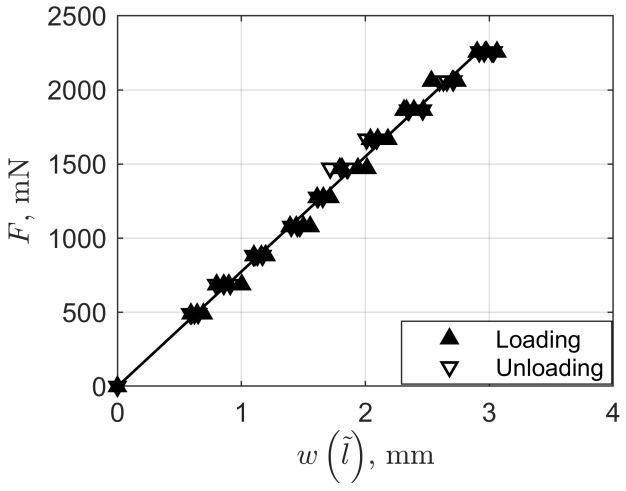

Figure 4.4: Applied static force (F) as a function of beam deflection ($w(\tilde{l})$) during beam stiffness testing.

Four cycles of loading (up arrows) and unloading (down arrows) are presented. For each cycle, the beam is incrementally loaded using a hanger and slotted weights up to a maximum of 230 g, and then incrementally unloaded to its original configuration.

Here, and for all parameters in this chapter, a hat over a parameter indicates an empirical estimate. The process to estimate the effective beam stiffness is:

1. Estimate the total stiffness for the shortened beam ($\hat{k}_{\text{total}}(\tilde{l})$) using a linear model to determine the proportionality constant between the force and deflection data.

2. Compute the effective stiffness for a shaker acting at the tip of the shortened beam ($k_{\text{eff,shaker}}(\tilde{l})$) based on the known shaker flexural stiffness (k_{shaker}), normalized location (α), and Eqn. 4.4.

3. Compute the estimated effective beam stiffness for the shortened beam ($\hat{k}_{\text{eff}}(\tilde{l})$) using Eqn. 4.5.

4. Compute the estimated effective beam stiffness for the complete beam length ($\hat{k}_{\text{eff}}$) using Eqn. 4.6.

The results of these steps are summarized in Table 4.2. As expected, the experimental stiffness is lower than the theoretical prediction due to various assumptions such as perfect clamped boundary condition and the set of Euler-Bernoulli beam assumptions. The difference between the theoretical and experimental stiffness values is relatively low, although even small differences will result in large errors in the prediction of response amplitude near resonance for lightly damped second order systems.

Table 4.2: Static stiffness testing results and comparison.

Parameter	Analytical (N/m)	Experimental (N/m)	$\Delta = \frac{\hat{k}_{\text{eff}} - k_{\text{eff,analytical}}}{k_{\text{eff,analytical}}}$
Total system stiffness, shortened ($\hat{k}_{\text{total}}(\tilde{l})$)	-	775	-
Shaker effective stiffness, shortened ($k_{\text{eff,shaker}}(\tilde{l})$)	-	18.4	-
Beam effective stiffness, shortened ($\hat{k}_{\text{eff}}(\tilde{l})$)	-	757	-
Beam effective stiffness, ($\hat{k}_{\text{eff}}$)	236	224	-5.0%

4.3.3 Dynamic Testing for Complete Identification

In this section, the excitation methods and experimental setup for dynamic testing are described first. A procedure to identify the system parameters of the equations of motion for electromagnetic actuation (Eqn. 4.1) and for strain-induced actuation (Eqn. 4.2) is then presented. Next, experimental results for electromagnetic and strain-induced actuation methods are reported. This section concludes with an analysis of the experimental data and the variation in identified system parameters.

Excitation Methods

The parameters to be estimated are ω_n and ζ for shaker actuation and ω_n, ζ, and γ for strain-induced actuation. For both actuation types, pure harmonic (i.e. sine) frequency sweeps are conducted, and the measurements used to identify a constant parameter model for each experimental frequency response function (FRF). To demonstrate and characterize inherent nonlinearities in the system response, these frequency sweeps are conducted at various amplitudes of excitation as well as under different testing procedures.

For electromagnetic actuation, the FRFs for several different testing procedures are developed for both increasing and decreasing frequency sweeps. These testing procedures are:

1. Open loop (OLP): Constant amplitude voltage excitation of the shaker/piezoelectric device.

2. Constant response type 1 via closed loop control (CLPACC): Variable amplitude voltage excitation of the shaker/piezoelectric device such that constant amplitude response is measured at the tip accelerometer.

3. Constant response type 2 via closed loop control (CLPVEL): Variable amplitude voltage excitation of the shaker/piezoelectric device such that constant amplitude response is measured at the laser velocity transducer.

4. Constant input via closed loop control (CLPFRC): Variable amplitude voltage excitation of the shaker/piezoelectric device such that constant amplitude input force is measured at the load cell.

For the constant response and input test methods, a closed loop (CLP) Proportional-Integral-Derivative (PID) controller is implemented in National Instruments LabVIEW [53] graphical software platform. In these closed loop experiments, the control voltage to the actuator is varied throughout the frequency sweep such that the amplitude of the controlled

signal is maintained constant. For each of these testing methods, five amplitude levels are tested, and 10 cycles of response are acquired at each frequency. The minimum amplitudes are established through trial and error by determining the minimum command amplitude that yields signals above the noise floor for all sensors throughout the frequency sweep. The higher amplitude levels are then determined by fixed step increments up to a specified maximum amplitude. The increasing and decreasing frequency sweep data are averaged due to minimal observed hysteresis, and the signal standard deviations are reported for each frequency. For the strain-induced actuation experiments, only the first three testing procedures described above are conducted as the input force cannot be measured for the constant input test method. A summary of the testing methods is given in Table 4.3.

Table 4.3: Summary of dynamic testing procedures.

Actuation Method	Testing Procedure	Controlled Signal
Electromagnetic	Open Loop (OLP)	Voltage (Input to Shaker)
(Shaker)	Constant Response 1 (CLPACC)	Acceleration (Tip)
	Constant Response 2 (CLPVEL)	Velocity (Mid-Span)
	Constant Input (CLPFRC)	Force (Load Cell)
Strain-Induced	Open Loop (OLP)	Voltage (Input to Piezoelectric Device)
(Piezoelectric)	Constant Response 1 (CLPACC)	Acceleration (Tip)
	Constant Response 2 (CLPVEL)	Velocity (Mid-Span)

Specimens and Setup

Two beam specimens are tested, one under electromagnetic actuation and the other under strain-induced actuation. The properties of the beam specimens tested dynamically are the same as those specified for the static tests presented in Table 3.1. For electromagnetic actuation, a shaker is positioned at 80 mm from the beam root. The shaker is used to excite the beam through a sting, load cell, and a roller-clamp bracket. For strain-induced actua-

tion, a piezocomposite beam is fabricated by bonding a commercially available piezoelectric device to the upper surface of the beam. The piezoelectric device used for this specimen is the M2814-P2 type Macro-Fiber Composite (MFC) manufactured by the Smart Material Corporation [54]. This device operates as an actuator in the *31* mode of piezoelectricity. The properties of the MFC as well as details of its bonding location are given in Table 4.4.

Table 4.4: Properties of the M2814-P2 type Macro-Fiber Composite actuator.

Parameter	Value	Source
Length (l_p)	28 mm	Measured
Width (b_p)	14 mm	Measured
Height (h_p)	0.18 mm	Measured
Coupling coefficient (d_{31})	-170 pm/V	Vendor [54]
Capacitance (C_p)	30.8 nF	Vendor [54]
Elastic modulus (E_p^E)	30.3 GPa	Vendor [54]
Start bond from root (x_{1p})	13.7 mm	Measured
End bond from root (x_{2p})	41.7 mm	Measured
Electromechanical coupling factor (g)	48.5 mN/V	Deduced

The coupling factor for the first mode of vibration (g) is determined by substituting the beam geometry, material properties, and start and end locations of the piezoelectric actuator in Eqn. C.11.

The experimental set ups are shown in Fig. 4.5. The beams are clamped on a support structure and this clamped boundary condition is maintained throughout all experiments.

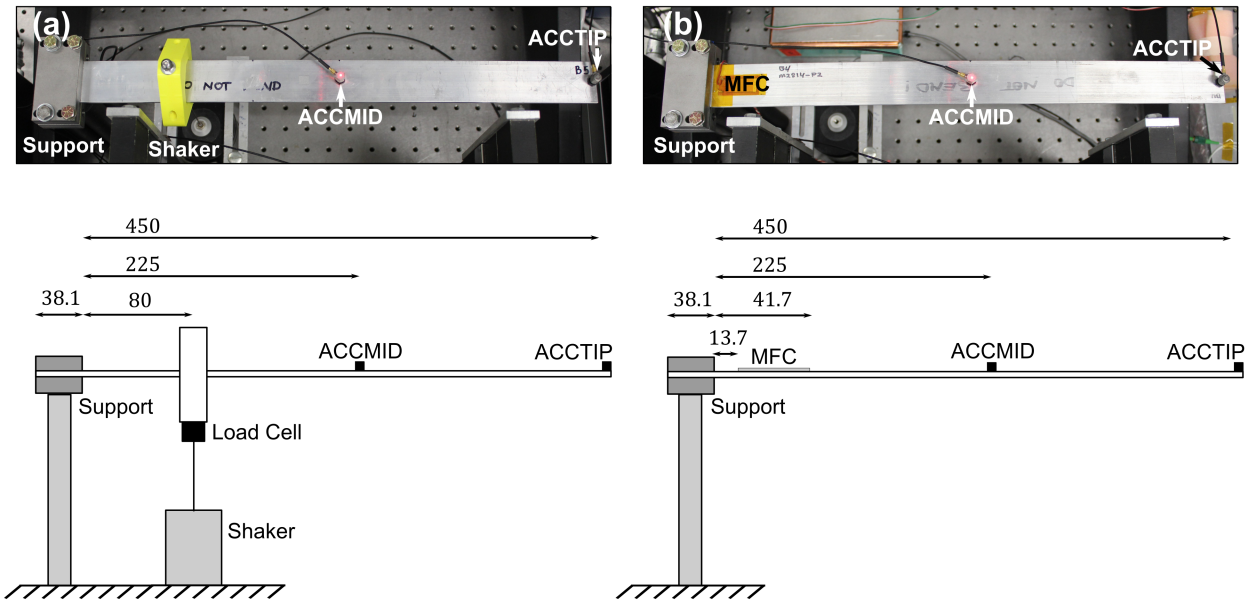

Figure 4.5: Dynamic experimental setup. (a) Electromagnetic actuation. (b) Strain-induced actuation. Dimensions are listed in mm.

Two accelerometers are glued to each beam: one at the mid-span location (labeled ACCMID) and the other near the tip of the beam (labeled ACCTIP). A laser velocity transducer is positioned directly above the mid-span accelerometer. The signal flow diagrams are shown in Fig. 4.6.

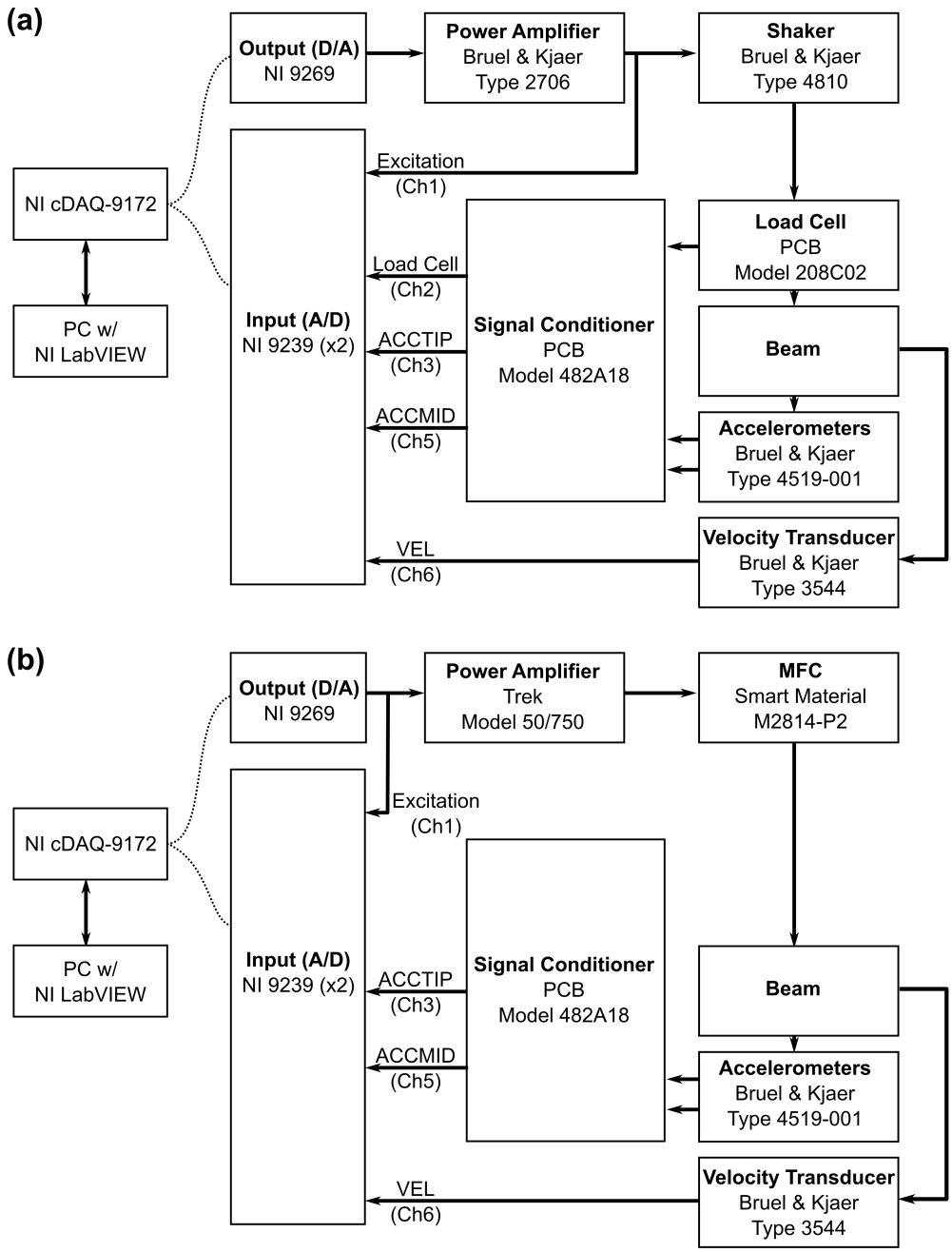

Figure 4.6: Signal flow diagrams. (a) Electromagnetic actuation. (b) Strain-induced actuation.

Identification Procedure

The empirical FRF magnitude for each test summarized in Table 4.3 is determined by the ratio of the tip acceleration (ACCTIP) to the input force for electromagnetic actuation, and to the input voltage for strain-induced actuation. From the calculated FRF, the system's natural frequency at low excitation amplitude ($\underline{\omega}_n$) is estimated, and the effective mass is determined using the static effective stiffness ($\underline{m}_{\text{eff}} = k_{\text{eff}}/\underline{\omega}_n^2$). For the electromagnetic actuation cases, where the input force could be directly measured, the amplitude of the empirical accelerance FRF is assumed to be modeled by the constant parameter frequency domain representation of a second order system given in Eqn. 4.8,

$$\frac{\ddot{w}_{\text{std}}}{F_{\text{std}}} = \left| \frac{s^2 W(s)}{F(s)} \right| = \left| \frac{1}{\underline{m}_{\text{eff}}} \left(\frac{s^2}{s^2 + 2\zeta\omega_n s + \omega_n^2} \right) \right| , \tag{4.8}$$

where the double over-dot ($\ddot{}$) indicates differentiation with respect to time and the subscript "std" indicates that the standard deviation of the harmonic signal is used in the calculations. In addition, for the steady state harmonic response considered in this chapter, the complex variable is defined as $s = j\omega$. Next, during the residual minimization routine described below, the damping ratio (ζ) and natural frequency (ω_n) are estimated to minimize the sum of squared residuals between the empirical FRF and this assumed model.

As mentioned before, the input force for strain-induced actuation cannot be directly measured. Instead, the input voltage is measured and the coupling correction as given in Eqn. 4.2 is used. Specifically, the amplitude of the empirical FRF is assumed to be modeled by Eqn. 4.9,

$$\frac{\ddot{w}_{\text{std}}}{V_{\text{std}}} = \left| \frac{s^2 W(s)}{V(s)} \right| = \left| \frac{\gamma g}{\underline{m}_{\text{eff}}} \left(\frac{s^2}{s^2 + 2\zeta\omega_n s + \omega_n^2} \right) \right| , \tag{4.9}$$

where the damping ratio (ζ), natural frequency (ω_n), and coupling correction (γ) are estimated to minimize the sum of squared residuals between the empirical FRF and this assumed model.

The residual minimization routine is implemented in MATLAB [55] using the system's state space representation, where, taking $x_1 = w$ and $x_2 = \dot{w}$, the SDOF equation of motion given in Eqn. 4.1 can be written as a system of equations in state space form:

$$\begin{bmatrix} \dot{x}_1 \\ \dot{x}_2 \end{bmatrix} = \begin{bmatrix} 0 & 1 \\ -\omega_n^2 & -2\zeta\omega_n \end{bmatrix} \begin{bmatrix} x_1 \\ x_2 \end{bmatrix} + \begin{bmatrix} 0 \\ \frac{1}{m_{\text{eff}}} \end{bmatrix} F\,. \tag{4.10}$$

The amplitude of the acceleration frequency response of this system is then determined for specified system parameters. Next, the sum of squared residuals between this model and an experimental FRF are computed and the constant parameters ω_n and ζ estimated which minimize that metric. For the strain-induced tests, the additional parameter γ is estimated simultaneously during the residual minimization routine by scaling the acceleration response of the model.

In addition to the residual minimization routine described above, it is worth mentioning that other more conventional methods can be used for estimating the parameters of second order systems. These include estimating the natural frequency based on peak picking or quadrature, and estimating the damping ratio based on the half power method. The peak picking estimate is simply the frequency associated with the maximum amplitude response, which for lightly damped systems corresponds closely with the undamped natural frequency. Quadrature estimation involves determining the frequency at which the phase of the acceleration response to input force crosses 270-deg, which for lightly damped systems corresponds to the natural frequency of the system. Finally, the half power damping method is based on determining the half power frequency points ω_1 and ω_2 and applying the approximate equation $\zeta = \frac{\omega_2 - \omega_1}{2\omega_n}$. The natural frequency and damping ratio estimates based on these methods are reported in Appendix F alongside the parameter estimates based on the residual minimization routine.

Results: Electromagnetic Actuation

The standard deviation of the acceleration and input force signals for the electromagnetic actuation tests are shown in Fig. 4.7. For each test procedure, the five command amplitude levels can be seen. As mentioned before, frequency dependent hysteresis is observed to be negligible for all experiments, so each frequency sweep is an average of increasing and decreasing frequency sweeps.

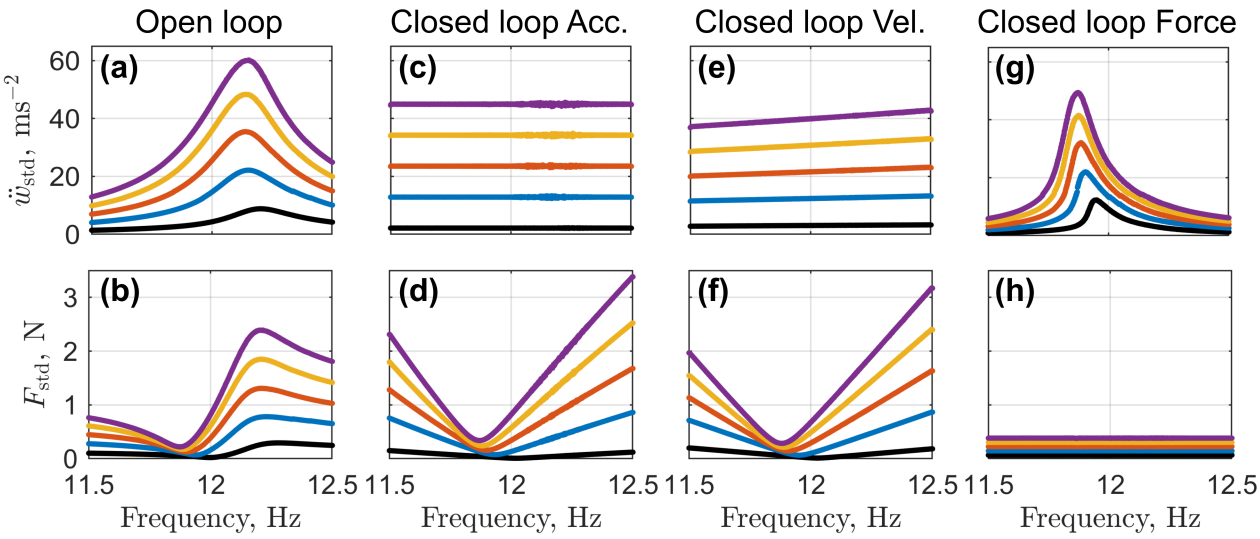

Figure 4.7: Standard deviation of acceleration ($\ddot{w}$) and force (F) versus excitation frequency for electromagnetic actuation tests.

The corresponding FRF amplitude and phase diagrams are plotted in Fig. 4.8.

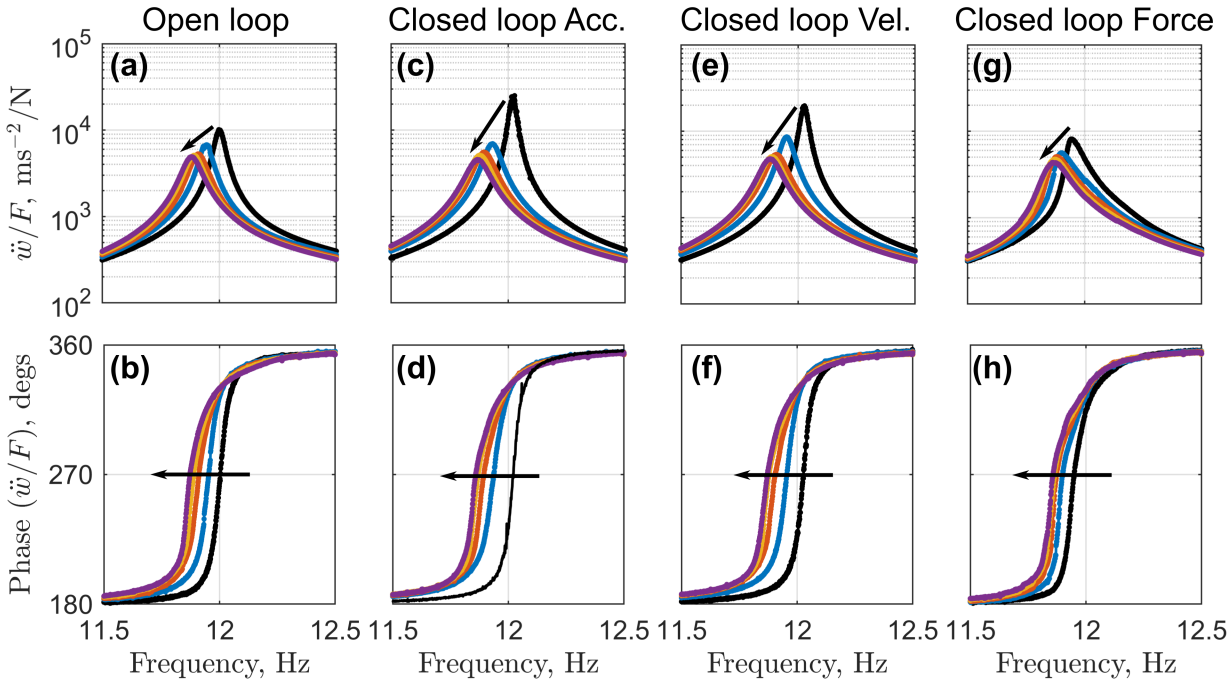

Figure 4.8: Tip acceleration to input force ($\ddot{w}/F$) FRFs for electromagnetic actuation tests as excitation amplitude is increased. Arrows point in the direction of increasing command amplitude.

As the command amplitude level increases, the FRFs for all the testing procedures exhibit decreases in the resonant frequencies and increases in the damping ratios. For the constant input, or closed loop force tests, "softening" is also present as seen in Fig. 4.8(g) by the tilting in the FRF amplitude plots towards lower frequencies. All test results indicate the presence of various levels of weak nonlinearities whose character appears to depend on the testing procedure that is implemented.

Results: Strain-induced Actuation

The standard deviation data of the acceleration and input force signals for the strain-induced actuation tests are shown in Fig. 4.9. For each test procedure, the five command amplitude levels can be seen.

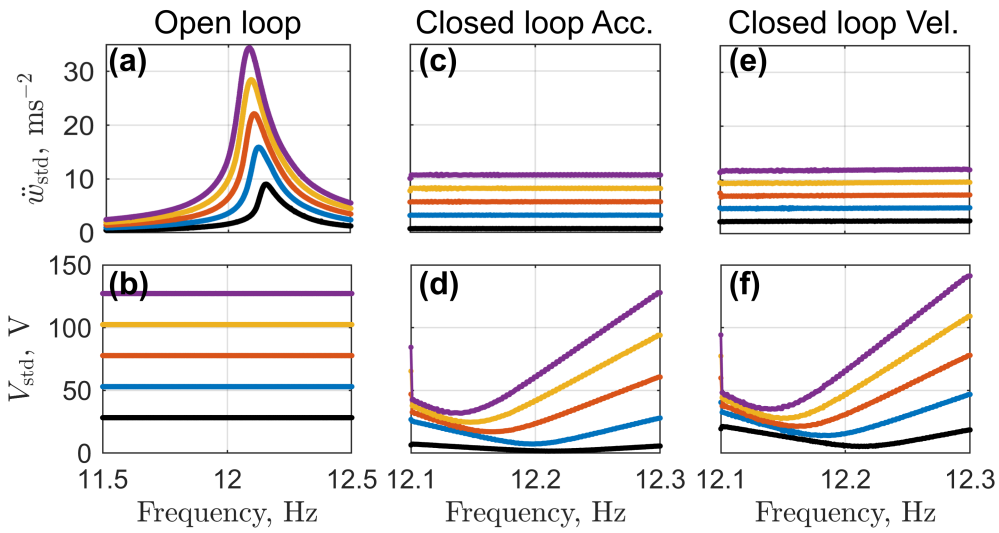

Figure 4.9: Standard deviation of acceleration ($\ddot{w}$) and voltage (V) versus excitation frequency for strain-induced actuation tests.

The corresponding FRF amplitude and phase diagrams are plotted in Fig. 4.10.

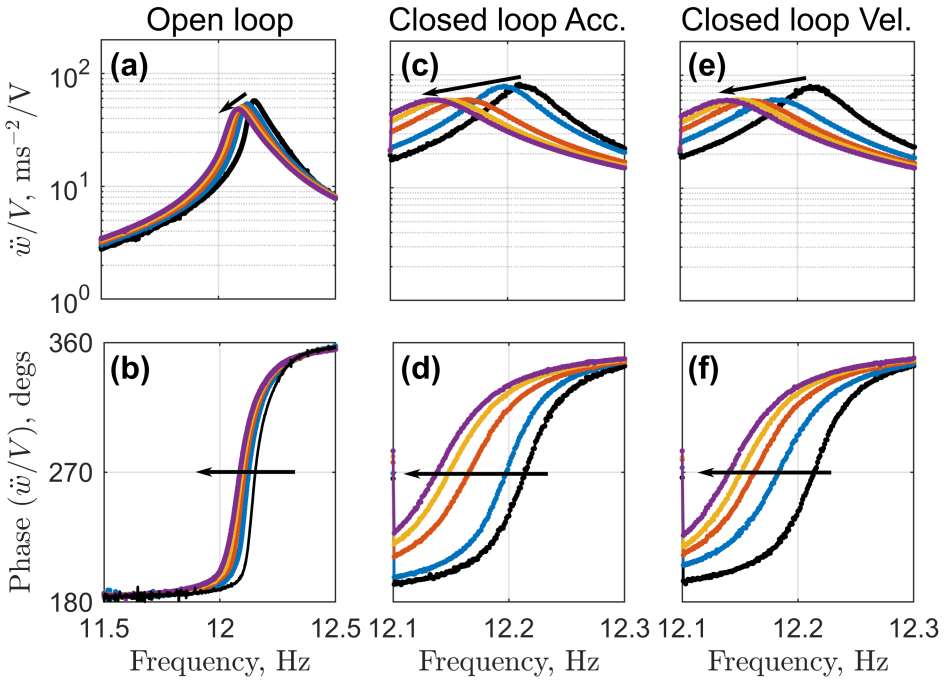

Figure 4.10: Tip acceleration to input voltage ($\ddot{w}/V$) FRFs for strain-induced actuation tests as excitation amplitude is increased. Arrows point in the direction of increasing command amplitude.

As the command amplitude increases, the FRFs for all the testing procedures exhibit decreases in the resonant frequencies and increases in the damping ratios just as for electromagnetic actuation. For the open loop, or constant voltage tests, softening is also present as seen in Fig. 4.10(a) by the tilting in the FRF amplitude plots towards lower frequencies. Similar to electromagnetic actuation, the impact of nonlinearities can be seen for all testing procedures.

Analysis

The identified constant parameter models based on the residual minimization routine for the electromagnetic actuation tests are shown in Fig. 4.11.

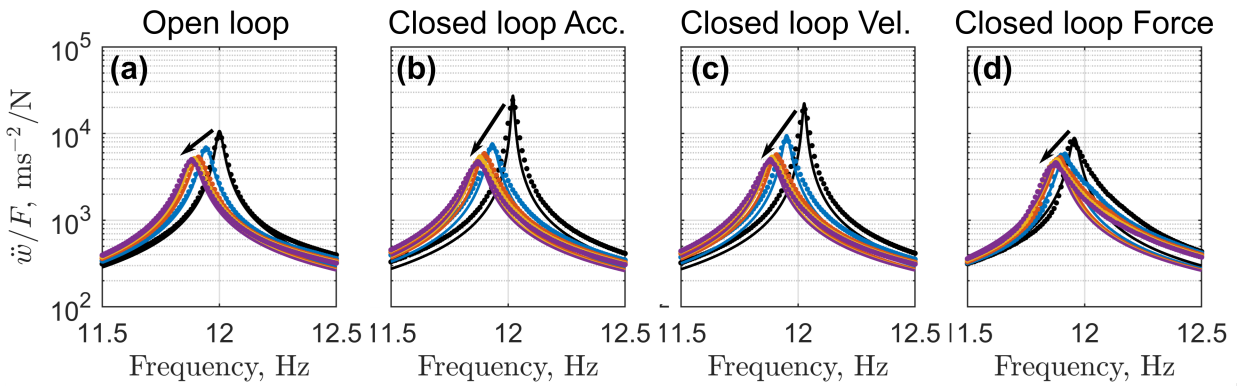

Figure 4.11: Identified constant parameter models of tip acceleration to input force ($\ddot{w}/F$) FRF amplitudes for electromagnetic actuation tests. Arrows point in the direction of increasing command amplitude.

For clarity, only every tenth experimental datum point for each command amplitude is shown in each plot. The identified SDOF models demonstrate close agreement with the empirical FRFs for all but the closed loop force test cases where the softening behavior causes divergence from the identified second order model, as shown in Fig. 4.11(d). In particular, the open loop case (Fig. 4.11(a)) shows excellent agreement throughout the frequency domain, while the experimental FRFs in the closed loop response cases (Fig. 4.11(b) and (c)) diverge slightly from the identified constant parameter model away from resonance.

The identified constant parameter models based on the residual minimization routine for the strain-induced actuation tests are shown in Fig. 4.12.

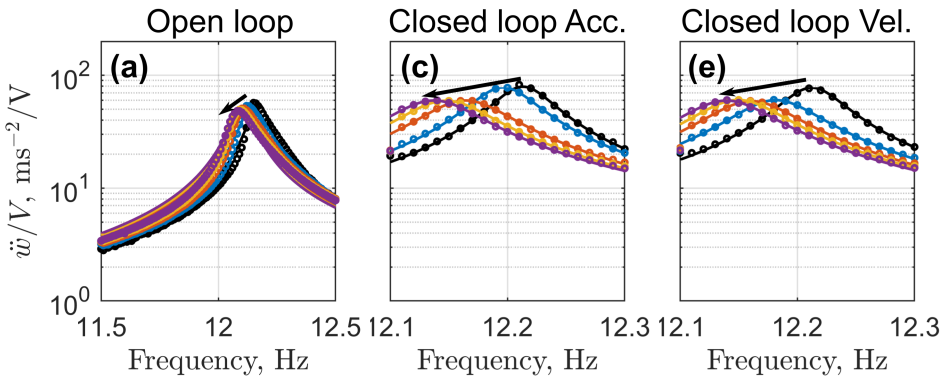

Figure 4.12: Identified constant parameter models of tip acceleration to input voltage ($\ddot{w}/V$) FRF amplitudes for strain-induced actuation tests. Arrows point in the direction of increasing command amplitude.

As in the previous figure, only every tenth experimental datum point for each command amplitude is shown in each plot for clarity. The identified SDOF models demonstrate close agreement with the empirical FRFs for the constant response test cases (Fig. 4.12(b) and (c)), but again cannot account for the softening behavior of the experimental FRF for the open loop test cases (Fig. 4.12(a)).

The identified constant parameters for each test case are determined ($\hat{\omega}_n$ and $\hat{\zeta}$ for every test, as well as $\hat{\gamma}$ for the strain-induced actuation tests) based on the SDOF residual minimization routine, where parameters with a hat indicate estimated parameters. For all the experimental cases, the estimated squared natural frequency ($\hat{\omega}_n^2$) versus the equivalent force acting at the beam tip are plotted in Fig. 4.13.

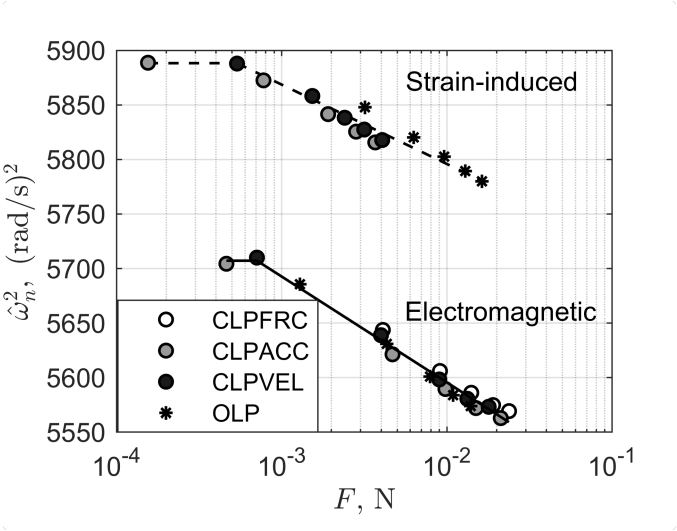

Figure 4.13: Estimated squared natural frequency ($\hat{\omega}_n^2$) versus logarithmic-scaled force (F).

Empirical piecewise-continuous variable parameter models are also plotted here, where the initial constant (horizontal) components represent the low force amplitude regions. This value is the baseline squared natural frequency, $\underline{\hat{\omega}}_n^2$, and is determined for each actuation type. The monotonically decreasing lines represent identified empirical relationship between $\hat{\omega}_n^2$ and the force amplitude. For each actuation type, the natural frequency at low excitation amplitude, $\underline{\hat{\omega}}_n$, is determined by taking the average of the two smallest force amplitude cases. For the higher excitation amplitudes, a logarithmic equation, given by Eqn. 4.11 is used to model the parameter variation.

$$\hat{\omega}_n^2 = C_{\omega_n} \cdot \ln \frac{F}{\underline{F}} + \underline{\hat{\omega}}_n^2 \,. \tag{4.11}$$

In this model, C_{ω_n} is the slope of the proportional relationship. The low excitation force, $\underline{F}$, is the force corresponding to the initial point of the estimated logarithmic model, which corresponds to the second smallest force amplitude here. The parameters of the identified models are summarized in Table 4.5.

Table 4.5: Functional dependency of squared natural frequency ($\hat{\omega}_n^2$) on excitation force (F).

Actuation Method	C_{ω_n}	$\underline{F}$	$\underline{\hat{\omega}_n^2}$	R^2_{adj}
Electromagnetic	-42.2	7.08×10^{-4}	5710	0.978
Strain-induced	-31.6	5.37×10^{-4}	5890	0.935

Although the material and geometric properties of the beam specimens are the same for both actuation types, the constant offset between the empirical natural frequencies of the electromagnetic and strain-induced tests is mainly a result of the contribution of the shaker in the electromagnetically excited system. For both actuation types, the corresponding variable parameter models demonstrate good agreement with the data. An additional notable observation is that the constant response cases (CLPACC and CLPVEL) are able to achieve the lowest excitation force at resonance while staying above the noise floor of the sensors for both excitation methods. Since system nonlinearities increase as the excitation amplitude increases, being able to achieve such low excitation force is important in estimating the baseline model with minimal nonlinear effects.

The estimated damping ratio is plotted versus the input excitation force in Fig. 4.14.

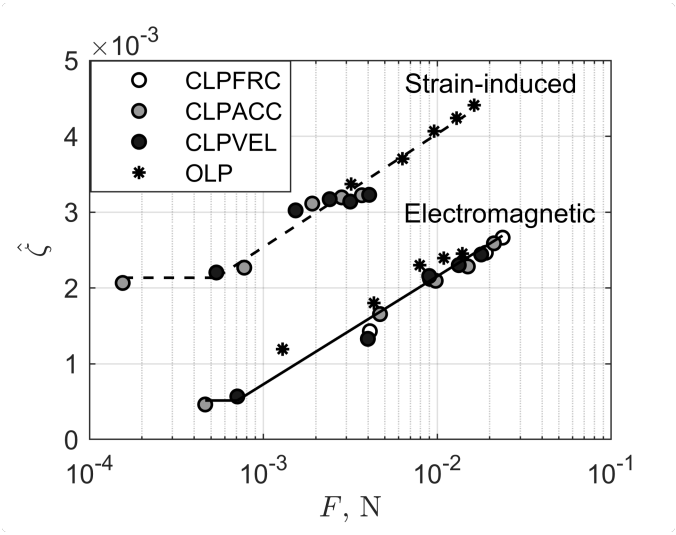

Figure 4.14: Estimated damping ratio ($\hat{\zeta}$) versus logarithmic-scaled force (F).

From these two plots, it can be seen that the strain-induced actuation tests show a higher natural frequency and a higher damping ratio for a given force in comparison to the electromagnetic actuation tests. With estimated damping ratios in this range ($\hat{\zeta} < 0.005$), the percent difference between the undamped and damped natural frequencies is very low:

$$\%\Delta\omega = \left(\frac{\omega_n}{\omega_d} - 1\right) \times 100 = \left(\frac{1}{\sqrt{1-\zeta^2}} - 1\right) \times 100 \approx 0.0013\%\,, \tag{4.12}$$

where $\omega_d = \omega_n\sqrt{1-\zeta^2}$. Since these systems are so lightly damped, the peak picking, quadrature, and SDOF residual minimization routine all yield natural frequencies in close agreement, as reported in the first three columns of Appendix F. In addition, for such lightly damped systems, the natural frequency does not vary significantly with changes in damping as discussed in Appendix A. The main effect of damping, then, is on the variation in the response amplitude near resonance.

As for the squared natural frequency data, piecewise linear empirical models are plotted in Fig. 4.14, where the horizontal segments represent the low force (baseline) amplitude values

of $\underline{\zeta}$. These values are determined by taking the mean of the two smallest force amplitude cases. Defining as before the low amplitude force, $\underline{F}$, a logarithmic model given by Eqn. 4.13 is then identified for the experimental data.

$$\hat{\zeta} = C_{\zeta'} \ln \frac{F}{\underline{F}} + \underline{\zeta} \,. \tag{4.13}$$

The identified model estimates are summarized in Table 4.6.

Table 4.6: Functional dependency of damping ratio ($\hat{\zeta}$) on excitation force (F).

Actuation Method	$C_{\zeta'}$	$\underline{F}$	$\underline{\hat{\zeta}}$	R^2_{adj}
Electromagnetic	6.19×10^{-4}	7.08×10^{-4}	5.18×10^{-4}	0.931
Strain-induced	6.49×10^{-4}	5.37×10^{-4}	2.14×10^{-3}	0.963

Although the functional relationship between force and the damping ratio given by Eqn. 4.13 and Table 4.6 could be used as the identified variable parameter model, the analytically simpler proportional damping model will be used instead. This model assumes that the damping can be described by two terms, one proportional to the mass of the system and one proportional to its stiffness:

$$c = C_{\zeta 1} \hat{m}_{\text{eff}} + C_{\zeta 2} \hat{k}_{\text{eff}} \,. \tag{4.14}$$

Substituting this model into the SDOF equation of motion and dividing through by the effective mass results in:

$$\ddot{w} + \left(C_{\zeta 1} + C_{\zeta 2} \hat{\omega}_n^2 \right) \dot{w} + \hat{\omega}_n^2 w = \left(\frac{\hat{\omega}_n^2}{\hat{k}_{\text{eff}}} \right) F(t) \,. \tag{4.15}$$

Under this model, the damping ratio can be written:

$$\hat{\zeta} = \frac{c}{2\hat{\omega}_n \hat{m}_{\text{eff}}} = \frac{1}{2}\left(\frac{C_{\zeta 1}}{\hat{\omega}_n} + C_{\zeta 2}\hat{\omega}_n\right) . \tag{4.16}$$

Thus, in the proportional damping model, two coefficients ($C_{\zeta 1}$ and $C_{\zeta 2}$) relating the damping ratio to the natural frequency must be estimated. The damping ratio as a function of natural frequency is shown in Fig. 4.15.

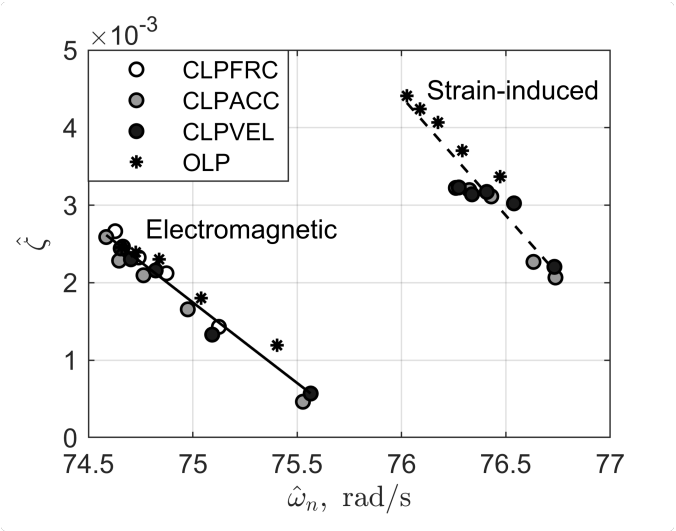

Figure 4.15: Estimated damping ratio ($\hat{\zeta}$) versus estimated natural frequency ($\hat{\omega}_n$).

The identified lines in the figure are based on the model of proportional damping in Eqn. 4.16 and with identified parameters specified in Table 4.7.

Table 4.7: Functional dependency of damping ratio ($\hat{\zeta}$) on natural frequency ($\hat{\omega}_n$).

Actuation Method	$C_{\zeta 1}$	$C_{\zeta 2}$	R^2_{adj}
Electromagnetic	11.9	-2.06×10^{-3}	0.952
Strain-induced	18.1	-3.02×10^{-3}	0.882

The identified functional relationships for $\hat{\omega}_n^2$ (given in Eqn. 4.11) and $\hat{\zeta}$ (given in Eqn. 4.16) can be substituted into Eqn. 4.1 to yield the complete identified variable parameter model for the shaker-actuated system.

For the strain-induced actuation tests, the additional parameter $\hat{\gamma}$ must be estimated for the model given in Eqn. 4.2. Its experimental values are plotted versus the squared natural frequency in Fig. 4.16.

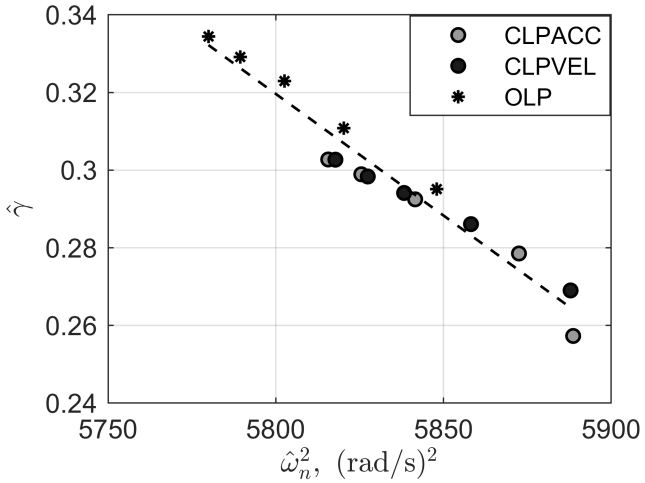

Figure 4.16: Estimated coupling correction ($\hat{\gamma}$) versus estimated squared natural frequency ($\hat{\omega}_n^2$) for strain-induced actuation.

From this plot it can be seen that only 25-35% of the analytically predicted force is present in the identified constant parameter models. For various reasons, this is as expected and

consistent with previous detailed models presented by Bilgen et al. [33]. One reason for the reduced electrical-to-mechanical coupling is the discrete fiber construction of MFC actuators, which is not accounted for in a basic *31*-mode actuation model. Only a fraction of the width which is considered active in this chapter actually contains active piezoceramic material – the remainder is composed of epoxy. Furthermore, the coupling correction decreases with the natural frequency of the system. This frequency dependence of the coupling correction is related to the frequency dependence of the piezoelectric constant, d_{31}, noted by other researchers [26] and described briefly in Appendix C. The empirical model for the coupling correction is given in Eqn. 4.17 with identified coefficients summarized in Table 4.8.

$$\hat{\gamma} = C_{\gamma 1}\hat{\omega}_n^2 + C_{\gamma 2}\,. \tag{4.17}$$

Table 4.8: Functional dependency of coupling correction ($\hat{\gamma}$) on natural frequency ($\hat{\omega}_n$).

Actuation Method	$C_{\zeta 1}$	$C_{\zeta 2}$	R^2_{adj}
Strain-induced	-6.26×10^{-4}	3.95	0.947

The functional relationship for $\hat{\gamma}$ given in Eqn. 4.17 can be substituted into Eqn. 4.2, along with the previously described functional relationships for $\hat{\omega}_n^2$ and $\hat{\zeta}$, to yield the complete identified variable parameter model for the system with strain-induced actuation. These identified models are functions of the amplitude of the input force, and thereby account for nonlinearities present in the systems due to changing excitation amplitude.

4.3.4 Comparison of Testing Methods

This section begins with a comparison of the natural frequencies predicted using the static identification of stiffness and those determined experimentally. Next, the accuracy and rel-

ative improvement of the identified variable parameter model in comparison to the constant parameter model is described.

Static Identification

Based strictly on the static testing for effective stiffness and an analytical model for the beam's effective mass, the natural frequency of the system can be estimated as $\hat{\omega}_n = \sqrt{\hat{k}_{\text{eff}}/m_{\text{eff,analytical}}}$. Assuming that the beam mode shape can be approximated by its static deflection curve, the kinetic energy of the vibrating beam can be calculated and the analytical effective lumped mass determined which yields the same kinetic energy:

$$m_{\text{eff,analytical}} = \frac{33}{140}\rho AL\,. \tag{4.18}$$

This value can be compared with the estimated effective mass determined experimentally based on the procedure previously described ($\underline{m}_{\text{eff}} = k_{\text{eff}}/\underline{\omega}_n^2$). A comparison of these estimated parameters based on static stiffness identification and on the baseline (lowest excitation level) experimental conditions is given in Table 4.9.

Table 4.9: Comparison of experimentally identified effective mass.

Method	m_{eff} (kg)	$\frac{1}{2\pi}\cdot\hat{\omega}_n$ (Hz)	$\Delta = \frac{\hat{\omega}_n - \hat{\omega}_{n,\text{analytical}}}{\hat{\omega}_{n,\text{analytical}}}$
Analytical	$m_{\text{eff,analytical}} = 0.0341$	12.9	-
Strain-induced	$\underline{\hat{m}}_{\text{eff}} = 0.0381$	12.2	-5.4%
Electromagnetic	$\underline{\hat{m}}_{\text{eff}} = 0.0393$	12.0	-7.0%

The Δ column, which is the percent difference in $\hat{\omega}_n$ relative to the analytical method, indicates that the largest relative difference between the baseline experimental cases and the analytical prediction is less than 7%. This difference is most likely attributable to un-

modeled components of the system (e.g. parasitic inertia of the accelerometers, effect of the shaker on the system dynamics, and finite stiffness of the clamp). If, for example, the mass of the mid- and tip accelerometers were taken into account (1.6 g each), the analytical effective mass would increase to 0.0363 kg based on the beam static deflection shape and equivalent kinetic energy analysis described above. The resulting analytical natural frequency decreases to 12.5 Hz, and the differences with the baseline strain-induced and electromagnetic cases reduce to -2.4% and -4.0%.

Dynamic Identification

From the identified constant parameter SDOF models and functional dependencies described above, the identified variable parameter models can be used to predict the response of the electromagnetic and strain-induced systems and then compared with the experimental FRFs. The variable parameter model comparisons are determined by the following steps:

1. Calculate the predicted natural frequency ($\hat{\omega}_n$) based on the input force amplitude at resonance from the models in Table 4.5.

2. Using the predicted natural frequency ($\hat{\omega}_n$):

   a) Determine the predicted damping ($\hat{\zeta}$) from the models in Table 4.7.

   b) Determine the predicted coupling coefficient ($\hat{\gamma}$) from the model in Table 4.8.

3. Compute the accelerance FRF amplitude and plot with the experimental data.

The plots of the variable parameter models versus experimental data for the electromagnetically actuated cases are shown in Fig. 4.17.

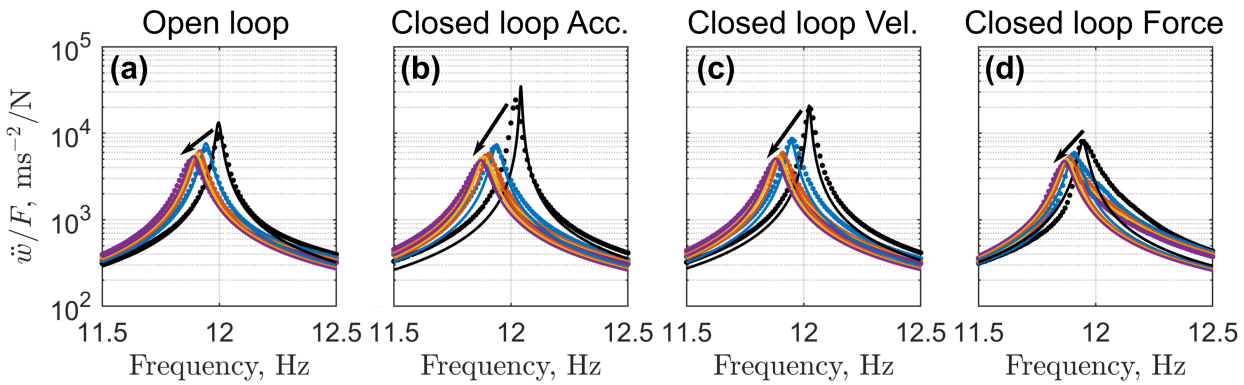

Figure 4.17: Identified variable parameter models of tip acceleration to input force ($\ddot{w}/F$) FRF amplitudes for electromagnetic actuation tests. Arrows point in the direction of increasing command amplitude.

The relative accuracy of the variable parameter model in comparison to the constant parameter models is presented quantitatively later, but here it can be observed that for these electromagnetic actuation cases, the predicted models are very good in tracking the experimental response. Slightly higher errors are present for the lowest excitation cases. In comparison to the individual identified constant parameter models for each experimental case shown in Fig. 4.11, the variable parameter model developed here is almost as effective in tracking the response of the system. For the closed loop force test cases, the softening nonlinearity is present, and this particular behavior cannot be accounted for by the linear models assumed here. It may be useful to reiterate here that the constant parameter models shown in Fig. 4.11 can not be used to predict the system response for different excitation amplitudes, but rather are minimum residual models for a single excitation amplitude. The variable parameter model shown in Fig. 4.17, on the other hand, is based on the identified baseline parameters and the variable parameter model. It can track the changes in system parameters as a function of the input excitation amplitude.

The process described above can be used for strain-induced actuation, and plots of the variable parameter model versus experimental data are shown in Fig. 4.18.

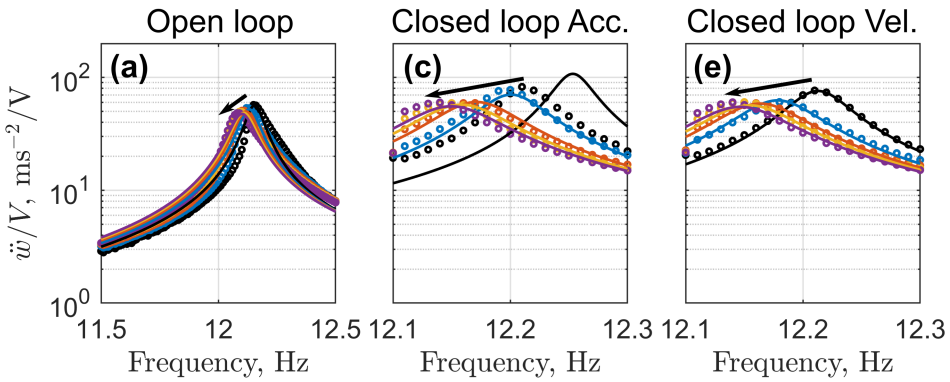

Figure 4.18: Identified variable parameter models of tip acceleration to input voltage ($\ddot{w}/V$) FRF amplitudes for strain-induced actuation tests. Arrows point in the direction of increasing command amplitude.

For the strain-induced actuation cases, the predicted models are again relatively good (quantified later) in tracking the experimental response. In comparison to the individual identified constant parameter models for each experimental case shown in Fig. 4.12, the variable parameter model developed here also tracks the trends in natural frequency and damping as the input force amplitude increases. As for the electromagnetic actuation cases, the softening nonlinear is present for the open loop test cases, and this is not accounted for with the assumed linear models. A comparison of the parameter estimates for $\hat{\omega}_n$, $\hat{\zeta}$, and $\hat{\gamma}$ using the various empirical and modeling techniques described in this chapter is summarized in Appendix F.

One anomalous case to note is the variable parameter model prediction for the lowest excitation level in the closed loop acceleration test. As can be seen in Fig. 4.18(b), the prediction for this case is quite far off in both ω_n and ζ, which demonstrates part of the reason that the reported correlation statistics in Tables 4.5 and 4.7 for the models for strain-induced tests are lower than those for the electromagnetic tests. For the other cases, the experimental response is predicted well by the identified model.

The absolute estimated parameter errors using the constant and variable parameter

models are shown in Table 4.10. For each testing procedure, the maximum absolute error is taken as the maximum absolute difference after subtracting each parameter estimate (based on the residual minimization routine) from its corresponding reference value. The reference value for the constant parameter models is the lowest excitation amplitude case (i.e. $\underline{\omega_n}$ and $\underline{\zeta}$ as given in Tables 4.5 and 4.6). The reference value for the coupling correction is the mean of the two values corresponding to the two lowest excitation amplitude cases ($\underline{\gamma} = 0.273$). The parameter errors for the variable parameter model are calculated in a similar manner, except that the references are not the baseline parameter estimates but rather the identified variable parameter models. For each parameter, the Δ column in Table 4.10 reports the reduction in maximum parameter error between the constant and variable parameter models. As an example, if the maximum absolute error for a particular variable parameter were zero, this error reduction metric would be 100%. For each set of test conditions, the variable parameter model reduces the maximum parameter error significantly.

Table 4.10: Maximum parameter error for constant parameter (e_{CP}) and variable parameter (e_{VP}) models, and relative improvement of variable parameter model.

		$\hat{\omega}_n$ (rad/s)			$\hat{\zeta}$ (%)			$\hat{\gamma}$		
Actuation Method	Testing Procedure	e_{CP}	e_{VP}	$\Delta = \frac{e_{\mathrm{CP}} - e_{\mathrm{VP}}}{e_{\mathrm{CP}}}$	e_{CP}	e_{VP}	$\Delta = \frac{e_{\mathrm{CP}} - e_{\mathrm{VP}}}{e_{\mathrm{CP}}}$	e_{CP}	e_{VP}	$\Delta = \frac{e_{\mathrm{CP}} - e_{\mathrm{VP}}}{e_{\mathrm{CP}}}$
Electromagnetic	Open Loop	0.89	0.05	*94%*	0.19	0.03	*85%*	-	-	-
	Constant Acceleration	0.96	0.05	*95%*	0.21	0.02	*90%*	-	-	-
	Constant Velocity	0.89	0.03	*97%*	0.19	0.02	*89%*	-	-	-
	Constant Force	0.92	0.07	*92%*	0.21	0.01	*94%*	-	-	-
Strain-induced	Open Loop	0.75	0.10	*85%*	0.23	0.04	*82%*	0.07	0.006	*92%*
	Constant Acceleration	0.47	0.08	*84%*	0.11	0.04	*65%*	0.03	0.007	*80%*
	Constant Velocity	0.46	0.04	*91%*	0.11	0.03	*70%*	0.03	0.006	*83%*

Table 4.11: Maximum accelerance FRF magnitude error for constant parameter (e_{CP}) and variable parameter (e_{VP}) models, and relative improvement of variable parameter model.

Actuation Method	Testing Procedure	e_{CP} $((\mathrm{m/s^2})/\mathrm{N})$ or (V)	e_{VP} $((\mathrm{m/s^2})/\mathrm{N})$ or (V)	$\Delta = \frac{e_{\mathrm{CP}} - e_{\mathrm{VP}}}{e_{\mathrm{CP}}}$
Electromagnetic	Open Loop	5.2×10^3	1.1×10^4	*-105%**
	Constant Acceleration	2.0×10^4	9.7×10^3	*53%*
	Constant Velocity	1.5×10^4	1.1×10^3	*93%*
	Constant Force	3.8×10^3	4.3×10^2	*88%*
Strain-induced	Open Loop	8.9	1.7	*81%*
	Constant Acceleration	23	25	*-11%***
	Constant Velocity	20	5.4	*72%*

In Table 4.11, a comparison of the error in the maximum magnitude of the accelerance FRF is given for the constant and variable parameter models. As above, the errors are determined by subtracting the maximum accelerance magnitude from a reference value. For the constant parameter model, the reference value is the maximum accelerance magnitude at the lowest excitation amplitude, and for the variable parameter model, the reference is the maximum accelerance magnitude corresponding to the identified variable parameter model. The Δ column is computed in the same manner as before.

For all but two cases, the variable parameter model reduces the error in the maximum accelerance magnitude significantly. A close examination of Figure 4.17(a) indicates that for the electromagnetic, open loop test, the variable parameter estimated damping is underestimated for the lowest amplitude forcing case, leading to a high maximum accelerance magnitude and a high error in comparison to the data (as indicated by * in Table 4.11). The next highest error for this testing procedure is 1.1×10^3 $(\mathrm{m/s^2})/\mathrm{N}$, corresponding to an error reduction of $\Delta = 79\%$.

Similarly, as discussed above, the variable parameter model prediction for the damping ratio in the strain-induced, constant acceleration case (Fig. 4.17(b)) is also significantly underestimated. This also leads to a relatively high error (as indicated by ** in Table 4.11). For this case, the next highest error is 9.0 $(\mathrm{m/s^2})/\mathrm{V}$, corresponding to an error reduction of $\Delta = 60\%$.

Although the constant force procedure for electromagnetic actuation and the open loop procedure for strain-induced actuation both reduce the errors in parameter estimation and maximum FRF magnitude, they also produce FRFs with significant softening nonlinearities. For the testing procedures which do not exhibit this un-modeled softening, the constant velocity testing procedures are the most effective in reducing the parameter and maximum FRF magnitude errors for both actuation methods. For electromagnetic actuation, the variable parameter model for constant velocity testing leads to error reductions of 97% for the natural frequency, 89% for the damping ratio, and 93% for the maximum FRF magnitude

over the constant parameter model. For strain-induced actuation, the error reduction of the variable over the constant parameter model for constant velocity testing is 91% for natural frequency, 70% for damping ratio, 83% for coupling coefficient, and 72% for the maximum FRF magnitude. These error reductions are significant and lead to improved system models over a range of excitation amplitudes.

4.4 Summary

Using both electromagnetic and strain-induced excitation, this chapter experimentally demonstrates the emergence of significant nonlinear behavior in the response of a cantilever beam to harmonic low-amplitude excitation. These nonlinearities result in different parameter estimates for varying actuation types and amplitudes. Various types of experimental procedures are described in detail and implemented to develop empirical models for tracking changes in parameters such as natural frequency, damping ratio, and coupling correction. The variable parameter empirical models are shown to track the changes very well over the investigated parameter domains. The magnitude of their improved predictive power over constant parameter models is quantified and discussed in detail.

In the reported results, it is seen that constant force and voltage methods produce empirical data with significant softening characteristics that are not accounted for in the identified second order model. The models for the constant response tests, on the other hand, closely approximate the experimental data throughout the frequency domain. Additionally, in the constant response cases the lowest excitation force at resonance can be achieved while staying above the sensor noise floor. This is critical, as low amplitude excitation yields the best estimate of the baseline natural frequency with minimal nonlinear effects. Finally, the closed loop velocity tests are shown to have the largest error reductions in the parameter and maximum FRF magnitude estimates for both actuation methods. Utilizing the constant velocity method, therefore, to develop the empirical model for parameter variation described in this chapter yields the most accurate model for the system's dynamics.

In summary, the proposed methodology for the identification of a lumped parameter model for a weakly nonlinear second order system requires the following three steps:

1. Static test: Estimate the effective stiffness.

2. Harmonic frequency sweep test at an excitation amplitude as low as possible while maintaining signals of interest sufficiently above noise floor: Estimate the baseline natural frequency ($\underline{\omega}_n$) with minimum nonlinear effects.

3. Harmonic frequency sweep test at the highest excitation amplitude that is required for predictive models: Estimate the empirical functional relationships for ω_n^2, ζ, and γ using the specified models given by Eqns. 4.11, 4.16, and 4.17.

Only one high-amplitude excitation test is required to develop the empirical models for the parameter changes, although more measurements will increase the confidence in the accuracy of the estimates. When available, a closed loop controller should be utilized so that constant response type tests can be conducted. These generalized procedures presented in this chapter can thereby be used in the identification of other weakly nonlinear second order systems.

CHAPTER 5
SUMMARY

In this thesis, the dynamics of cantilever beam and plate structures have been investigated through a modal approach. Chapter 2 develops the analytical models which are used in the following chapters for describing the mechanics of beams and plates. Both distributed and lumped parameter models are described and various solutions provided, including exact and approximate solutions where appropriate. The bending and twisting behaviors are particularly important as they are employed in the shape sensing development of Chapter 3. Analytical results for the cantilever beam are presented in detail, and approximate methods for solving the cantilever plate equation of motion are presented.

Chapter 3 focuses on the use of fiber optic strain sensors for shape identification. After a brief introduction to the use of Fiber Bragg Gratings as optical strain sensors is given, the focus of the remainder of the chapter is on their use in structural shape estimation. Referencing the results of Chapter 2, the analytical correspondence between strain measurements and the local curvature or twist is shown. Using these results, experimental tests are presented for the cantilever beam and plate which estimate the mode shapes for these structures based on the strain distributions. These experimental results, which are compared with analytical and numerical predictions, correspond quite well for the studied modes. Based on these tests, it is shown that measurements from fiber optic strain sensors can be used effectively to reconstruct the bending and twisting deformation of cantilever beams and plates.

After investigating a method to compare experimental and theoretical mode shapes in Chapter 3, in Chapter 4 an experimental procedure for system identification of weakly nonlinear systems is presented. Through the development of empirical models, the variation in identified parameters due to nonlinear system response is accurately incorporated into a modified linear model. The accuracy of the variable parameter model is compared to a constant parameter model and shown to yield significantly improved results.

5.1 Contributions

Research related to this thesis has been presented and published at the 2017 ASME Smart Materials, Adaptive Structures and Intelligent Systems (SMASIS) Conference. An additional conference paper has been accepted and will be presented at the 2018 AIAA Aviation and Aeronautics Forum and Exposition. The citations for these publications are below:

1. P. S. Heaney and O. Bilgen, "Nonlinearities in experimental system identification of a piezocomposite beam model," in *Proceedings of ASME 2017 Conference on Smart Materials, Adaptive Structures and Intelligent Systems*, vol. 2, Snowbird, UT, USA, 2017

2. P. S. Heaney and O. Bilgen, "Experimental mode shape identification for a cantilever beam using optical fiber bragg gratings," in *Proceedings of ASME 2017 Conference on Smart Materials, Adaptive Structures and Intelligent Systems*, vol. 2, Snowbird, UT, USA, 2017

3. P. S. Heaney, T. G. Ivanco, and O. Bilgen, "Distributed sensing of a cantilever beam and plate using a fiber optic sensing system," in *Proceedings of 2018 AIAA Aviation and Aeronautics Forum and Exposition (AIAA Aviation)*, Atlanta, GA, 2018

5.2 Future Work

Future research on these topics will focus on developing and extending methods to use fiber optic sensors for control applications. Higher fidelity shape sensing methods can also be developed by integrating additional sensing fibers and utilizing more sophisticated shape reconstruction algorithms. Since the twist rate fiber in this work yielded noisy strain results, another topic of future investigation will be developing methods to increase the quality of the shear strain measurements for use in reconstructing structural twist.

An area for additional work in empirical system identification for weakly nonlinear

systems is to complete similar variable parameter models for multiple modes of a structure and develop accurate MDOF variable parameter models which track parameter shifts due to nonlinearities. The performance difference between the constant and variable parameter model in structural control is also a potential area of research.

REFERENCES

[1] W. L. Ko, W. L. Richards, and V. T. Tran, "Displacement theories for in-flight deformed shape predictions of aerospace structures," *NASA/TP-2007-214612*, 2007.

[2] L. Li, B. Zhong, W. Li, W. Sun, and X. Zhu, "Structural shape reconstruction of fiber bragg grating flexible plate based on strain modes using finite element method," *Journal of Intelligent Material Systems and Structures*, 2017.

[3] S. L. Vazquez, A. Tessler, C. C. Quach, E. G. Cooper, J. Parks, and J. L. Spangler, "Structural health monitoring using high-density fiber optic strain sensor and inverse finite element methods," NASA/TM-2005-213761, Tech. Rep., 2005.

[4] M. Gherlone, P. Cerracchio, M. Mattone, M. D. Sciuva, and A. Tessler, "Shape sensing of 3d frame structures using and inverse finite element method," *International Journal of Solids and Structures*, vol. 49, pp. 3100–3112, 2012.

[5] C. Pak, "Wing shape sensing from measured strain," *AIAA Journal*, vol. 54, no. 3, pp. 1064–1073, 2016.

[6] R. T. Jones, D. G. Bellemore, T. A. Berkoff, J. S. Sirkis, M. A. Davis, M. A. Putnam, E. J. Friebele, and A. D. Kersey, "Determination of cantilever plate shapes using wavelength division multiplexed fiber bragg grating sensors and a least-squares strain-fitting algorithm," *Smart Materials and Structures*, vol. 7, pp. 178–188, 1998.

[7] R. Glaser, V. Caccese, and M. Shahinpoor, "Shape monitoring of a beam structure from measured strain or curvature," *Experimental Mechanics*, vol. 52, no. 6, pp. 591–606, 2012.

[8] J. A. Bakalyar and C. Jutte, "Validation tests of fiber optic strain-based operational shape and load measurements," *AIAA Structures, Structural Dynamics and Materials Conference, 23-26 April 2012, Honolulu, Hawaii*, 2012.

[9] A. Derkevorkian, S. F. Masri, J. Alvarenga, H. Boussalis, J. Bakalyar, and W. L. Richards, "Strain-based deformation shape-estimation algorithm for control and monitoring applications," *AIAA Journal*, vol. 51, no. 9, pp. 2231–2240, 2013.

[10] B. A. Childers, M. E. Froggatt, S. G. Allison, T. C. Moore, D. A. Hare, C. F. Batten, and D. C. Jegley, "Use of 3000 bragg grating strain sensors distributed on four eight-m optical fibers during static load tests of a composite structure," in *Proc. SPIE 4332, Smart Structures and Materials 2001: Industrial and Commercial Applications of Smart Structures Technologies*, Jun. 2001.

[11] C. V. Jutte, W. L. Ko, C. A. Stephens, J. A. Bakalyar, W. L. Richards, and A. R. Parker, "Deformed shape calculation of a full-scale wing using fiber optic strain data from a ground loads test," NASA/TP-2011-215975, Tech. Rep., 2011.

[12] M. J. Nicolas, R. W. Sullivan, and W. L. Richards, "Large scale applications using fbg sensors: Determination of in-flight loads and shape of a composite aircraft wing," *Aerospace*, vol. 3, no. 18, 2016.

[13] A. Cusano, P. Capoluongo, S. Campopiano, A. Cutolo, M. Giordano, F. Felli, A. Paolozzi, and M. Caponero, "Experimental modal analysis of an aircraft model wing by embedded fiber bragg grating sensors," *IEEE Sensors Journal*, vol. 6, no. 1, pp. 67–77, 2006.

[14] H. Jiang, B. van der Veek, D. Kirk, and H. Gutierrez, "Real-time estimation of time-varying bending modes using fiber bragg grating sensor arrays," *AIAA Journal*, vol. 51, no. 1, pp. 178–185, 2013.

[15] K. Chau, B. Moslehi, G. Song, and V. Sethi, "Experimental demonstration of fiber bragg grating strain sensors for structural vibration control," in *Proceedings of SPIE 5391, Smart Structures and Materials 2004: Sensors and Smart Structures Technologies for Civil, Mechanical, and Aerospace Systems*, Jul. 2004.

[16] F. Braghin, G. Cazzulani, S. Cinquemani, and F. Resta, "Potential of fbg sensors for vibration control in smart structures," in *Proceedings of the 2013 IEEE International Conference on Mechatronics*, Vicenza, Italy, Feb. 2013.

[17] G. Cazzulani, S. Cinquemani, L. Comolli, and F. Resta, "A quasi-modal approach to overcome fbg limitations in vibration control of smart structures," *Smart Materials and Structures*, vol. 22, Nov. 2013.

[18] G. Cazzulani, S. Cinquemani, L. Comolli, A. Gardella, and F. Resta, "Vibration control of smart structures using an array of fiber bragg grating sensors," *Mechatronics*, vol. 24, pp. 345–353, 2014.

[19] D. J. Ewins, *Modal testing: Theory, Practice, and Application*. Baldock, Hertfordshire, England: Research Studies Press, Ltd., 2000.

[20] G. Kerschen, K. Worden, A. Vakakis, and J. Golinval, "Past, present and future of nonlinear system identification in structural dynamics," *Mechanical Systems and Signal Processing*, vol. 20, no. 3, pp. 505–592, 2006.

[21] T. Doughty, P. Davies, and A. Bajaj, "A comparison of three techniques using steady state data to identify non-linear modal behavior of externally excited cantilever beams," *Journal of Sound and vibration*, vol. 249, no. 4, pp. 785–813, 2002.

[22] P. Malatkar, "Nonlinear vibrations of cantilever beams and plates," PhD thesis, Virginia Polytechnic Institute and State University, 2003.

[23] E. F. Crawley and J. de Luis, "Use of piezoelectric actuators as elements of intelligent structures," *AIAA Journal*, vol. 25, no. 10, pp. 1373–1385, 1987.

[24] S. Im and S. Atluri, "Effects of a piezo-actuator on a finitely deformed beam subjected to general loading," *AIAA Journal*, vol. 27, no. 12, pp. 1801–1807, 1989.

[25] N. W. Hagood, W. H. Chung, and A. von Flotow, "Modelling of piezoelectric actuator dynamics for active structural control," *Journal of Intelligent Material Systems and Structures*, vol. 1, no. 3, pp. 327–354, 1990.

[26] E. F. Crawley and E. H. Anderson, "Detailed models of piezoceramic actuation of beams," *Journal of Intelligent Material Systems and Structures*, vol. 1, no. 1, pp. 4–25, 1990.

[27] N. W. Hagood and A. von Flotow, "Damping of structural vibrations with piezoelectric materials and passive electrical networks," *Journal of Sound and Vibration*, vol. 146, no. 2, pp. 243–268, 1991.

[28] S. J. Kim and J. D. Jones, "Influence of piezo-actuator thickness on the active vibration control of a cantilever beam," *Journal of Intelligent Material Systems and Structures*, vol. 6, no. 5, pp. 610–623, 1995.

[29] C. Park and I. Chopra, "Modeling piezoceramic actuation of beams in torsion," *AIAA Journal*, vol. 34, no. 12, Dec. 1996.

[30] M. C. Brennan and A. R. McGowan, "Piezoelectric power requirements for active vibration control," *Proceedings of SPIE 4th Annual Symposium on Smart Structures and Materials*, vol. 3039, pp. 660–669, 1997.

[31] A. Erturk and D. J. Inman, "On mechanical modeling of cantilevered piezoelectric vibration energy harvesters," *Journal of Intelligent Material Systems and Structures*, vol. 19, no. 11, pp. 1311–1325, 2008.

[32] A. Erturk and D. J. Inman, "A distributed parameter electromechanical model for cantilevered piezoelectric energy harvesters," *Journal of Vibration and Acoustics*, vol. 130, 2008.

[33] O. Bilgen, A. Erturk, and D. J. Inman, "Analytical and experimental characterization of macro-fiber composite actuated thin clamped-free unimorph benders," *Journal of Vibration and Acoustics*, vol. 132, Oct. 2010.

[34] O. Bilgen, Y. Wang, and D. J. Inman, "Electromechanical comparison of cantilevered beams with multifunctional piezoceramic devices," *Mechanical Systems and Signal Processing*, vol. 27, pp. 763–777, 2012.

[35] I. H. Shames and C. L. Dym, *Energy and Finite Element Methods in Structural Mechanics*. Taylor & Francis, 2003.

[36] D. T. Greenwood, *Classical Dynamics*. Prentice-Hall, Inc., 1977.

[37] W. E. Boyce and R. C. DiPrima, *Elementary Differential Equations and Boundary Value Problems*, 10th. Wiley, 2012.

[38] D. J. Inman, *Vibration with Control*. John Wiley & Sons, Ltd, 2006.

[39] D. H. Hodges and G. A. Pierce, *Introduction to Structural Dynamics and Aeroelasticity*, ser. Cambridge Aerospace Series. Cambridge University Press, 2002.

[40] W. C. Young and R. G. Budynas, *Roark's Formulas for Stress and Strain*, Seventh. McGraw-Hill, 2002.

[41] S. S. Rao, *Vibration of Continuous Systems*. John Wiley & Sons, Inc., 2007.

[42] G. Warburton, "The vibration of rectangular plates," *Proceedings of the Institution of Mechanical Engineers*, vol. 168, no. 1, pp. 371–384, 1954.

[43] A. W. Leissa, "Vibration of plates," National Aeronautics and Space Administration, research rep. NASA SP-160, 1969.

[44] A. Leissa, "The free vibration of rectangular plates," *Journal of Sound and Vibration*, vol. 31, no. 3, pp. 257–293, 1973.

[45] R. B. Bhat, "Natural frequencies of rectangular plates using characteristic orthogonal polynomials in rayleigh-ritz method," *Journal of Vibration and Sound*, vol. 102, no. 4, pp. 493–499, 1985.

[46] R. R. Craig and A. J. Kurdila, *Fundamentals of structural dynamics*, 2nd. John Wiley & Sons, Inc., 2006.

[47] N. M. Newmark, "A method of computation for structural dynamics," *Journal of the Engineering Mechanics Division*, pp. 67–94, Jul. 1959.

[48] R. C. Hibbeler, *Engineering Mechanics. Statics.* 13th. Upper Saddle River, N.J.: Pearson, 2013.

[49] MSC Software, *MSC Nastran 2018.0*, software.

[50] M. H. Sadd, *Elasticity: Theory, Applications, and Numerics*. Elsevier, 2005.

[51] J. Francu, P. Novackova, and P. Janicek, "Torsion of a non-circular bar," *Engineering Mechanics*, vol. 19, no. 1, pp. 45–60, 2012.

[52] Bruel & Kjaer, *Mini-shaker type 4810 instruction manual*.
[53] National Instruments, *LabVIEW 2015*, Software.
[54] Smart Material Corporation, *Macro Fiber Composite - MFC*.
[55] The MathWorks, Inc., *MATLAB 2017b*, Natick, Massachusetts.
[56] P. S. Heaney and O. Bilgen, "Nonlinearities in experimental system identification of a piezocomposite beam model," in *Proceedings of ASME 2017 Conference on Smart Materials, Adaptive Structures and Intelligent Systems*, vol. 2, Snowbird, UT, USA, 2017.
[57] ——, "Experimental mode shape identification for a cantilever beam using optical fiber bragg gratings," in *Proceedings of ASME 2017 Conference on Smart Materials, Adaptive Structures and Intelligent Systems*, vol. 2, Snowbird, UT, USA, 2017.
[58] P. S. Heaney, T. G. Ivanco, and O. Bilgen, "Distributed sensing of a cantilever beam and plate using a fiber optic sensing system," in *Proceedings of 2018 AIAA Aviation and Aeronautics Forum and Exposition (AIAA Aviation)*, Atlanta, GA, 2018.
[59] J. L. Meriam, *Dynamics*, 2nd. John Wiley & Sons, Inc., 1975.
[60] D. J. Inman, *Engineering Vibration*, 4th. USA, USA: Pearson, 2014.
[61] T. R. Chandrupatla and A. D. Belegundu, *Introduction to Finite Elements in Engineering*, 4th. Pearson, 2012.
[62] P. S. Heaney and G. Hou, "Projection method with minimal correction procedure for numerical simulation of constrained dynamics," in *ASME 2017 Dynamic Systems and Control Conference*, Tysons Corner, VA, 2017.

APPENDIX A
VIBRATION OF SINGLE DEGREE OF FREEDOM SYSTEMS

A.1 Equation of Motion

Consider the single degree of freedom (SDOF) system shown in Fig. A.1, where m, k, and c are the lumped parameters for the system's mass, stiffness and damping constant, w is the degree of freedom, and F is an external force.

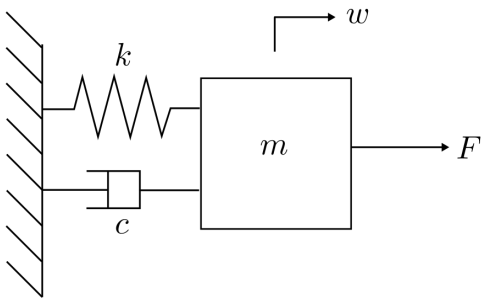

Figure A.1: Representative SDOF spring-mass-damper system.

Although this class of system is relatively simple, the methods and results developed through its analysis are quite useful and relevant for more complex systems to be discussed later. The equation of motion for this system will be derived below in two manners: (1) Newton's Method and (2) Lagrange's Method. These two methods yield equivalent results, although for some problems one or the other method will prove easier to carry out, so both methods will be illustrated here.

A.1.1 Newton's Method

Newton's second law indicates that the acceleration of an object is proportional to the net force acting on it [59]. It follows that Newton's method for deriving an object's equation of motion requires determining the net force acting on the object, which is equal to the product of the object's acceleration and a constant of proportionality (the object's mass). This can be expressed in equation form as: $\sum \text{Forces} = m\ddot{w}$. For the representative SDOF system shown in Fig. A.1, the summation of forces and subsequent rearrangement leads to the following equation of motion:

$$\begin{aligned} F - kw - c\dot{w} &= m\ddot{w} \\ \Rightarrow m\ddot{w} + c\dot{w} + kw &= F\,. \end{aligned} \tag{A.1}$$

This equation of motion, a second-order ordinary differential equation, is characteristic of a damped harmonic oscillator and will be the subject of the analytical development in this appendix.

A.1.2 Lagrange's Method

The Lagrangian function is defined as $L(q, \dot{q}, t) = T - V$, where T is the kinetic energy, V is the potential energy, and q is a generalized coordinate of the system. By Lagrange's Method [36], the equation of motion can be determined by evaluating the associated terms in the following equation:

$$\frac{d}{dt}\left(\frac{\partial L}{\partial \dot{q}}\right) - \frac{\partial L}{\partial q} = Q\,, \tag{A.2}$$

where Q is a generalized force not derivable from a potential function. For our system, w is the generalized coordinate and the damper is modeled as a external force. The Lagrangian

L and generalized force Q for the system are then given by:

$$\begin{aligned} L &= \frac{1}{2}m\dot{w}^2 - \frac{1}{2}kw^2 \\ Q &= F - c\dot{w}\,. \end{aligned} \tag{A.3}$$

Each term in Eqn. A.2 can then be evaluated:

$$\begin{aligned} \frac{d}{dt}\left(\frac{\partial L}{\partial \dot{w}}\right) &= \frac{d}{dt}\left(m\dot{w}\right) = m\ddot{w} \\ \frac{\partial L}{\partial w} &= -kw\,. \end{aligned} \tag{A.4}$$

Substituting these results into Eqn. A.2 and then rearranging yields the equation of motion for the system:

$$\begin{aligned} m\ddot{w} + kw &= F - c\dot{w} \\ \Rightarrow m\ddot{w} + c\dot{w} + kw &= F\,. \end{aligned} \tag{A.5}$$

Clearly, after rearrangement this equation of motion is equivalent to that obtained using Newton's Method as given in Eqn. A.1.

A.2 Free Vibration

The first class of problems to be analyzed using the SDOF equation of motion derived in the previous section is that of free vibration. These type of problems involve analyzing the unforced equation of motion:

$$m\ddot{w} + c\dot{w} + kw = 0\,. \tag{A.6}$$

A.2.1 Assumed Solution Method

One of the more useful methods of solution for vibration problems is known as the assumed solution method (or method of undetermined coefficients), which involves determining an assumed solution form and then substituting into the given equation of motion [60]. For

the SDOF system, the assumed solution to be employed is $w = ae^{\lambda t}$ where λ is a complex quantity. Substituting this assumed form into the equation of motion:

$$\begin{aligned} \left(m\lambda^2 + c\lambda + k\right) ae^{\lambda t} &= 0 \\ \Rightarrow m\lambda^2 + c\lambda + k &= 0\,. \end{aligned} \tag{A.7}$$

This is known as the characteristic equation of the system, and its solution is easily determined from the quadratic formula:

$$\begin{aligned} \lambda &= -\frac{c}{2m} \pm \frac{1}{2m}\sqrt{c^2 - 4km} \\ \Rightarrow \lambda &= -\frac{c}{2m} \pm j\frac{1}{2m}\sqrt{4km - c^2}\,. \end{aligned} \tag{A.8}$$

In the form given in the second line, λ is written as a pair of complex conjugates, where the real part is related to the system's damping, and the imaginary part is related to the system's oscillation. The imaginary component is equal to zero when:

$$c_{\text{cr}} = 2\sqrt{km}\,, \tag{A.9}$$

which is known as the critical damping constant. When $c = c_{\text{cr}}$, the system response will not include any oscillation and the system is called critically damped. Alternatively, when $c > c_{\text{cr}}$, the first line of Eqn. A.8 indicates that the second term contributes to the real component of λ and the system damping is increased. This type of system is called overdamped. The case of most interest here is when $c < c_{\text{cr}}$, which is characteristic of underdamped systems. These systems exhibit damped oscillation and occur frequently in many fields of study.

The damping ratio ζ is another useful way to represent the system damping and is the ratio of the damping constant to the critical damping constant:

$$\zeta = \frac{c}{c_{\text{cr}}} = \frac{c}{2\sqrt{km}}\,. \tag{A.10}$$

This parameter can then be used to write the damped natural frequency, which is the oscillation frequency as expressed in Eqn. A.8:

$$\omega_d = \frac{1}{2m}\sqrt{4km - c^2} = \frac{1}{2m}\sqrt{4km\,(1-\zeta^2)} = \sqrt{\frac{k}{m}}\sqrt{1-\zeta^2} = \omega_n\sqrt{1-\zeta^2}\,, \tag{A.11}$$

where the undamped natural frequency ω_n is the frequency corresponding to $\zeta = 0$:

$$\omega_n = \sqrt{\frac{k}{m}}\,. \tag{A.12}$$

Using these parameters, the solution for λ given in Eqn. A.8 can be written:

$$\lambda = -\zeta\omega_n \pm j\omega_d\,, \tag{A.13}$$

and the assumed solution form as:

$$\begin{aligned} w &= ae^{(-\zeta\omega_n \pm j\omega_d)t} \\ &= e^{-\zeta\omega_n t}\left(C_1 e^{j\omega_d t} + C_2 e^{-j\omega_d t}\right)\,, \end{aligned} \tag{A.14}$$

where the constants a, C_1, and C_2 are determined from initial conditions. If there is no initial displacement or initial velocity, then the system response w is zero. This solution method naturally yields a solution in the time domain.

For comparison with the next method of solution, the exponential form of the solution can be written in trigonometric form as:

$$w = e^{-\zeta\omega_n t}\left(A\cos\omega_d t + B\sin\omega_d t\right)\,, \tag{A.15}$$

where A and B are constants to be determined based on the initial conditions. At $t = 0$:

$$\begin{aligned} A &= w_0 \\ \dot{w}_0 &= -A\zeta\omega_n + B\omega_d \\ \Rightarrow B &= \frac{\dot{w}_0 + \zeta\omega_n w_0}{\omega_d}\,. \end{aligned} \tag{A.16}$$

Given initial conditions w_0 and $\dot{w}_0$, the unforced system response can then be determined.

A.2.2 Laplace Solution Method

An alternative solution method utilizes the Laplace Transform, and naturally yields a solution in the frequency domain. Taking the Laplace Transform of the unforced equation of motion Eqn. A.6:

$$m\left(s^2W - w_0 s - \dot{w}_0\right) + c\left(sW - w_0\right) + kW = 0\,, \tag{A.17}$$

where the subscript 0 indicates the initial condition for that quantity and W indicates the Laplace transform of w. Solving for W and then dividing the numerator and denominator by m yields:

$$\begin{aligned} W &= \frac{m\left(w_0 s + \dot{w}_0\right) + cw_0}{ms^2 + cs + k} \\ &= \frac{w_0 s + \dot{w}_0 + 2\zeta\omega_n w_0}{s^2 + 2\zeta\omega_n s + \omega_n^2}\,. \end{aligned} \tag{A.18}$$

The numerator of this expression indicates that for free vibration, if there are no initial displacement or initial velocity (i.e. $w_0 = \dot{w}_0 = 0$), the system response W is zero.

The equivalence of the solution using the assumed solution method given by Eqn. A.14 with the solution derived here is best shown using the trigonometric form of the time domain

solution (Eqn. A.15) and then taking the Laplace transform:

$$\begin{aligned} w &= e^{-\zeta\omega_n t}\left(A\cos\omega_d t + B\sin\omega_d t\right) \\ W &= \frac{A\left(s+\zeta\omega_n\right)+B\omega_d}{\left(s+\zeta\omega_n\right)^2+\omega_d^2} \\ &= \frac{A\left(s+\zeta\omega_n\right)+B\omega_d}{s^2+2\zeta\omega_n s+\zeta^2\omega_n^2+\omega_n^2\left(1-\zeta^2\right)} \\ &= \frac{A\left(s+\zeta\omega_n\right)+B\omega_d}{s^2+2\zeta\omega_n s+\omega_n^2}\,. \end{aligned} \tag{A.19}$$

Comparing Eqn. A.19 and Eqn. A.18, $A = w_0$ and $A\zeta\omega_n + B\omega_d = \dot{w}_0 + 2\zeta\omega_n w_0$. Solving for B indicates that:

$$B = \frac{\dot{w}_0 + \zeta\omega_n w_0}{\omega_d}\,. \tag{A.20}$$

These values for A and B correspond exactly with those obtained for the constants using the assumed solution method; thus, the solutions are equivalent.

A.3 Forced Vibration

A.3.1 Assumed Solution Method

Now consider the system response to harmonic forcing, $F(t) = F_0 e^{j\omega t}$. Following the same process as in the free vibration case, the particular solution here is assumed to be of the form $w_p = Ae^{j\omega t}$. The physical intuition behind this choice is that when forced at frequency ω, the system response will oscillate at that same frequency. The coefficient A is complex valued and accounts for amplification or attenuation of the forcing signal as well as phase lag between the force and the response. Substituting this assumed form into the forced equation of motion, Eqn. A.1, and then dividing through by m:

$$\begin{aligned} \left(-m\omega^2 + cj\omega + k\right)Ae^{j\omega t} &= F_0 e^{j\omega t} \\ \left(\left(\omega_n^2 - \omega^2\right) + 2\zeta\omega_n j\omega\right)Ae^{j\omega t} &= f_0 e^{j\omega t}\,, \end{aligned} \tag{A.21}$$

where f_0 is the mass normalized forcing amplitude. Solving for A in Eqn. A.21:

$$A = \frac{f_0}{(\omega_n^2 - \omega^2) + 2\zeta\omega_n j\omega} = \frac{f_0\left[(\omega_n^2 - \omega^2) - 2\zeta\omega_n j\omega\right]}{(\omega_n^2 - \omega^2)^2 + (2\zeta\omega_n\omega)^2}\,. \tag{A.22}$$

The modulus, or amplitude, and phase of this complex value are:

$$\begin{aligned} |A| &= \frac{f_0}{\sqrt{(\omega_n^2 - \omega^2)^2 + (2\zeta\omega_n\omega)^2}} \\ \underline{\angle A} &= -\tan^{-1}\left(\frac{2\zeta\omega_n\omega}{\omega_n^2 - \omega^2}\right)\,. \end{aligned} \tag{A.23}$$

Defining $\phi = -\underline{\angle A}$, by Euler's formula the coefficient A can be written:

$$\begin{aligned} A &= |A|\, e^{j\underline{\angle A}} \\ &= \frac{f_0}{\sqrt{(\omega_n^2 - \omega^2)^2 + (2\zeta\omega_n\omega)^2}} e^{-j\phi}\,, \end{aligned} \tag{A.24}$$

and the particular solution can be written:

$$w_p = Ae^{j\omega t} = |A|\, e^{j\left(\omega t + \underline{\angle A}\right)} = \frac{f_0}{\sqrt{(\omega_n^2 - \omega^2)^2 + (2\zeta\omega_n\omega)^2}} e^{j(\omega t - \phi)}\,. \tag{A.25}$$

Based on this expression, the forced solution is oscillatory with frequency ω, phase ϕ, and amplitude $|A|$. While the oscillatory component of the response, $e^{j(\omega t-\phi)}$, is strictly dependent on the parameters of the forcing function, the amplitude of the response changes based on the excitation parameters as well as the system properties ω_n and ζ.

From the previously derived homogeneous, or free vibration, solution given in Eqn. A.14 and here denoted by denoted w_h, the total solution is then given by:

$$w = w_h + w_p = e^{-\zeta\omega_n t}\left(C_1 e^{j\omega_d t} + C_2 e^{-j\omega_d t}\right) + \frac{f_0}{\sqrt{(\omega_n^2 - \omega^2)^2 + (2\zeta\omega_n\omega)^2}} e^{j(\omega t - \phi)}\,. \tag{A.26}$$

As for the homogeneous case, this solution method yields a time domain solution to the

equation of motion where the coefficients C_1 and C_2 are determined based on the initial conditions. For large t the first term of the total solution, which corresponds to free vibration, decreases in relative importance in comparison to the forced term due to the exponential decay factor, $e^{-\zeta\omega_n t}$. For the steady state solution, this transitory contribution of the free vibration term is assumed to be zero, and the motion is determined by the forced solution.

A.3.2 Laplace Solution Method

Taking the Laplace Transform of the forced equation of motion, Eqn. A.1, yields:

$$m\left(s^2W - w_0 s - \dot{w}_0\right) + c\left(sW - w_0\right) + kW = F\left(s\right) . \tag{A.27}$$

Solving for W as before then yields the frequency domain system response:

$$\begin{aligned} W &= \frac{F\left(s\right) + m\left(w_0 s + \dot{w}_0\right) + cw_0}{ms^2 + cs + k} \\ &= \frac{\left(\frac{1}{m}\right)F\left(s\right) + w_0 s + \dot{w}_0 + 2\zeta\omega_n w_0}{s^2 + 2\zeta\omega_n s + \omega_n^2} . \end{aligned} \tag{A.28}$$

This frequency domain solution is dependent on the form of the forcing function F as well as the initial conditions w_0 and $\dot{w}_0$.

If we suppose zero initial conditions, the second row of Eqn. A.28 can be written:

$$\frac{W(s)}{F(s)} = \frac{1}{m} \cdot \frac{1}{s^2 + 2\zeta\omega_n s + \omega_n^2} , \tag{A.29}$$

which is known as the transfer function of the system, $H(s) \equiv \frac{W(s)}{F(s)}$. When $s = j\omega$, i.e. the system is in steady state oscillation, the transfer function is known as the frequency response function:

$$H(j\omega) = \frac{1}{m} \cdot \frac{1}{\omega_n^2 - \omega^2 + 2\zeta\omega_n\omega j} = \frac{1}{m}\left(\frac{\omega_n^2 - \omega^2 - 2\zeta\omega_n\omega j}{\left(\omega_n^2 - \omega^2\right)^2 + \left(2\zeta\omega_n\omega\right)^2}\right) . \tag{A.30}$$

The amplitude and phase of the frequency response function are given by:

$$\begin{aligned} |H(j\omega)| &= \frac{1}{m} \cdot \frac{1}{\sqrt{\left(\omega_n^2 - \omega^2\right)^2 + \left(2\zeta\omega_n\omega\right)^2}} \\ \underline{/H(j\omega)} &= -\tan^{-1}\left(\frac{2\zeta\omega_n\omega}{\omega_n^2 - \omega^2}\right), \end{aligned} \tag{A.31}$$

which correspond to the amplitude and phase of the complex-valued A given by Eqn. A.23 in the assumed solution method with $A = H \cdot F_0$.

A.4 Damping

In this thesis, the damping mechanism is assumed to be linear viscous damping, where the damping force is proportional to the velocity, $F_c = c\dot{w}$. Although somewhat restrictive, during steady state vibration other assumed forms can be approximated as an equivalent viscous damper that dissipates the same amount of energy [60].

An additional simplifying heuristic is that the damping constant, c, can be written as a linear combination of the mass and stiffness of the system:

$$c = \alpha m + \beta k\,. \tag{A.32}$$

This model, known as proportional damping, greatly simplifies the analysis of multiple degree of freedom systems by permitting the complete decoupling of the equations of motion into multiple SDOF systems. In Chapter 4, both the linear viscous and proportional damping assumptions are utilized in order to identify the parameters to be estimated.

When the damping ratio ζ is small, the damped and undamped natural frequencies are approximately the same. If the damping ratio is less than 10%, for example, the percent difference between the undamped and damped natural frequencies is less than 0.5%, as shown in Fig. A.2.

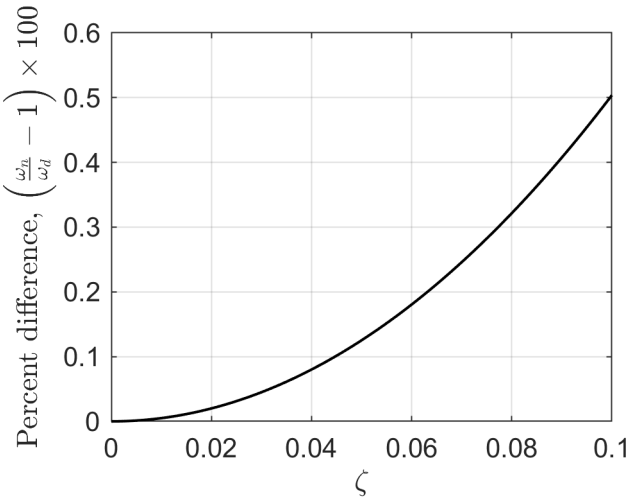

Figure A.2: Percent difference between undamped and damped natural frequencies as a function of damping ratio ζ.

In the beam and plate structures analyzed experimentally in this thesis, the damping ratio is small and the undamped natural frequency is close to the observed damped natural frequency.

Consider again the amplitude of the frequency response function given in Eqn. A.31. The normalized amplitude can be written in terms of the frequency ratio ($r = \omega/\omega_n$) as:

$$k \cdot |H(j\omega)| = \frac{1}{\sqrt{\left(1 - r^2\right)^2 + \left(2\zeta r\right)^2}} \,. \tag{A.33}$$

This response amplitude is plotted for various damping ratios around resonance in Fig. A.3.

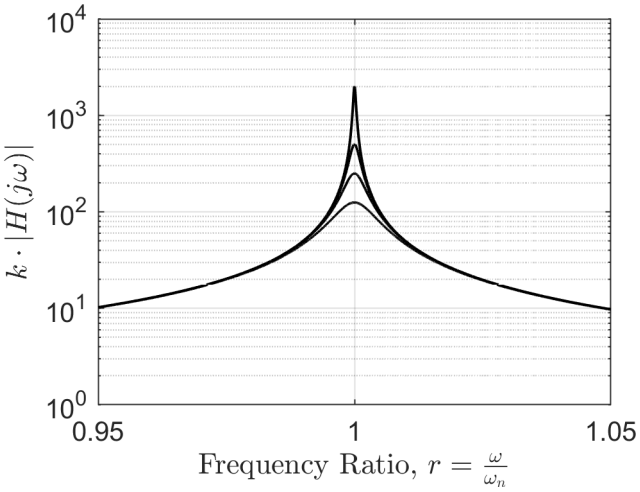

Figure A.3: Normalized displacement amplitude as a function of frequency ratio r for various damping ratios ($\zeta = 0.025, 0.1, 0.3, 0.4\%$).

For these lightly damped systems, increases in damping have a significant impact on the response amplitude near resonance. On the other hand, changes in the damping ratio do not have a significant impact on the frequency at which the maximum response occurs. In the cases shown in Fig. A.3, the response amplitude decreases by a factor of 16 between the lowest and highest damping values, while the frequency ratio corresponding to the maximum response only changes 0.002%. In addition, the response amplitude does not change significantly away from the region near resonance – the impact of damping changes is most pronounced near $r = 1$.

A.5 Parameter Sensitivity of Frequency Response

From Eqn. A.23, the force normalized steady-state amplitude of the harmonic acceleration response is:

$$\frac{\ddot{w}}{f_0} = \frac{\omega^2}{\sqrt{(\omega_n^2 - \omega^2) + (2\zeta\omega_n\omega)}}, \tag{A.34}$$

where f_0 is the mass normalized amplitude of the external forcing. Near resonance ($\omega \approx \omega_n$), this ratio is:

$$\frac{\ddot{w}_{\text{res}}}{f_0} \approx \frac{1}{2\zeta}\,. \tag{A.35}$$

For a lightly damped system, the maximum response (i.e. resonance) occurs nearly at the system's undamped natural frequency. The dependence of the maximum response amplitude on the system parameters can be approximated by conducting a parameter sensitivity analysis based on Eqn. A.35. The linearized change in response amplitude near resonance for variation of the parameters (only ζ in this case) is:

$$\Delta\left(\frac{\ddot{w}_{\text{res}}}{f_0}\right) = \frac{\partial}{\partial\zeta}\left(\frac{1}{2\zeta}\right)\Delta\zeta = -\frac{1}{2\zeta}\left(\frac{\Delta\zeta}{\zeta}\right)\,. \tag{A.36}$$

Rearranging, the normalized change is then given by:

$$\Delta\left(\frac{\ddot{w}_{\text{res}}}{f_0}\right) \Big/ \left(\frac{\ddot{w}_{\text{res}}}{f_0}\right) \approx -\frac{\Delta\zeta}{\zeta}\,. \tag{A.37}$$

In other words, a one percent increase in damping leads to approximately a one percent decrease in the force normalized acceleration response around resonance. For nonlinear systems, estimates of the damping ratio often vary widely for different response amplitudes, thus leading to significant changes in the system's maximum response at resonance.

If the external forcing is achieved through strain-induced (i.e. piezoelectric) actuation, then the amplitude of the external forcing is given by $f_0 = \gamma \cdot g v_0$, where g is the electromechanical factor to determine the equivalent force for a given voltage, and γ is the coupling correction factor. These parameters are described in Appendix C. Equation A.35 can then be written:

$$\frac{1}{\gamma}\cdot\frac{\ddot{w}_{\text{res}}}{g v_0} \approx \frac{1}{2\zeta}\,. \tag{A.38}$$

The linearized change in response amplitude for this case is then:

$$\Delta\left(\frac{\ddot{w}_{\text{res}}}{gv_0}\right) = \frac{\partial}{\partial\zeta}\left(\frac{\gamma}{2\zeta}\right)\Delta\zeta + \frac{\partial}{\partial\gamma}\left(\frac{\gamma}{2\zeta}\right)\Delta\gamma = -\frac{\gamma}{2\zeta}\left(\frac{\Delta\zeta}{\zeta}\right) + \frac{\gamma}{2\zeta}\left(\frac{\Delta\gamma}{\gamma}\right). \tag{A.39}$$

Rearranging as before, the normalized change is given by:

$$\Delta\left(\frac{\ddot{w}_{\text{res}}}{gv_0}\right) \Big/ \left(\frac{\ddot{w}_{\text{res}}}{gv_0}\right) \approx -\frac{\Delta\zeta}{\zeta} + \frac{\Delta\gamma}{\gamma}. \tag{A.40}$$

In other words, a one percent increase in the coupling correction γ will lead to a one percent increase in the force normalized acceleration response around resonance.

From this analysis it is seen that near resonance changes in ω_n do not lead to any changes in the force or voltage normalized acceleration responses, while changes in ζ and γ both impact the response. In experimental identification processes, then, misidentification of the damping ratio will lead to incorrect predictions for the maximum acceleration response for both electromagnetic and strain-induced actuation methods. The same is true for strain-induced actuation and misidentification of the coupling correction factor γ. As shown in Chapter 4, the changes in empirical damping ratio estimates for varying experimental procedures dominate the other parameter changes; thus, their misidentification has a particularly large impact on the accuracy of predicted responses.

APPENDIX B

VIBRATION OF MULTIPLE DEGREES OF FREEDOM SYSTEMS

B.1 Equation of Motion

Consider the multiple degrees of freedom (MDOF) system shown in Fig. B.1.

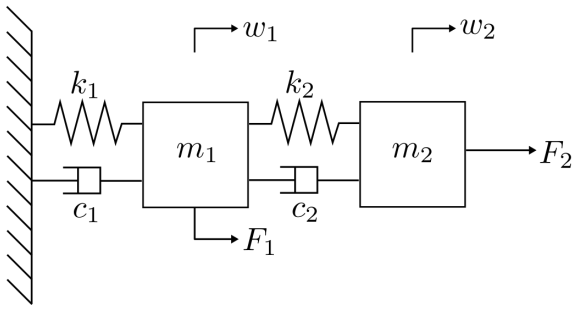

Figure B.1: Representative MDOF spring-mass-damper system.

Following the same procedure as for the single degree of freedom (SDOF) case, the equation of motion for this system will be derived in two manners: (1) Newton's Method and (2) Lagrange's Method. Both methods yield the same equation of motion, but it useful to illustrate both equilibrium and energy methods in the development of the system's equation of motion.

B.1.1 Newton's Method

Following the same analysis steps as previously shown for the SDOF system in Appendix A, the summation of forces and subsequent rearrangement leads to the equation of motion for

the MDOF system illustrated in Fig. B.1:

$$\sum \text{Forces} = \begin{Bmatrix} m_1\ddot{w}_1 \\ m_2\ddot{w}_2 \end{Bmatrix}$$

$$\begin{Bmatrix} -(k_1+k_2)\,w_1 + k_2 w_2 - (c_1+c_2)\,\dot{w}_1 + c_2\dot{w}_2 + F_1 \\ k_2 w_1 - k_2 w_2 + c_2\dot{w}_1 - c_2\dot{w}_2 + F_2 \end{Bmatrix} = \begin{Bmatrix} m_1\ddot{w}_1 \\ m_2\ddot{w}_2 \end{Bmatrix} \tag{B.1}$$

$$\begin{bmatrix} m_1 & 0 \\ 0 & m_1 \end{bmatrix} \begin{Bmatrix} \ddot{w}_1 \\ \ddot{w}_2 \end{Bmatrix} + \begin{bmatrix} c_1+c_2 & -c_2 \\ -c_2 & c_2 \end{bmatrix} \begin{Bmatrix} \dot{w}_1 \\ \dot{w}_2 \end{Bmatrix} + \begin{bmatrix} k_1+k_2 & -k_2 \\ -k_2 & k_2 \end{bmatrix} \begin{Bmatrix} w_1 \\ w_2 \end{Bmatrix} = \begin{Bmatrix} F_1 \\ F_2 \end{Bmatrix}$$

$$\boldsymbol{M}\ddot{\boldsymbol{w}} + \boldsymbol{C}\dot{\boldsymbol{w}} + \boldsymbol{K}\boldsymbol{w} = \boldsymbol{f}\,,$$

where $\boldsymbol{M}$, $\boldsymbol{C}$, and $\boldsymbol{K}$ are known as the system's mass, damping, and stiffness matrices and $\boldsymbol{f}$ is the vector of external forces. Since the off-diagonal terms of both the damping and stiffness matrices are non-zero, these equations of motion in the two degrees of freedom are coupled. Although progress can be made analyzing the system as given in Eqn. B.1, a more powerful analysis tool, known as modal analysis, will be described later in the section which leads to a set of uncoupled equations for the system. This form is desirable as the methods and results for the SDOF system are then directly applicable to each of the uncoupled equations.

Although the example MDOF system described here only has two degrees of freedom, the analysis would proceed in the same manner if additional degrees of freedom or different connecting stiffness and damping arrangements are present.

B.1.2 Lagrange's Method

For an MDOF system with n independent degrees of freedom, Lagrange's equations are written as [36]:

$$\frac{d}{dt}\left(\frac{\partial L}{\partial \dot{q}_i}\right) - \frac{\partial L}{\partial q_i} = Q_i \qquad (i = 1, 2, \ldots, n)\,, \tag{B.2}$$

where $q_1, q_2, \ldots, q_n$ are generalized coordinates and $Q_1, Q_2, \ldots, Q_n$ are generalized forces not derivable from a potential function. As for the SDOF case, the damping contributions are modeled as external forces. The Lagrangian, $L = T - V$, and generalized forces are given by:

$$\begin{aligned} L &= \frac{1}{2}m_1\dot{w}_1^2 + \frac{1}{2}m_2\dot{w}_2^2 - \frac{1}{2}k_1w_1^2 - \frac{1}{2}k_2\left(w_2 - w_1\right)^2 \\ Q_1 &= F_1 - c_1\dot{w}_1 + c_2\left(\dot{w}_2 - \dot{w}_1\right) \\ Q_2 &= F_2 - c_2\left(\dot{w}_2 - \dot{w}_1\right) . \end{aligned} \tag{B.3}$$

Substituting into Eqn. B.2 yields the two equations of motion:

$$\begin{gathered} \frac{d}{dt}\begin{Bmatrix} m_1\dot{w}_1 \\ m_2\dot{w}_2 \end{Bmatrix} + \begin{Bmatrix} k_1w_1 - k_2\left(w_2 - w_1\right) \\ k_2\left(w_2 - w_1\right) \end{Bmatrix} = \begin{Bmatrix} F_1 - c_1\dot{w}_1 + c_2\left(\dot{w}_2 - \dot{w}_1\right) \\ F_2 - c_2\left(\dot{w}_2 - \dot{w}_1\right) \end{Bmatrix} \\ \begin{bmatrix} m_1 & 0 \\ 0 & m_2 \end{bmatrix}\begin{Bmatrix} \ddot{w}_1 \\ \ddot{w}_2 \end{Bmatrix} + \begin{bmatrix} c_1 + c_2 & -c_2 \\ -c_1 & c_2 \end{bmatrix}\begin{Bmatrix} \dot{w}_1 \\ \dot{w}_2 \end{Bmatrix} + \begin{bmatrix} k_1 + k_2 & -k_2 \\ -k_2 & k_2 \end{bmatrix}\begin{Bmatrix} w_1 \\ w_2 \end{Bmatrix} = \begin{Bmatrix} F_1 \\ F_2 \end{Bmatrix} , \end{gathered} \tag{B.4}$$

which are the same as those determined using Newton's Method.

B.2 Undamped Free Vibration

Consider first the undamped, unforced, form of the equation of motion given by Eqn. B.1 (or equivalently Eqn. B.4), $\boldsymbol{M}\ddot{\boldsymbol{w}} + \boldsymbol{K}\boldsymbol{w} = \boldsymbol{0}$. The assumed solution method can be utilized here with an assumed form $\boldsymbol{w} = \boldsymbol{\phi}e^{j\omega t}$. This is analogous to the form assumed in the SDOF case, where here ϕ is a vector and the motion is assumed to be harmonic. Substituting into the MDOF equation of motion:

$$\begin{aligned} \left(\boldsymbol{K} - \omega^2\boldsymbol{M}\right)\boldsymbol{\phi}e^{j\omega t} &= 0 \\ \left(\boldsymbol{K} - \omega^2\boldsymbol{M}\right)\boldsymbol{\phi} &= 0 , \end{aligned} \tag{B.5}$$

where both sides have been divided by $e^{j\omega t}$. This is the form of an eigenproblem, where the eigenvalues (ω^2) and eigenvectors ($\boldsymbol{\phi}$) are to be determined. Since $\boldsymbol{\phi} = 0$ is the trivial solution, for a non-trivial solution the determinant of $\boldsymbol{K} - \omega^2\boldsymbol{M}$ must equal zero. For the example MDOF system:

$$\begin{aligned} \begin{vmatrix} k_1 + k_2 - \omega^2 m_1 & -k_2 \\ -k_2 & k_2 - \omega^2 m_2 \end{vmatrix} &= 0 \\ \left(k_1 + k_2 - \omega^2 m_1\right)\left(k_2 - \omega^2 m_2\right) - k_2^2 &= 0 \\ m_1 m_2 \omega^4 - \left(m_2\left(k_1 + k_2\right) + m_1 k_2\right)\omega^2 + k_1 k_2 &= 0\,. \end{aligned} \tag{B.6}$$

For given physical parameters, this equation can be solved for the eigenvalues, or natural frequencies ω_i, of the system. Substituting each eigenvalue into Eqn. B.5 will then lead to solutions for the corresponding eigenvectors $\boldsymbol{\phi}$, also known as the system's mode shapes.

B.3 Modal Coordinates

Rather than starting by assuming a solution to the equation of motion as in the previous section, first define a transformation $\boldsymbol{w} = \boldsymbol{M}^{-1/2}\boldsymbol{r}$. Assuming the mass matrix is diagonal (i.e. no mass coupling), the matrix square root is defined as the square root of each entry such that $\boldsymbol{M}^{1/2}\boldsymbol{M}^{1/2} = \boldsymbol{M}$. Substituting the defined transformation for $\boldsymbol{w}$ into the equation of motion and premultiplying by $\boldsymbol{M}^{-1/2}$ yields:

$$\ddot{\boldsymbol{r}} + \boldsymbol{M}^{-1/2}\boldsymbol{K}\boldsymbol{M}^{-1/2}\boldsymbol{r} = \boldsymbol{0}\,. \tag{B.7}$$

Now, assuming and substituting a solution of the form $\boldsymbol{r} = \boldsymbol{u}e^{j\omega t}$ for this transformed system yields the eigenproblem:

$$\left(\widetilde{\boldsymbol{K}} - \lambda\boldsymbol{I}\right)\boldsymbol{u} = \boldsymbol{0}\,, \tag{B.8}$$

where $\widetilde{\boldsymbol{K}} \equiv \boldsymbol{M}^{-1/2}\boldsymbol{K}\boldsymbol{M}^{-1/2}$ and $\lambda \equiv \omega^2$. If $\boldsymbol{M}$ and $\boldsymbol{K}$ are symmetric, then $\widetilde{\boldsymbol{K}}$ is also symmetric, and Eqn. B.8 is a symmetric eigenproblem. Determining the eigenvalues and eigenvectors for a symmetric eigenproblem is readily accomplished using any number of algorithms [60].

The eigenvectors $\boldsymbol{u}$ in this formulation, normalized such that they are orthonormal, can be arranged as columns in a matrix $\boldsymbol{U} = [\boldsymbol{u}_1,\ \boldsymbol{u}_2,\ \ldots]$. A second transformation can now be defined as $\boldsymbol{r} = \boldsymbol{U}\boldsymbol{\eta}$, which upon substitution into Eqn. B.7 and pre-multiplication by $\boldsymbol{U}^T$, yields:

$$\begin{aligned} \ddot{\boldsymbol{\eta}} + \boldsymbol{U}^T\boldsymbol{M}^{-1/2}\boldsymbol{K}\boldsymbol{M}^{-1/2}\boldsymbol{U}\boldsymbol{\eta} &= \boldsymbol{0} \\ \ddot{\boldsymbol{\eta}} + \boldsymbol{\Phi}^T\boldsymbol{K}\boldsymbol{\Phi}\boldsymbol{\eta} &= \boldsymbol{0} \\ \ddot{\boldsymbol{\eta}} + \boldsymbol{\Lambda}\boldsymbol{\eta} &= \boldsymbol{0}\,, \end{aligned} \tag{B.9}$$

where the modal matrix, $\boldsymbol{\Phi} \equiv \boldsymbol{M}^{-1/2}\boldsymbol{U}$, is the matrix of mass normalized eigenvectors, or mode shapes. Equation B.9 is the equation of motion expressed in modal coordinates, with modal mass matrix $\boldsymbol{\Phi}^T\boldsymbol{M}\boldsymbol{\Phi} = \boldsymbol{I}$, modal stiffness matrix $\boldsymbol{\Phi}^T\boldsymbol{K}\boldsymbol{\Phi} = \boldsymbol{\Lambda}$, and modal coordinates $\boldsymbol{\eta}$. Under the mass normalization used here, the modal stiffness matrix takes a special form: $\boldsymbol{\Lambda} = \mathrm{diag}\,(\omega_i^2)$.

In summary, the matrix $\boldsymbol{U}$ is the orthonormal matrix of eigenvectors and $\boldsymbol{\Lambda}$ is the diagonal matrix of eigenvalues of $\widetilde{\boldsymbol{K}} = \boldsymbol{M}^{-1/2}\boldsymbol{K}\boldsymbol{M}^{-1/2}$. The mass normalized eigenvectors are given by $\boldsymbol{\Phi} = \boldsymbol{M}^{-1/2}\boldsymbol{U}$, which describe the transformation between physical and modal coordinates, $\boldsymbol{w} = \boldsymbol{\Phi}\boldsymbol{\eta}$. Although this process appears somewhat convoluted, one of the main reasons this technique is particularly useful is that the equations of motion expressed in modal coordinates, given in Eqn. B.9, are uncoupled and can be solved individually as SDOF systems. These solutions can then be transformed back to the physical coordinates using the matrix of mass normalized eigenvectors.

B.4 Free Vibration in Modal Coordinates

In the previous section it was shown that the undamped free vibration equations of motion for an MDOF system can be uncoupled through the use of modal coordinates. Although this is not generally true for all forms of damping, the equations of motion can still be shown to be uncoupled for proportional damping [38]. Proportional damping, described previously for SDOF systems, defines the damping constant as a linear combination of the system mass and stiffness matrices. Proceeding directly by substituting the transformation $\boldsymbol{w} = \boldsymbol{\Phi\eta}$ into the forced equation of motion, Eqn. B.1, and premultiplying by $\boldsymbol{\Phi}^T$ yields:

$$\begin{aligned} \ddot{\boldsymbol{\eta}} + \boldsymbol{\Phi}^T\boldsymbol{C}\boldsymbol{\Phi}\dot{\boldsymbol{\eta}} + \boldsymbol{\Phi}^T\boldsymbol{K}\boldsymbol{\Phi}\boldsymbol{\eta} &= \boldsymbol{\Phi}^T\boldsymbol{f} \\ \ddot{\boldsymbol{\eta}} + \boldsymbol{C}_\eta\dot{\boldsymbol{\eta}} + \boldsymbol{\Lambda}\boldsymbol{\eta} &= \boldsymbol{f}_\eta\,, \end{aligned} \tag{B.10}$$

where $\boldsymbol{C}_\eta = \boldsymbol{\Phi}^T\boldsymbol{C}\boldsymbol{\Phi}$ is the modal damping matrix and $\boldsymbol{f}_\eta = \boldsymbol{\Phi}^T\boldsymbol{f}$ is the modal force vector. In the case of proportional damping, the modal damping matrix is diagonal, just as the modal mass and stiffness matrices, and the equations of motion for the N degrees of freedom are uncoupled:

$$\ddot{\eta}_i + 2\zeta_i\omega_i\dot{\eta}_i + \omega_i^2\eta_i = f_{\eta,i}\,, \tag{B.11}$$

for $i = 1, 2, \ldots, N$.

After applying the modal coordinate transformation, the analysis techniques described for the SDOF system can be used directly. In addition, reduced order models can be developed through modal truncation, where only a limited number of modes are considered. By ignoring the contributions of higher order modes which are far outside the frequency range of interest, this much simpler model can be used to approximate the total system response while reducing the complexity of analysis.

APPENDIX C
STRAIN-INDUCED TRANSVERSE VIBRATION OF A CANTILEVER BEAM

In strain-induced actuation of a piezocomposite beam, the external forcing term is due to an applied moment $M(\hat{x},t)$. By Eqn. 2.17, the equation of motion for transverse vibration can be written:

$$\rho A\frac{\partial^2 w\left(\hat{x},t\right)}{\partial t^2}+c\frac{\partial w\left(\hat{x},t\right)}{\partial t}+\frac{EI_y}{l^4}\frac{\partial^4 w\left(\hat{x},t\right)}{\partial \hat{x}^4}=\frac{\partial^2 M(\hat{x},t)}{\partial \hat{x}^2}\,. \tag{C.1}$$

The applied moment can be written as the product of three terms: (1) input voltage V to the piezocomposite device, (2) an electromechanical coupling term ϑ, and (3) a geometric term locating the piezocomposite device along the beam. The coupling term is given by [23]:

$$\vartheta=\frac{E_{\mathrm{MFC}}d_{31}b_p}{2h_p}\left(h_{pt}^2-h_{pb}^2\right)\,, \tag{C.2}$$

where the E_{MFC} is the elastic modulus of the total piezoelectric actuator, the subscript p is used to indicated quantities in reference to the active piezoelectric material, d_{31} is the coupling coefficient, and h_{pt} and h_{pb} are the distances in the z-direction from the composite neutral axis to the top and bottom of the active piezoelectric material. The geometric term for a piezoelectric actuator with start location $\hat{x}_{p1}$ and end location $\hat{x}_{p2}$ is written:

$$H\left(\hat{x}-\hat{x}_{p1}\right)-H\left(\hat{x}-\hat{x}_{p2}\right)\,, \tag{C.3}$$

where $H(\cdot)$ is the Heaviside function. Combining these equations yields the equation for the applied moment:

$$M(\hat{x},t)=-\vartheta V(t)\left[H\left(\hat{x}-\hat{x}_{p1}\right)-H\left(\hat{x}-\hat{x}_{p2}\right)\right]\,. \tag{C.4}$$

The quantities h_{pt} and h_{pb} in the coupling term can be determined by transforming the composite cross section into an equivalent cross section with uniform modulus [32]. Since the active piezoelectric element is sandwiched between insulating (Kapton) layers and comprises only a fraction of the total piezoelectric actuator, the distances to the top and bottom of the active material can be calculated only after determining the distances to the top and bottom of the total actuator, $h_{\mathrm{MFC},t}$ and $h_{\mathrm{MFC},b}$.

The untransformed composite cross-section is shown in Fig. C.1(a), where the subscript s refers to the substrate of the piezocomposite beam.

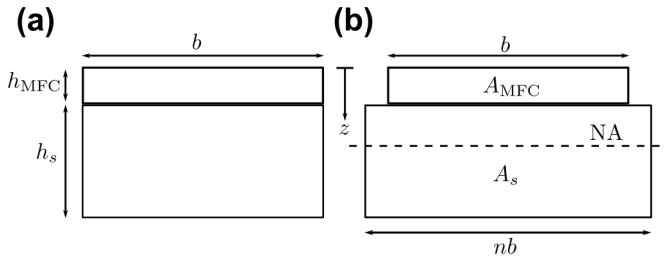

Figure C.1: (a) Composite beam cross-section. (b) Transformed beam cross-section with uniform modulus.

Defining $n = \frac{E_s}{E_{\mathrm{MFC}}}$, multiplying the width of the substrate by n transforms the cross-section into one with uniform modulus without changing the neutral axis. The transformed cross-section is shown in Fig. C.1(b). The distance of the neutral axis from the top of the piezoelectric actuator can be found by considering the contribution of each rectangular body in the transformed cross-section:

$$\begin{aligned} h_{\mathrm{MFC},t} &= \frac{A_{\mathrm{MFC}} z_{\mathrm{MFC}} + A_s z_s}{A_{\mathrm{MFC}} + A_s} = \frac{b h_{\mathrm{MFC}} \left(\frac{h_{\mathrm{MFC}}}{2}\right) + n b h_s \left(h_{\mathrm{MFC}} + \frac{h_s}{2}\right)}{b h_{\mathrm{MFC}} + n b h_s} \\ &= \frac{h_{\mathrm{MFC}}^2 + 2 n h_{\mathrm{MFC}} h_s + n h_s^2}{2\left(h_{\mathrm{MFC}} + n h_s\right)}, \end{aligned} \tag{C.5}$$

where $z_{\text{MFC}} = \frac{h_{\text{MFC}}}{2}$ and $z_s = h_{\text{MFC}} + \frac{h_s}{2}$ are the distances from the top of the piezoelectric actuator its center and to the substrate. The distance from the neutral axis to the bottom of the piezoelectric actuator can then be determined:

$$h_{\text{MFC},b} = h_{\text{MFC},t} - h_{\text{MFC}}\,. \tag{C.6}$$

Finally, the distances from the neutral axis to the active piezoelectric element are:

$$\begin{aligned} h_{pt} &= h_{\text{MFC},t} - \left(\frac{h_{\text{MFC}} - h_p}{2}\right) \\ h_{pb} &= h_{\text{MFC},b} + \left(\frac{h_{\text{MFC}} - h_p}{2}\right)\,. \end{aligned} \tag{C.7}$$

Now substituting Eqn. C.4, the external moment equation, into the equation of motion [34]:

$$\rho A \frac{\partial^2 w\left(\hat{x},t\right)}{\partial t^2} + c\frac{\partial w\left(\hat{x},t\right)}{\partial t} + \frac{EI_y}{L^4}\frac{\partial^4 w\left(\hat{x},t\right)}{\partial \hat{x}^4} = -\vartheta v(t)\left[\frac{d\delta\left(\hat{x}-\hat{x}_{p1}\right)}{d\hat{x}} - \frac{d\delta\left(\hat{x}-\hat{x}_{p2}\right)}{d\hat{x}}\right]\,, \tag{C.8}$$

where $\delta(\cdot)$ is the Dirac delta. Substituting the modal solution $w(\hat{x},t) = \sum_{r=1}^{\infty}\eta_r(t)\phi_r(\hat{x})$ results in the equation of motion for the r-th modal coordinate:

$$\ddot{\eta}_r + 2\zeta_r\omega_r\dot{\eta}_r + \omega_r^2\eta_r = \frac{1}{\rho A}F_r(t)\,, \tag{C.9}$$

where ζ_r is the modal damping ratio and the modal forcing term is:

$$\begin{aligned} F_r(t) &= -\vartheta V(t)\int_0^1 \left[\frac{d\delta\left(x-x_{p1}\right)}{dx} - \frac{d\delta\left(x-x_{p2}\right)}{dx}\right]\phi_r(\hat{x})\;d\hat{x} \\ &= -\vartheta\left[\phi_r'(\hat{x}_{p2}) - \phi_r'(\hat{x}_{p1})\right]V(t)\,. \end{aligned} \tag{C.10}$$

For convenience, the factor multiplying the voltage in the modal forcing term is defined:

$$g \equiv -\vartheta\left[\phi_r'(\hat{x}_{p2}) - \phi_r'(\hat{x}_{p1})\right]\,, \tag{C.11}$$

so the modal equation of motion can be written as:

$$\ddot{\eta}_r + 2\zeta_r \omega_r \dot{\eta}_r + \omega_r^2 \eta_r = \frac{g}{\rho A} V(t)\,. \tag{C.12}$$

For empirical model estimation, a coupling correction factor $\gamma = \frac{\hat{g}}{g}$ is estimated which multiplies the analytical coefficient g to yield the estimated input force. Based on this equation of motion, it is noted that holding the input voltage constant is theoretically equivalent to holding the input force constant.

The equation for the coupling correction can be rearranged as:

$$\hat{g} = \gamma g = \gamma \left(-\frac{E_p d_{31} b_p}{2h_p} \left(h_{pt}^2 - h_{pb}^2 \right) \left[\phi_r'(\hat{x}_{p2}) - \phi_r'(\hat{x}_{p1}) \right] \right) = C \cdot \gamma d_{31}\,, \tag{C.13}$$

where C is a constant based on the material and geometric properties of the piezocomposite beam. From this expression, γ can be interpreted as a correction factor to the coupling coefficient d_{31} of the piezocomposite actuator.

APPENDIX D
ANALYTICAL DERIVATION OF THE EFFECTIVE STIFFNESS OF A CANTILEVER BEAM WITH A SHAKER

Consider a cantilever beam with additional linear spring (i.e. electromagnetic shaker), with spring force R, located between the root and tip as shown in Fig. D.1.

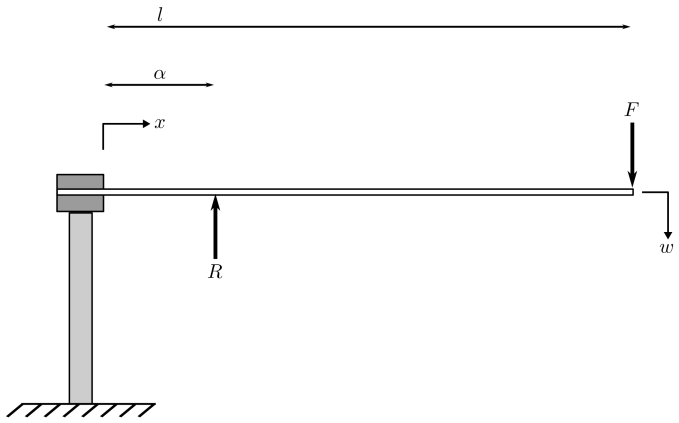

Figure D.1: Tip loaded cantilever beam with additional linear spring located at α.

A single point load is applied at position l and the point $\alpha \in [0, l]$ denotes the position of the linear spring. The spring force, $R = k \cdot w(\alpha)$, is to be determined, where k is the linear spring stiffness.

The total complementary energy of the system is given by [35]:

$$\pi^* = U^* + V^* \,, \tag{D.1}$$

where the strain and load potential energies are:

$$\begin{aligned} U^* + &= \frac{1}{2}\int_0^l \frac{M^2}{EI}\, dx + \frac{1}{2}k \cdot w(\alpha)^2 = \frac{1}{2}\int_0^l \frac{M^2}{EI}\, dx + \frac{R^2}{2k} \\ V^* &= -\iiint_V u_i B_i\, dV - \iint_{S_2} u_i T_i^{(\nu)}\, dS = 0\,. \end{aligned} \tag{D.2}$$

From a static analysis of the beam, the moment in the section of the beam located at x in terms of the spring force R is:

$$M(x) = \begin{cases} F(l-x) - R(\alpha - x), & 0 \le x \le \alpha \\ F(l-x), & \alpha \le x \le l \end{cases}\,. \tag{D.3}$$

Substituting this moment relationship into Eqn. D.1, the total complementary energy is:

$$\pi^* = \frac{1}{2EI}\left[\int_0^\alpha \left\{F(l-x) - R(\alpha - x)\right\}^2\, dx + \int_\alpha^l \left\{F(l-x)\right\}^2\, dx\right] + \frac{R^2}{2k}\,, \tag{D.4}$$

where the integral domain has been split into two convenient parts. Extremizing π^* requires that $\frac{\partial \pi^*}{\partial R} = 0$, so:

$$\frac{\partial \pi^*}{\partial R} = -\frac{1}{EI}\left[\int_0^a \left\{F(l-x) - R(\alpha - x)\right\}(\alpha - x)\, dx\right] + \frac{R}{k} = 0\,. \tag{D.5}$$

This equation can now be solved for the spring force, R:

$$R = \left(\frac{k\alpha^2}{3EI + k\alpha^3}\right)\left(\frac{3l - \alpha}{2}\right)F\,. \tag{D.6}$$

Now by Eqn. D.3, the moment in the beam is:

$$M(x) = \begin{cases} F\left[l - x - \left(\frac{k\alpha^2}{3EI+k\alpha^3}\right)\left(\frac{3l-\alpha}{2}\right)(\alpha - x)\right], & 0 \le x \le \alpha \\ F(l-x), & \alpha \le x \le l \end{cases}\,. \tag{D.7}$$

The moment equation can be integrated twice over each domain to determine the deflec-

tion profile of the beam in each of those two sections from the relationship $EI \cdot w(x) = \iint M(x)\, dxdx$. Using the root boundary conditions, $w(0) = w'(0) = 0$, and the continuity conditions between the two domains, $w(\alpha)^- = w(\alpha)^+$ and $w'(\alpha)^- = w'(\alpha)^+$, the deflection of the beam is given by:

$$w(x) = \begin{cases} \frac{Fx^2}{6EI}\left[3l - x - \left(\frac{k\alpha^2}{3EI+k\alpha^3}\right)\left(\frac{3l-\alpha}{2}\right)(3\alpha - x)\right], & 0 \le x \le \alpha \\ \frac{F}{6EI}\left[3lx^2 - x^3 - \left(\frac{k\alpha^4}{3EI+k\alpha^3}\right)\left(\frac{3l-\alpha}{2}\right)(3x - \alpha)\right], & \alpha \le x \le l \end{cases} . \tag{D.8}$$

At the beam tip, the deflection is thus:

$$w(l) = \frac{FL^3}{3EI}\left[1 - \frac{\alpha^4}{4l^3}\left(\frac{k(3l-\alpha)^2}{3EI + k\alpha^3}\right)\right] = \frac{Fl^3}{3EI}\left[1 - \frac{\tilde{\alpha}^4}{4}\left(\frac{k(3-\tilde{\alpha})^2}{\frac{3EI}{l^3} + k\tilde{\alpha}^3}\right)\right] . \tag{D.9}$$

where $\tilde{\alpha} \equiv \alpha/l$ is the normalized location of the linear spring.

Instead of the spring acting through position α, an equivalent system can be developed which yields the same tip deflection with a different spring of stiffness k^* acting at l. The tip deflection for this equivalent system can be determined by evaluating Eqn. D.9 for $\tilde{\alpha} = 1$:

$$w^*(l) = \frac{Fl^3}{3EI}\left[1 - \frac{k^*}{\frac{3EI}{l^3} + k^*}\right] . \tag{D.10}$$

Now since the tip deflections are assumed equal, equating Eqn. D.9 (which represents the system with spring located at arbitrary $\tilde{\alpha}$) with Eqn. D.10 (which represents the system with spring located at $\tilde{\alpha} = 1$) and solving for the equivalent tip stiffness k^* yields the following Lemma:

$$k^* = \frac{3EI}{l^3}\left(\frac{k\tilde{\alpha}^4(3-\tilde{\alpha})^2}{4\left(\frac{3EI}{l^3}\right) + k\tilde{\alpha}^3(1-\tilde{\alpha})^2(4-\tilde{\alpha})}\right) . \tag{D.11}$$

In the limit $\tilde{\alpha} \to 0$, the spring location is approaching the beam root and $k^* \to 0$. Alternatively, in the limit $\tilde{\alpha} \to 1$, the spring location is approaching the beam tip and $k^* \to k$.

APPENDIX E
FINITE ELEMENT METHOD

Although MSC NASTRAN 2018.0 [49] is used to analyze the finite element (FE) models in this thesis, in this appendix a brief description of the FE method applied to a cantilever beam is given. The material discussed here builds on previous results discussed in this thesis and follows the general development given by Chandrupatla and Belegundu [61], where derivations of the results stated here can be found.

Consider a beam element as shown in Fig. E.1.

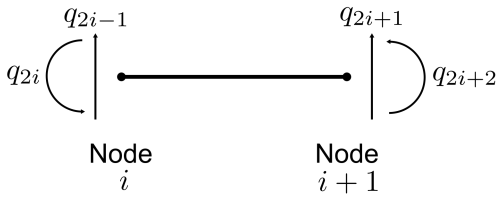

Figure E.1: Finite element degrees of freedom for beam element.

The i-th node ($i \in [1,\ 2, \ldots,\ N]$) has two degrees of freedom: q_{2i-1} for transverse displacement and q_{2i} for rotation. The element stiffness matrix is given by:

$$\boldsymbol{k}^e = \frac{EI_y}{l_e^3} \left[\begin{array}{cc:cc} 12 & 6l_e & -12 & 6l_e \\ 6l_e & 4l_e^2 & -6l_e & 2l_e^2 \\ \hdashline -12 & -6l_e & 12 & -6l_e \\ 6l_e & 2l_e^2 & -6l_e & 4l_e^2 \end{array}\right] \equiv \left[\begin{array}{c:c} K_{11} & K_{12} \\ \hdashline K_{21} & K_{22} \end{array}\right], \tag{E.1}$$

and the element mass matrix is:

$$\boldsymbol{m}^e = \frac{\rho A l_e}{420}\left[\begin{array}{cc:cc} 156 & 22l_e & 54 & -13l_e \\ 22l_e & 4l_e^2 & 13l_e & -3l_e^2 \\ \hdashline 54 & 13l_e & 156 & -22l_e \\ -13l_e & -3l_e^2 & -22l_e & 4l_e^2 \end{array}\right] \equiv \left[\begin{array}{c:c} M_{11} & M_{12} \\ \hdashline M_{21} & M_{22} \end{array}\right], \tag{E.2}$$

where l_e is the length of the element, A is its cross-sectional area, E is the elastic modulus, and I_y is the area moment of inertia for bending about the y-axis. The use of the submatrices K_{ij} and M_{ij} will be shown next. The global stiffness and mass matrices can be constructed for a beam of arbitrary number of elements through the process of assembly, where the combined stiffness and mass contributions from elements whose nodes are colocated are determined. For a simple beam, the global stiffness and mass matrices are:

$$\begin{aligned} \boldsymbol{K}_{\text{global}} &= \begin{bmatrix} K_{11} & K_{12} & 0 & 0 & \cdots & 0 \\ K_{21} & K_{11}+K_{22} & K_{12} & 0 & & 0 \\ 0 & K_{21} & K_{11}+K_{22} & K_{12} & & 0 \\ 0 & 0 & K_{21} & K_{11}+K_{22} & & 0 \\ \vdots & & & & \ddots & \vdots \\ 0 & 0 & 0 & 0 & \cdots & K_{22} \end{bmatrix} \\ \boldsymbol{M}_{\text{global}} &= \begin{bmatrix} M_{11} & M_{12} & 0 & 0 & \cdots & 0 \\ M_{21} & M_{11}+M_{22} & M_{12} & 0 & & 0 \\ 0 & M_{21} & M_{11}+M_{22} & M_{12} & & 0 \\ 0 & 0 & M_{21} & M_{11}+M_{22} & & 0 \\ \vdots & & & & \ddots & \vdots \\ 0 & 0 & 0 & 0 & \cdots & M_{22} \end{bmatrix}. \end{aligned} \tag{E.3}$$

For a cantilever beam, the first two degrees of freedom are constrained (i.e. the displacement and slope at the root are zero). The reduced stiffness and mass matrices ($\boldsymbol{K}$

and $\boldsymbol{M}$) which account for these boundary conditions are formed from the global matrices defined above by eliminating the first two rows and columns from each matrix. The unforced multiple degree of freedom equation of motion is then written:

$$\boldsymbol{M}\ddot{\boldsymbol{q}} + \boldsymbol{K}\boldsymbol{q} = 0\,. \tag{E.4}$$

As in Appendix B, the solution to this equation of motion can be determined by substituting the assumed form $\boldsymbol{q} = \boldsymbol{\phi}e^{j\omega t}$, which yields the eigenproblem:

$$\left(\boldsymbol{K} - \omega^2\boldsymbol{M}\right)\boldsymbol{\phi} = 0\,, \tag{E.5}$$

where ω^2 are the eigenvalues and $\boldsymbol{\phi}$ are the eigenvectors. Based on the previous development in Appendix B, the natural frequencies of the system are given by ω_i and the mode shapes by $\boldsymbol{\phi}$.

This method can be carried out in MATLAB [55] by forming the associated reduced stiffness and mass matrices for the beam with properties described in Table 3.1 and a user-specified number of beam elements. The deflections between nodes are determined based on Hermite shape functions which satisfy the calculated deflections and slopes at the nodes exactly. For a given element i, the shape function is defined as:

$$v = \frac{1}{4}\begin{bmatrix} 2 - 3\xi + \xi^3 \\ 1 - \xi - \xi^2 + \xi^3 \\ 2 + 3\xi - \xi^3 \\ -1 - \xi + \xi^2 + \xi^3 \end{bmatrix}^T \begin{bmatrix} q_{2i-1} \\ q_{2i} \\ q_{2i+1} \\ q_{2i+2} \end{bmatrix} = \boldsymbol{H}\boldsymbol{q}_i\,, \tag{E.6}$$

where $\xi \in [-1,\ 1]$ describes the domain between the nodes of the element ($\xi = -1$ corresponding to the first node and $\xi = 1$ to the second node) and $\boldsymbol{q}_i$ represents the degrees of freedom associated with element i.

The resulting mode shapes (eigenvectors) for several increasing numbers of elements are shown in Fig. E.2.

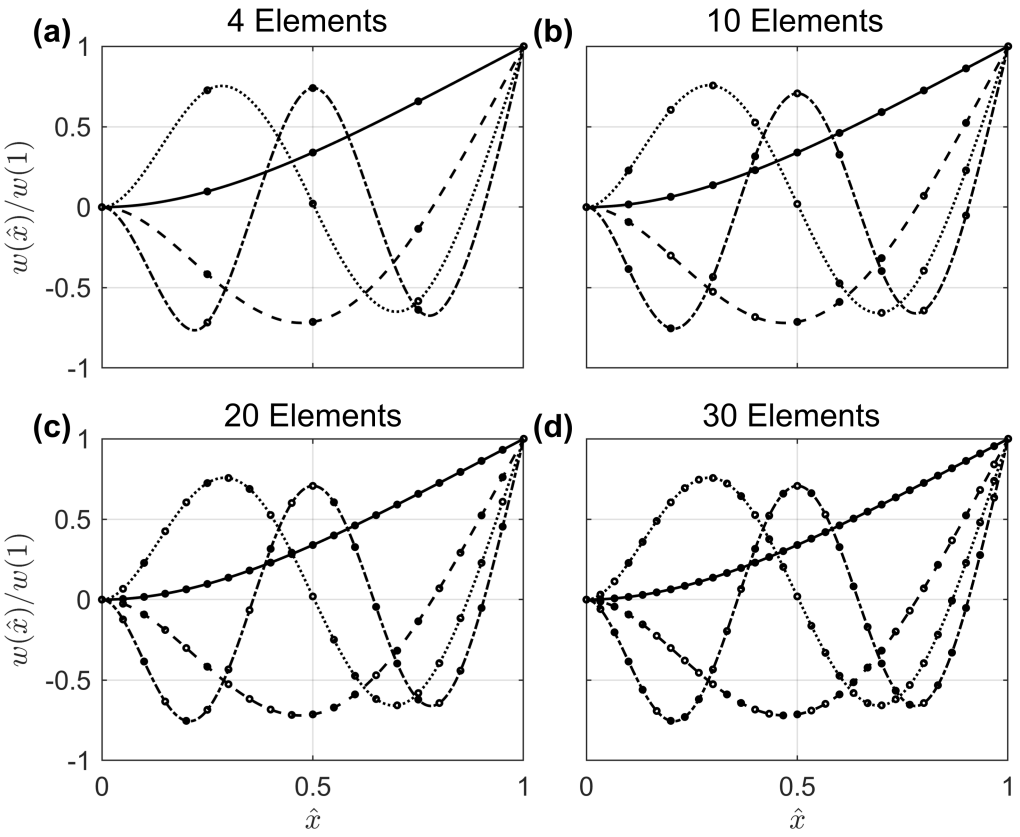

Figure E.2: First four FE bending mode shapes of a cantilever beam for increasing number of elements. Dots indicate nodal displacements and lines indicate the shape functions between nodes.

Comparing these mode shapes with the analytical solutions of the beam partial differential equation (Fig. 2.8) shows that even with only four elements the FE results are in close agreement. As the number of elements increase, the accuracy of the numerical FE mode shapes converges quickly towards the analytical solution. The convergence of the natural frequency estimates for increasing number of elements is also fast, as shown in Fig. E.3.

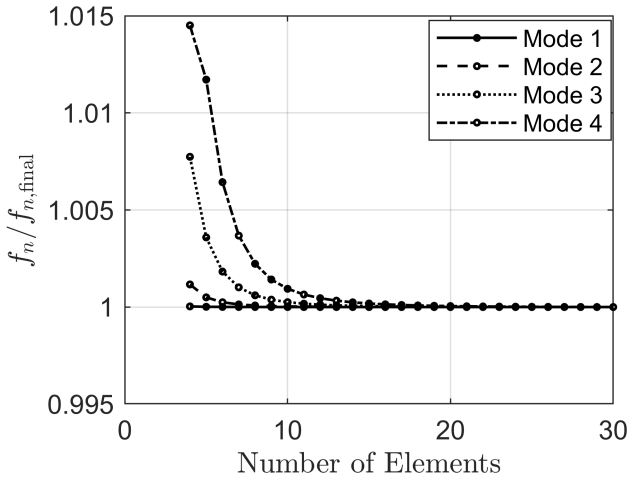

Figure E.3: Convergence of FE analysis natural frequencies for the first four bending modes of a cantilever beam as the number of elements is increased.

With 30 elements, the natural frequencies based on the finite element method are $f_n = [13.0,\ 81.7,\ 228.8,\ 448.4]$, which are the same as those based on the analytical solution to the distributed parameter equation of motion and those resulting from the use of NASTRAN as reported in Table 3.4.

APPENDIX F

SYSTEM IDENTIFICATION CASE STUDY: SUMMARY OF EMPIRICAL AND MODEL ESTIMATES

The empirical estimates for the various dynamic testing procedures implemented in Chapter 4, as summarized in Table 4.3, are reported here in comparison to those estimates based on the constant and variable parameter models.

Table F.1: Comparison of parameter estimates. Constant parameter (CP) and variable parameter (VP) model estimates correspond to methods outlined in Chapter 4.

Test Method	$\frac{1}{2\pi} \cdot \hat{\omega}_n$ (Hz)				$\hat{\zeta}$ (%)			$\hat{\gamma}$	
	Peak	Quadrature	CP	VP	1/2-Power	CP	VP	CP	VP
Electromagnetic,	11.88	11.87	11.88	11.89	0.3177	0.2455	0.2351	-	-
Open Loop	11.89	11.89	11.89	11.90	0.2950	0.2394	0.2205		
	11.91	11.91	11.91	11.92	0.2858	0.2302	0.2018		
	11.95	11.95	11.94	11.94	0.2153	0.1802	0.1663		
	12.00	12.00	12.00	12.00	0.1687	0.1192	0.0957		
Electromagnetic,	11.87	11.86	11.87	11.87	0.3751	0.2589	0.2599	-	-
Closed Loop	11.88	11.87	11.88	11.89	0.3477	0.2285	0.2395		
Acceleration	11.90	11.89	11.90	11.92	0.3231	0.2096	0.2144		
	11.93	11.94	11.93	11.94	0.2723	0.1656	0.1710		
	12.03	12.02	12.02	12.04	0.0873	0.0465	0.0365		
Electromagnetic,	11.88	11.87	11.88	11.88	0.3620	0.2442	0.2500	-	-
Closed Loop	11.89	11.88	11.89	11.89	0.3453	0.2302	0.2324		
Velocity	11.91	11.90	11.91	11.91	0.3257	0.2158	0.2093		
	11.95	11.96	11.95	11.95	0.2236	0.1331	0.1616		
	12.03	12.03	12.03	12.02	0.1229	0.0570	0.0610		
Electromagnetic,	11.86	11.86	11.88	11.87	0.4257	0.2664	0.2668	-	-
Closed Loop	11.87	11.86	11.88	11.88	0.3835	0.2465	0.2536		
Force	11.88	11.87	11.90	11.89	0.3513	0.2326	0.2356		
	11.90	11.90	11.92	11.91	0.3247	0.2121	0.2099		
	11.94	11.95	11.96	11.95	0.2473	0.1431	0.1631		
Strain-induced,	12.09	12.09	12.10	12.10	0.4470	0.4410	0.4309	0.3345	0.3322
Open Loop	12.09	12.09	12.11	12.11	0.4279	0.4242	0.4160	0.3291	0.3262
	12.10	12.11	12.12	12.12	0.4138	0.4068	0.3972	0.3229	0.3180
	12.12	12.12	12.14	12.13	0.3828	0.3704	0.3704	0.3108	0.3069
	12.15	12.15	12.17	12.15	0.3245	0.3369	0.3273	0.2951	0.2896
Strain-induced,	12.14	12.14	12.14	12.15	0.3065	0.3223	0.3364	0.3027	0.3098
Closed Loop	12.15	12.15	12.15	12.16	0.3170	0.3195	0.3195	0.2989	0.3037
Acceleration	12.17	12.17	12.16	12.17	0.3061	0.3113	0.2949	0.2925	0.2936
	12.20	12.16	12.20	12.20	0.2170	0.2269	0.2382	0.2785	0.2742
	12.21	12.21	12.21	12.25	0.1907	0.2067	0.1375	0.2573	0.2641
Strain-induced,	12.14	12.14	12.14	12.15	0.3151	0.3229	0.3425	0.3027	0.3085
Closed Loop	12.15	12.15	12.15	12.15	0.3096	0.3140	0.3267	0.2984	0.3025
Velocity	12.16	12.16	12.16	12.16	0.3144	0.3171	0.3094	0.2941	0.2957
	12.18	12.18	12.18	12.18	0.2936	0.3023	0.2810	0.2861	0.2832
	12.21	12.21	12.21	12.21	0.2082	0.2205	0.2150	0.2690	0.2646

VITA

Patrick Sean Heaney
Old Dominion University
Department of Mechanical and Aerospace Engineering
238 Kaufman Hall, Norfolk, Virginia 23529

Education:

University of Pennsylvania — Philadelphia, Pennsylvania
Master of Science in Education — May 2014
Thesis: High-Stakes Testing Accountability in Charter Schools: A Case Study of Stakeholder Perceptions

Yale University — New Haven, Connecticut
Bachelor of Arts in Economics and Mathematics — May 2009

Professional Experience:

NASA Langley Research Center, Aeroelasticity Branch — Hampton, Virginia
Pathways Intern — Oct. 2017 - Present
NASA Education AS&ASTAR Fellow — Sep. 2016 - Oct. 2017

Awards:

- NASA Education Aeronautics Scholarships and Advanced STEM Training and Research Fellowship, Sept. 2016 - Oct. 2017
- Best Presentation, Modeling, Simulation, & Visualization Student Capstone Conference, Education & Training, Apr. 2016
- Second Place, American Society of Naval Engineers (ASNE) Day 2016 Graduate Student Poster Competition, Mar. 2016

Selected Publications:

1. P. S. Heaney, T. G. Ivanco, and O. Bilgen, "Distributed sensing of a cantilever beam and plate using a fiber optic sensing system," in *Proceedings of 2018 AIAA Aviation and Aeronautics Forum and Exposition (AIAA Aviation)*, Atlanta, GA, 2018
2. P. S. Heaney and G. Hou, "Projection method with minimal correction procedure for numerical simulation of constrained dynamics," in *ASME 2017 Dynamic Systems and Control Conference*, Tysons Corner, VA, 2017
3. P. S. Heaney and O. Bilgen, "Nonlinearities in experimental system identification of a piezocomposite beam model," in *Proceedings of ASME 2017 Conference on Smart Materials, Adaptive Structures and Intelligent Systems*, vol. 2, Snowbird, UT, USA, 2017
4. P. S. Heaney and O. Bilgen, "Experimental mode shape identification for a cantilever beam using optical fiber bragg gratings," in *Proceedings of ASME 2017 Conference on Smart Materials, Adaptive Structures and Intelligent Systems*, vol. 2, Snowbird, UT, USA, 2017